THESIS

OBSERVATIONS AND SIMULATIONS OF SYNOPTIC, REGIONAL, AND LOCAL VARIATIONS OF ATMOSPHERIC CO$_2$

Submitted by
Jih-Wang Wang
Department of Atmospheric Science

ABSTRACT OF THESIS

OBSERVATIONS AND SIMULATIONS OF SYNOPTIC, REGIONAL, AND LOCAL VARIATIONS OF ATMOSPHERIC CO$_2$

With the increasing temporal and spatial density of CO$_2$ flux and concentration observations from worldwide tower networks, the importance of interpreting the data is becoming more conspicuous. Previous work shows that tower observations might be able to catch synoptic, regional, and local signals of CO$_2$ simultaneously. Thus a study that can explain CO$_2$ transport and the response of the ecosystem to the weather change simultaneously is necessary and will help the development of the regional inverse modeling technique in the future.

We have chosen a frontal case at the WLEF tower site in Wisconsin, USA, on 2001/08/16 from a case pool of 51 cold fronts during the summers of year 1997 to 2001. This frontal event on 2001/08/16 had an increasing CO$_2$ trend before the front arrived at the WLEF site and a decreasing trend after that. The discrepancy between the CO$_2$ concentrations estimated from the vertical flux divergence of the WLEF tower flux data and the observed CO$_2$ concentrations indicates that both the local ecosystem response to the weather change and horizontal advection determine the atmospheric CO$_2$ concentration. The data analysis also shows that on 2001/08/15, stronger respiration at

night due to warmer air temperature and slow photosynthesis during the day due to the cloud cover might be responsible for a small part of the slow CO_2 accumulation in the lower levels in northern Wisconsin. Horizontal advection is, however, the most important mechanism to bring CO_2-rich air and increase it by more than 40 ppm.

SiB 2.5 (Sellers *et al.*, 1996) and RAMS 5.04 (Pielke *et al.* 1992, Cotton *et a1.* 2002) with a newly implemented Grell (1995) convection scheme are coupled together. We have implemented the interface of the exchange of latent heat, sensible heat, radiation, CO_2, water vapor, and momentum between the land surface and the atmosphere, and employed the latest high-resolution soil map, satellite vegetation map, and biome map. The model is designed to simulate the regional CO_2 budget, its transport, and the feedback between the ecosystem and the local weather.

Our case simulation shows that a high CO_2 concentration air mass is built up in Oklahoma and Texas on 2001/08/14 and 2001/08/15 due to very strong daytime respiration and the shut-down of photosynthesis caused by hot and dry air over that region. The leading edge of this air mass then reaches out to the north at lower levels and is responsible for the increasing trend of CO_2 concentration at the WLEF site on 2001/08/15. On 2001/08/16, a low CO_2 concentration air mass from Canada is advected into northern Wisconsin and gradually sweeps the CO_2-rich air to the southeast. The simulation results cannot, however, explain all the $[CO_2]$ temporal variation that is detected by the WLEF tower during this frontal event. Further refinement of the coupled model is needed to simulate the rather weak photosynthesis rate on a cloudy day, such as

during the daytime of 2001/08/15, and to correctly reproduce the synoptic signals that

travel across North America.

This case study confirms the existence of mixing signals from at least two different scales:

horizontal advection and the local ecosystem response to the weather change. Without an

appropriate tool to successfully simulate CO_2 concentration spatial distributions, regional

wind fields, and the correct timing and strength of the local ecosystem signal to solve the

signal puzzle from different scales, it is improper to exploit tower observation data in

inverse modeling to determine regional sources and sinks.

Jih-Wang Wang
Department of Atmospheric Science
Colorado State University
Fort Collins, CO 80523
Summer 2005

Chapter I   Introduction

1.1 CO$_2$ Increase in the Atmosphere

Fossil fuel burning, deforestation, cement manufacture, and land use change have

resulted in more than 30% increase in atmospheric concentration of carbon dioxide (CO$_2$)

since late 19th century. CO$_2$ concentration, or [CO$_2$], in the atmosphere has risen from

280 ppmv (parts per million by volume of dry air) before the industrial revolution, to 375

ppmv in 2003, shown by Figure 1.1 from the National Oceanic and Atmospheric

Administration Climate Monitoring and Diagnostics Laboratory (NOAA/CMDL).
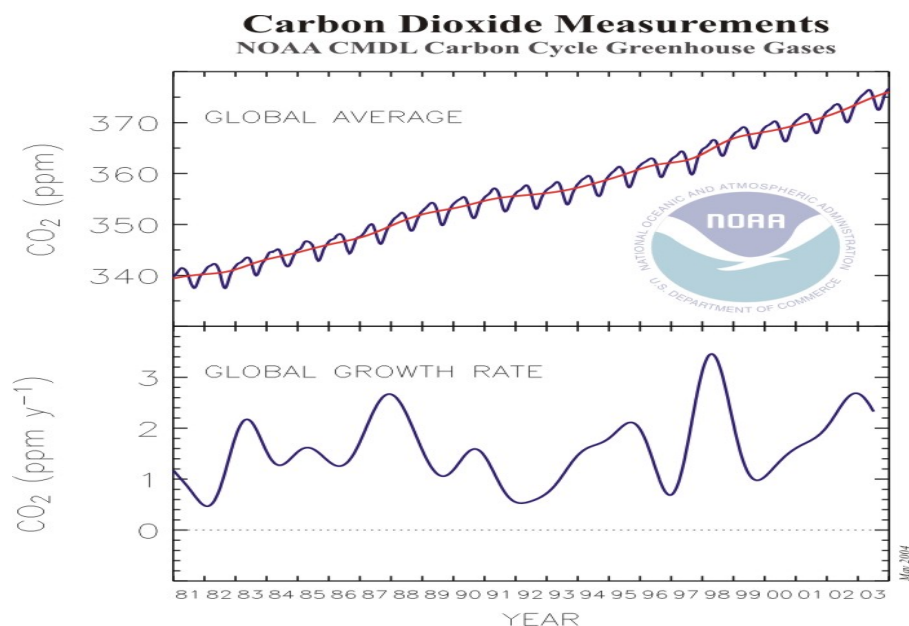
Top: Global average atmospheric carbon dioxide mixing ratios (blue line) determined using measurements from the NOAA CMDL cooperative air sampling network. The red line represents the long-term trend. Bottom: Global average growth rate for carbon dioxide. Principal investigator: Dr. Pieter Tans, NOAA CMDL Carbon Cycle Greenhouse Gases, Boulder, Colorado, (303) 497-6278 (pieter.tans@noaa.gov, http://www.cmdl.noaa.gov/ccgg).

Figure 1.1: Global average CO_2 concentration and growth rate. From NOAA/CMDL website, http://www.cmdl.noaa.gov/gallery/ccgg_figures.

As a greenhouse gas, CO_2 absorbs longwave radiation emitted from the surface and re-emits it back, resulting in more surface warming than would exist otherwise; this is called the "greenhouse effect". Thus increasing CO_2 concentration in the atmosphere is related to the Earth's radiative imbalance. Approximately 6.3 Gigatons (Gt) of carbon is introduced into the atmosphere every year due to fossil fuel burning and cement manufacture (Andres *et al.* 1996). Tropical deforestation has contributed another ~1.6 Gt C yr^{-1} during the 1980s (Schimel 1995). However, the rate of CO_2 increase in the atmosphere is estimated to be only about half the amount that is being emitted each year by the primary source of fossil fuel burning (Andres *et al.* 1996). Since atmospheric CO_2 is a passive gas (not chemically reactive) in the air, the rest might be taken up by the terrestrial biosphere and/or dissolved into water bodies instead of being consumed by chemical reactions in the atmosphere. The part that cannot be accounted for is called "missing sink", because where, how, and when the sink works is still not clear. The remains in the atmosphere accumulate over time, and it is very evident in Figure 1.1. It is important and interesting to discover the missing sink and understand the mechanism of extra uptake of carbon dioxide by the planet additional to the natural carbon budget before we can manage it.
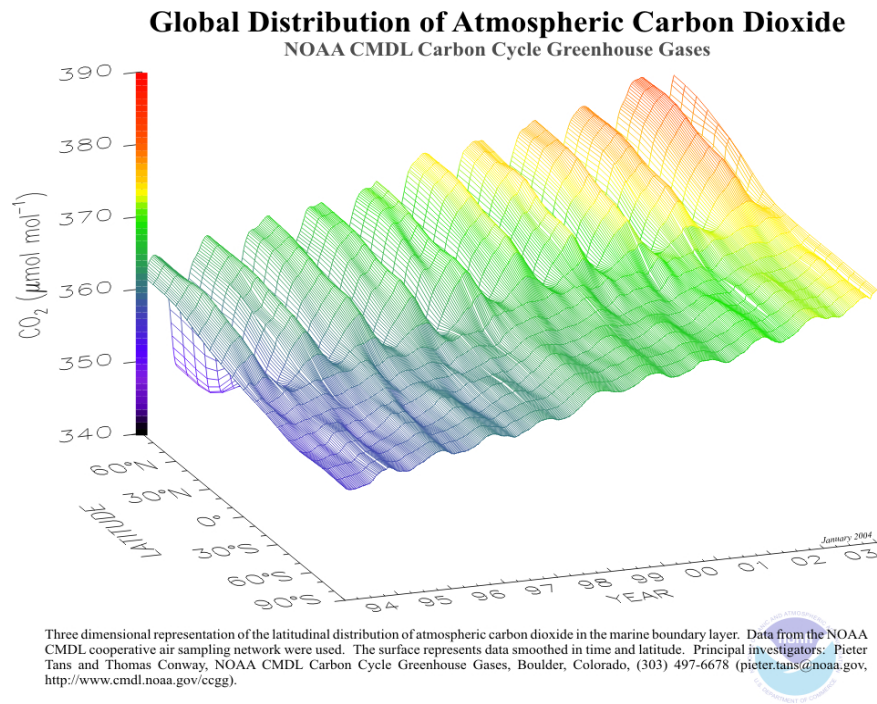
Global Distribution of Atmospheric Carbon Dioxide
NOAA CMDL Carbon Cycle Greenhouse Gases

Three dimensional representation of the latitudinal distribution of atmospheric carbon dioxide in the marine boundary layer. Data from the NOAA CMDL cooperative air sampling network were used. The surface represents data smoothed in time and latitude. Principal investigators: Pieter Tans and Thomas Conway, NOAA CMDL Carbon Cycle Greenhouse Gases, Boulder, Colorado, (303) 497-6678 (pieter.tans@noaa.gov, http://www.cmdl.noaa.gov/ccgg).

Figure 1.2: Meridional distribution of atmospheric CO_2 and its seasonality. From NOAA/CMDL website, http://www.cmdl.noaa.gov/gallery/ccgg_figures.

1.2 Inverse Modeling

Since anthropogenic sources of CO_2 are predominantly concentrated in the northern hemisphere, a north-south CO_2 concentration gradient of four to five ppm should be seen (Tans *et al.* 1990); however, an annual mean observed gradient of three ppm implies the existence of northern hemisphere (NH) sink or southern hemisphere (SH) source (Tans *et al.* 1990). Also the seasonal variation of north-south gradient implies that the response of vegetation to weather seasonality plays an important role in taking up CO_2 during growth

3

seasons (Figure 1.2). Although CO_2 concentration changes seasonally, with higher concentrations in the winter months and lower concentrations in the summer months, the overall CO_2 concentration has continued to increase steadily since the early 1990s. Tans *et al.* suggested that this smaller than expected gradient was most likely due to a carbon sink in boreal or temperate northern continents. Despite the clear existence of NH sink, the strength and temporal/spatial distribution is actually not clear.
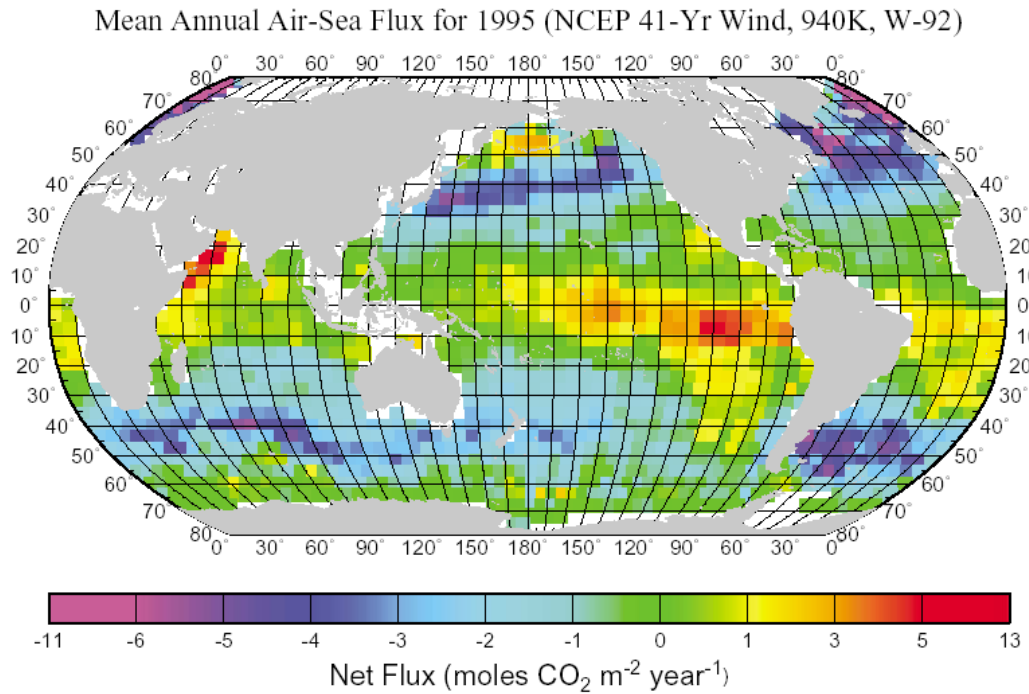

Figure 1.3: 1995 annual mean air-sea CO_2 exchange flux. From Takahashi *et al.* (2002)

Some land surface models, such as the Simplified Biosphere Model (hereafter SiB,

(Sellers *et al.* 1996) and Carnegie-Ames-Stanford Approach (hereafter CASA, Potter *et al.* 1993), model the land surface and simulate CO_2 flux from it at the same time. By

doing so, we can approximately estimate how much CO_2 is taken up and released by the

land surface and its temporal variability. Takahashi *et al.* (2002) utilized about 940,000

measurements of surface-water partial pressure of CO_2 (pCO_2) and calculated mean

annual air-sea flux for 1995 (Figure 1.3), taking into account wind speed, seawater

temperature, and sea-air pCO_2 difference. Andres *et al.* (1996) did tedious calculations to

derive annual anthropogenic CO_2 emission at each latitude and longitude degree by using

fossil fuel consumption, cement manufacture, and population density data. These

estimates are important, because they are based on physical processes. However, we still

need a transport model together with inverse modeling techniques to evaluate and provide

"corrections" to anthropogenic, ocean, and land surface flux estimates, because

uncertainties always exist due to human impacts, unrealistic land surface

parameterizations, non-investigated seawater CO_2 content, etc.

Inverse modeling techniques can help a detailed pattern of fluxes to emerge. Imagine a
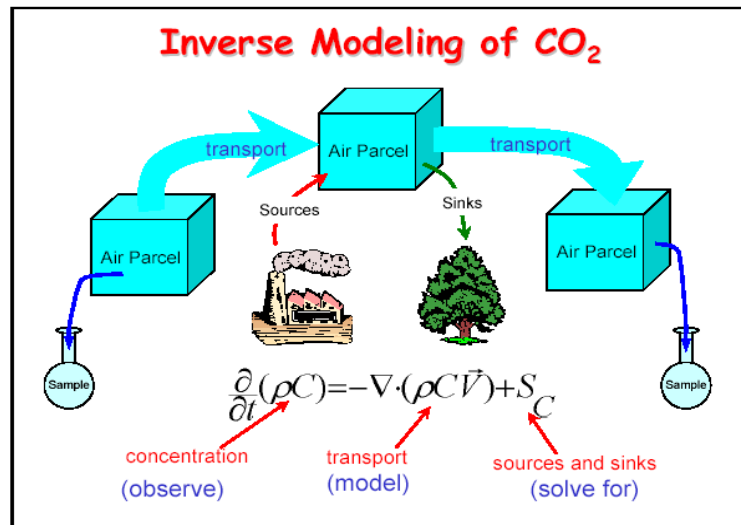
CO_2 stream like Figure 1.4.

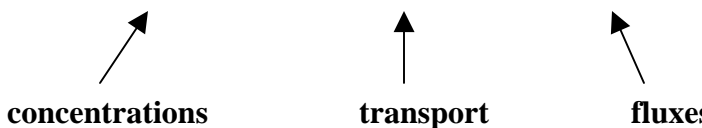**Figure 1.4:** A cartoon for the concept of inverse modeling.

If we have samples of air before and after sources/sinks of CO_2 modify an air parcel, we can subtract the CO_2 concentrations from each other, divide this residual by time and area traversed by the parcel to obtain a flux estimate. Now suppose we have a "perfect" transport model and "perfect" observations, we can calculate a "perfect" estimate.

Let's take a look at the big picture. Suppose we have observations of CO_2 concentration at N locations, and we want to find out the fluxes along M sections that exist between the N points. Extend the idea from Figure 1.3, and we can express the relationship between concentrations, transport, and fluxes in a linear system (Equation 1.1 and Equation 1.2). The same concept applies. If we have observations at those N points and transport

information on the M sections between them, we can invert the transport matrix $\hat{G}$ and get flux vector $\vec{m}$. Transport matrix is the "response" at any of the N locations with respect to any of the fluxes from the M sections, derived from transport information, such as wind velocity, diffusion, convective transport, and eddy flux parameterizations. Therefore, transport matrix has the unit of concentration over flux, which is equivalent to inverse of velocity.
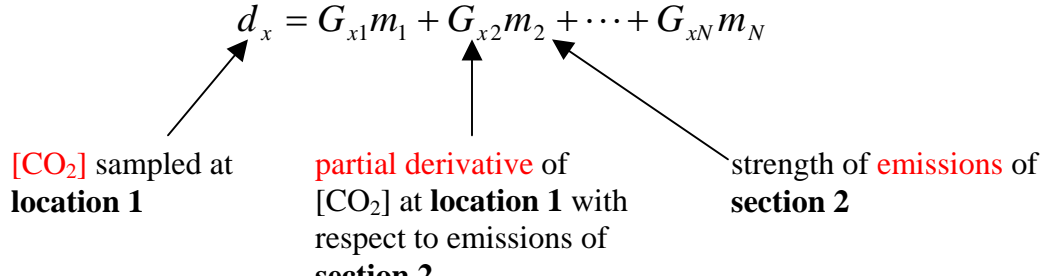
Equation 1.1

$$\vec{d} = \hat{G}\vec{m} \quad \Rightarrow \quad \begin{bmatrix} d_1 \\ d_2 \\ \cdot \\ \cdot \\ d_N \end{bmatrix} = \begin{bmatrix} G_{11} & G_{12} & \cdot & \cdot & G_{1M} \\ G_{21} & G_{22} & \cdot & \cdot & \cdot \\ \cdot & \cdot & \cdot & \cdot & \cdot \\ \cdot & \cdot & \cdot & \cdot & \cdot \\ G_{N1} & G_{N2} & \cdot & \cdot & G_{NM} \end{bmatrix} \begin{bmatrix} m_1 \\ m_2 \\ \cdot \\ \cdot \\ m_M \end{bmatrix}$$

concentrations   **transport**   **fluxes**

Equation 1.2

$$d_x = G_{x1}m_1 + G_{x2}m_2 + \cdots + G_{xN}m_N$$

[CO$_2$] sampled at **location 1**

partial derivative of [CO$_2$] at **location 1** with respect to emissions of **section 2**

strength of emissions of **section 2**

Equation 1.3

$$\vec{m} = \hat{G}^{-1}\vec{d}$$

The procedure is as follows:

1. Decompose total emissions into M "basis functions"

2. Use atmospheric transport model to generate $\hat{G}$

3. Observe d at N locations

4. Invert $\hat{G}$ to find $\vec{m}$

* Note that time dimension is omitted here for convenience

The M basis functions are simply the prescribed regions that will allow CO_2 to be taken up or released. They are not overlapped, and should have no relationship with each other. The number M (how many sections that we prescribe) is arbitrary and dependent on how we can make a "clean cut", so that the prescribed regions are not interdependent.

However, in the real world, it is not that simple. First we have very few observations and they are not "perfect". Until recently, there have been only about 100 sampling locations where "baseline" $[CO_2]$ is collected in flasks every week (NOAA/CMDL Carbon Cycle Cooperative Global Air Sampling Network). Baseline $[CO_2]$ is the concentration from the

ocean background, with well-mixed air and minimum land ecosystem influence; in order to avoid biasing the measurements by local contamination, nearly all the measurement sites are located on remote islands or in rural coastal areas and sample only marine air. Therefore, we obtain measurements that represent the signal from larger areas. The terrestrial signal is still present in such data, but is quite dilute after thousands of kilometers of atmospheric transport. There are also many towers around the world that observe CO_2 concentrations and fluxes in the time scale of minutes (e.g. Baldocchi 2003), but they are greatly influenced by small-scale phenomena, such as boundary layer build-up, mesoscale transport, and turbulence. Secondly, we lack perfect understanding of transport details both in time and space. The information that a transport model can give us is limited by model grid spacing, timestep, and insufficient meteorological data input. Also the information is always not perfect due to the model pitfalls, such as model parameterizations and/or numerical errors, etc. In addition, sampling error, representativeness error, transport simulation error and so on make it impossible to achieve perfect. Therefore, we should not and cannot expect perfect match between observations and model estimates both for concentrations and fluxes.

What we can do is to minimize the "errors" (strictly speaking, they are "differences" rather than "errors") between observed concentrations and model concentrations, and also to minimize the "differences" between the *a priori* flux estimates and the *a posteriori* flux estimates, to some tolerable degree. In other words, *a priori* flux estimates play an important role here, and we have to set up our tolerable criteria for errors or differences.

The inverse method that includes *a priori* information is called Bayesian inverse method.

A priori flux estimates can be obtained from investigations (e.g. Andres *et al.* 1996,

Takahashi *et al.* 2002) or from pre-run surface model output (e.g. Potter *et al.* 1993).

Within the Bayesian inverse method, we use a "cost function" (Equation 1.4) to minimize

the differences. Basically, we combine the mismatch between the *a posteriori* model flux

estimates and the *a priori* flux estimates and the mismatch between the *a posteriori*

model concentration values and observed concentration values into a mathematical

equation (cost function). And then we then try to make this cost function as small as

possible.

Equation 1.4

$$S(m) = \frac{1}{2}\left[\left(\hat{G}\vec{m} - \vec{d}_{obs}\right)^T \hat{C}_d^{-1}\left(\hat{G}\vec{m} - \vec{d}_{obs}\right) + \left(\vec{m} - \vec{m}_p\right)^T \hat{C}_m^{-1}\left(\vec{m} - \vec{m}_p\right)\right]$$

<div align="center">

concentration   *flux*
constraint   *constraint*

</div>

, where S is the "error" cost function, $\hat{G}$ is the transport matrix, $\vec{m}$ is the *a posteriori*

model CO_2 flux, $\vec{d}_{obs}$ is observed CO_2 concentration, and $\vec{m}_p$ is the *a priori* CO_2 flux

estimate. $\hat{C}_d$ is a covariance matrix of the observational data vector $\vec{d}_{obs}$. The inverse of

$\hat{C}_d$, or $\hat{C}_d^{-1}$, is a covariance matrix that is to give confidence level to the observational

data values. $\hat{C}_m$ is the *a priori* flux estimate uncertainty covariance matrix, and the

inverse of $\hat{C}_m$, or $\hat{C}_m^{-1}$, is the covariance matrix to give confidence level to the *a priori*

flux estimates. $\hat{G}\bar{m}$ as a matrix product is the *a posteriori* model concentration. $S(m)$

comprises two main parts. The first part in the bracket on the right hand side is the

concentration constraint, which is resulted from the mismatch between the *a posteriori*

model concentrations and the observed concentrations. The second part in the bracket is

the flux constraint, which is resulted from the mismatch between the *a posteriori* model

flux estimates and our *a priori* "best guess" flux estimates. By minimizing our cost

function, we can get *a posteriori* flux estimates.

TransCom (Gurney *et al.* 2004, Gurney *et al.* 2003) accomplished this idea on a

continental-scale project. They used Carnegie-Ames-Stanford Approach (CASA, a land

surface parameterization) to estimate prior CO_2 flux from the land surface, sea surface

CO_2 flux investigated by Takahashi, and fossil fuel/cement production anthropogenic

emission estimated by Andres. NOAA/CMDL has a CO_2 monitoring network, which has

about 100 observation sites located on remote islands or in rural coastal areas and collects

air samples in flasks every two weeks. CMDL flask data are used as TransCom observed

CO_2 concentrations. In order to compare and evaluate the performances of different

models, they used 12 different General Circulation Models (GCMs) as their transport

models. Figure 1.5 shows their results. The use of Bayesian inverse method can strongly

reduce uncertainties in the area with more observations. Although the Bayesian inverse

technique helps us to understand the location and magnitude of sources and sinks of CO_2,

the technique still requires accurate and precise data, which are quite scarce, especially in

some regions of the world (e.g. the tropics). This let us quantify transport errors and compare to other sources of errors. But as shown in the results, the *a posteriori* uncertainties in equatorial regions are still fairly significant.
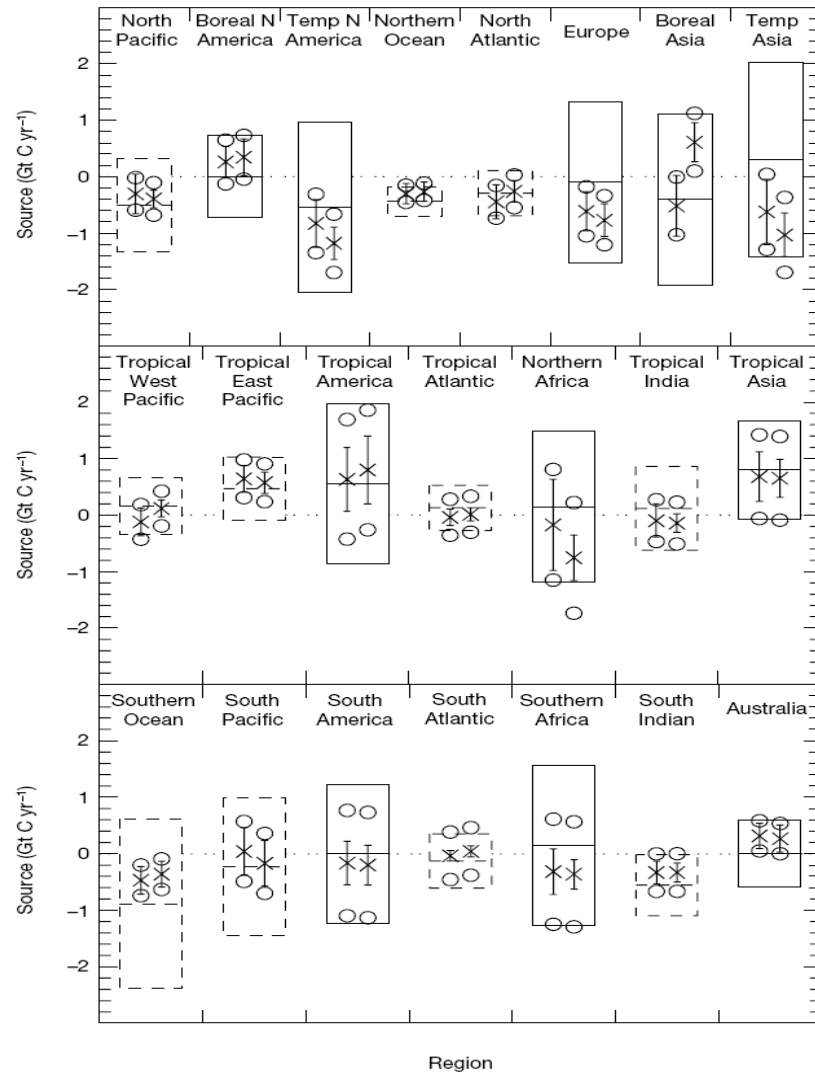

Figure 1.5: *A priori* and *a posteriori* flux estimates and their uncertainties. From Gurney *et al.* (2002), Figure1.

1.3 Paper Review

Lu *et al.* (2001) coupled a biogeochemical model (daily time step CENTURY or DayCENT) with the climate version of Regional Atmospheric Modeling System (ClimRAMS). They drove CENTURY with ClimRAMS meteorological data to calculate leaf area index (LAI) and vegetation transimissivity, and in turn used DayCENT LAI and vegetation transmissivity to update ClimRAMS land surface characteristics. They found that seasonal vegetation phenological variation strongly influences regional climate patterns through its effects on land surface water and energy exchange.

Eastman *et al.* (2001) replaced the RAMS/LEAF (Land Ecosystem-Atmosphere Feedback, RAMS' original land surface submodel) with the General Energy and Mass Transfer Model (GEMTM) and investigated regional weather conditions in the central grasslands of the U.S. for land cover change and double CO_2 scenarios. It was shown that the response of biology to double CO_2 mixing ratio significantly changed regional total accumulated precipitation and vegetation phenology. Local climate and phenology could be influenced even more strongly. Both Lu *et al.* and Eastman *et al.* showed that there was a feedback loop between the ecosystem and the atmosphere, and the interaction is non-linear.

It is clear that vegetation acclimates to elevated CO_2 mixing ratio (e.g. Free Air CO_2 Enrichment project), and the resultant vegetation change may influence regional climate (Eastman *et al.* 2001). However, most of the researches focus on biogeochemical process, climate change, and seasonal or long-term vegetation response. The role of CO_2 on biophysical processes has not been explored yet. In other words, we do not know how CO_2 mixing ratio variation would change energy budget and tracer exchange between the ecosystem and the atmosphere in the short run.

Geels *et al.* (2004) adopted a high-resolution terrestrial biospheric model (the NCAR Land Surface Model, LSM) and a three-dimensional atmospheric transport model (the Danish Eulerian Hemispherical Model, DEHM) to reproduced CO_2 spatiotemporal variation. Their model still has the rigid constraint as in many others: the meteorological data is a given parameter, not a variable. Therefore, although their model simulated the CO_2 variation very well, the model of Geels *et al.* did not possess the predictive skill for either the meteorology or the interaction between the land and the atmosphere.

Chan *et al.* (2004) investigated the CO_2 exchange between the biosphere and the atmosphere by coupling the Mesoscale Compressible Community Model (MC2, Benoit et al. 1997) and the Boreal Ecosystem Productivity Simulator (BEPS, Liu et al. 2002). They showed that synoptic and mesoscale processes caused strong impacts on CO_2 field

evolution. Their research, however, assumed that CO_2 mixing ratio would not change the weather and would not cause the vegetation response to vary.

1.4 Why is it important to simulate a frontal case?

1.4.1 Signals vs. Noise

One of the biggest problems about increasing in-land boundary layer CO_2 observations is how we, data end users, interpret them. If we cannot interpret the data, making more measurements does not bring any benefits. With the emergence of high-frequency tower observations (see Section 1.4.2 and 1.4.3), we are still not capable of explaining every detail of them. Unfortunately, the part that we cannot explain has to be treated as observation "noise". Only the part that we can explain can be seen as "signals". Here is an example.
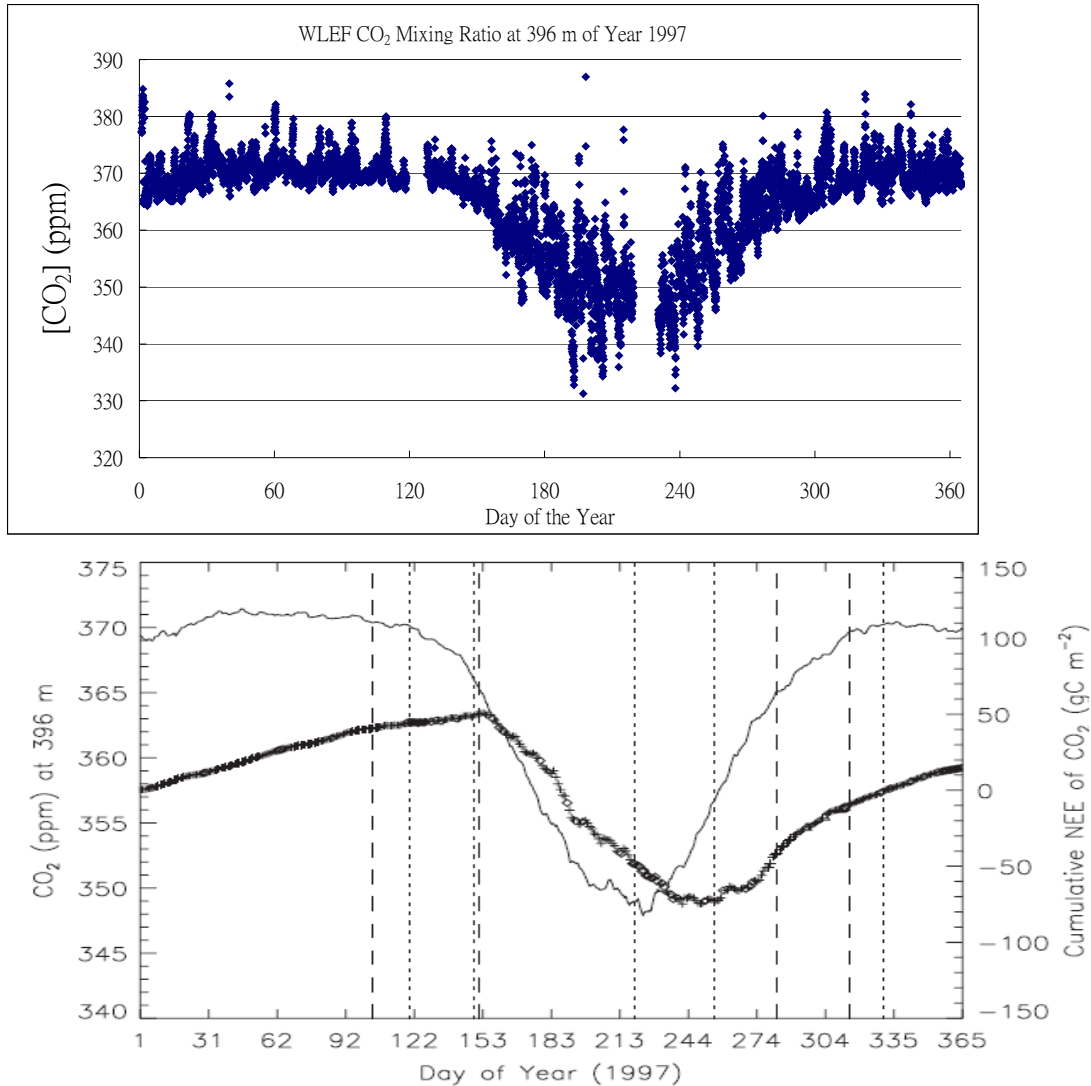
Figure 1.6: CO₂ mixing ratio at 396m of year 1997. Data is from a tower site in northern Wisconsin (WLEF, see case description later). The lower panel is from Davis *et al.* 2003.

For Davis *et al.* the upper panel of Figure 1.6 contains too much information, including synoptic variation, diurnal cycles, local anomalies, etc. Therefore, they have to smooth out the short-term variation and take 30-day running average. The lower panel shows that

they try to use accumulated NEEC (net ecosystem exchange of carbon) to explain local

CO_2 seasonal variability. The tower data is meaningful in the seasonal scale and

meaningless in the weekly or shorter scale. In this situation, the seasonal variability of the

tower data is a "signal" for Davis *et al.* when they only look at the monthly mean, but the

hourly, daily, and synoptic variability is "noise" for them.

1.4.2 Problems of Inverse Modeling Techniques in the Regional Scale

Inverse modeling techniques that use GCMs can help us find out sources/sinks in the

continental scale, but these techniques cannot provide information in the regional scale.

This is because 1) we do not have fine-resolution (both in time and space) of CO_2

observations; 2) the resolution of GCMs is way too coarse to construct regional or even

small-scale features of transport in the models. In addition we "did not" have enough

computer resources to practice inverse modeling techniques for the whole globe with

regional-scale resolution.

Law *et al.* (2002) used high-frequency pseudodata and divided Australia into sub-

continental regions to test the capabilities of a GCM on regional inverse modeling.

Continuous measurements of CO_2 (and possibly other relevant gases) from tall towers

and coastal buoys, in particular, is expected to dramatically improve the degree of

constraint on regional sources and sinks (Law *et al.* 2003). Just as the GCMs can be used

in global inverse modeling, likewise we can apply the same concepts in using a regional

model (instead of a GCM) to find regional sources or sinks of CO_2. With appropriate

boundary conditions, we can narrow down the scope of spatial pattern and temporal

variation of sources/sinks to a much smaller area. However, the same problem will also

appear in this downscaling approach. That is, without enough observations the *a*

posteriori uncertainty can still be large, just like what happens to the flux estimation near

the equator in TransCom 3 (Gurney *et al.* 2002).

Global tracer transport models may have insufficient spatial resolution to make the best

use of the dense hourly sampling network envisioned under NACP (The North American

Carbon Program, Figure 1.7). Currently available global weather analyses are inadequate

for driving regional transport models due to insufficient resolution in both time (Δt is

typically 3 to 6 hours) and space (Δx is typically 100-250 km), and the standard practice

of interpolation to standard pressure levels fails to conserve mass. These products are

simply not intended for the purpose of driving quantitative trace gas transport
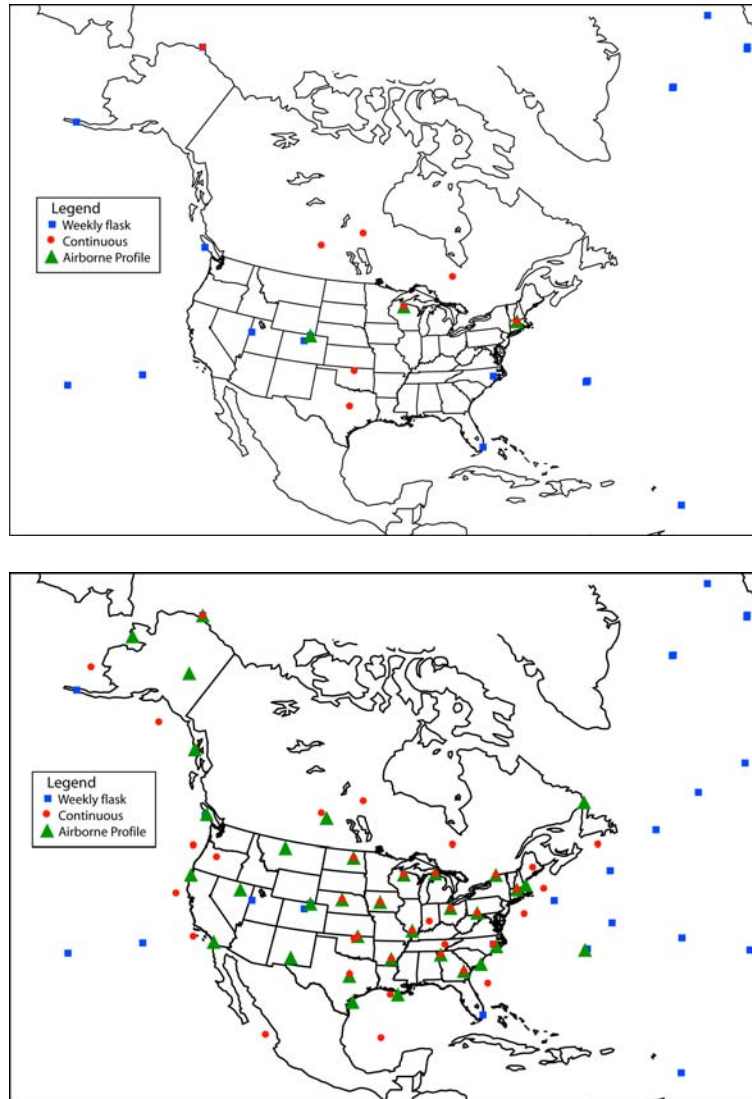
calculations.

Figure 1.7: The NACP CO_2 concentration measurement network. The upper panel is for the present and the lower one is for the near future.

1.4.3 New Era for Regional Inverse Modeling

The atmospheric observing system is expected to undergo dramatic enhancement in the second half of this decade (Fig 1.7) as global observing programs (Bender *et al*. 2002), NACP (Wofsy and Harris, 2002), and a similar effort in Europe (CarboEurope Integrated Project, 2003) deploy additional stations. The density of the enhanced in-situ observing

system should enable source/sink estimation to a high degree of confidence over much finer spatial scales than has been possible to date. Hourly observations exhibit large variations associated with synoptic weather events (e.g. Hurwitz *et al.* 2004) that can be used to estimate upstream fluxes as the fetch changes due to passing weather disturbances. Inland observed $[CO_2]$ are strongly influenced by vegetation and weather conditions as has been shown in Hungarian measurement site (Haszpra 1995). As enhanced observations enable fluxes to be estimated at finer temporal and spatial resolution, atmospheric transport errors are likely to become more problematic. We need a more sophisticated atmospheric model, which can generate fine-resolution transport information, to distinguish signals from noise in the high-frequency measurements.

To obtain maximum value from the emerging temporally and spatially dense observing systems, a new approach is needed, in which state-of-the-art data analysis is applied to produce custom meteorological analyses in support of carbon cycle research, rather than relying on standard products intended for weather forecasting. Unlike the weather forecast problem, carbon cycle data assimilation has the luxury of time – weeks or months may elapse after samples are collected before final quality-controlled data are available for analysis. The carbon data assimilation problem also requires very careful treatment of diurnal variability of terrestrial ecophysiology, boundary-layer turbulence, and cumulus convection. In short, we need to control the details of our own modeling environment rather than rely on "off-the-shelf" meteorological products to drive offline carbon cycle models and inverse calculations. This will require a major research effort to develop both appropriate forward models and assimilation techniques to make use of the

wide variety of observations available.

1.4.4 Other Issues about Regional Modeling

Most of our [CO_2] measurements are taken in the boundary layer once every two weeks along the seashores or on remote islands (NOAA/CMDL network) or taken every few minutes on the towers; neither of these methods can capture the big picture of synoptic/mesoscale CO_2 variability, which is determined by transport and the response of vegetation to synoptic weather systems. CMDL intends to measure marine CO_2 concentration, while towers measure concentration at single points. The footprint of flux measurements is only a few kilometers, depending on wind speed, instability, surface roughness length, and tower heights (Schmid 2002). Thus, multiple-scale simulations must be done in order to integrate these signals of flux or concentration from different scales. A regional model with nesting techniques has the downscaling capability to perform such simulations.

Before we can actually perform a regional inverse modeling experiment, we must run a forward model to design it. Without a successful forward model, we can never justify its adjoint model or evaluate the regional inverse modeling technique.

1.4.5 The Importance of this Case Study

Over all, the importance of regional modeling is clear. First, with dramatically increasing

observations, we need to distinguish signals from noise. Secondly, successful regional forward modeling is necessary before we can perform regional inverse modeling to quantify regional-scale CO_2 source and sink. A regional forward model is a tool to evaluate the performance of its counterpart regional inverse model. This case study is a benchmark to address the issues mentioned above and makes its existence important.

1.5 Model Coupling and Case Study

In this research, SiB 2.5 and BRAMS (Brazilian Regional Atmospheric Modeling System) are used. SiB is a land surface model that is driven by weather parameters, such as precipitation, solar radiation, temperature, etc. BRAMS is a new regional atmospheric model adapted from the latest version of RAMS (Regional Atmospheric Modeling System 5.04) with Grell convection scheme and shallow convection scheme (Grell *et al.* 1995) implemented in it. Freitas *et al.* (personal communication) coupled SiB 2.5 with BRAMS and allowed tracer transport by Grell and shallow convection scheme. Thanks to profound land surface investigation, data integration technique, and satellite monitoring, soil class map of 10 km resolution and biome type map and NDVI (Normalized Difference Vegetation Index) map of 1 km resolution are available and make it possible to do a sophisticated mesoscale simulation.

In this thesis, I shall present a case as mentioned above, in which CO_2 enrichment occurs during a frontal passage. In next chapter, experimental design will be discussed, which includes data preparation, model descriptions, coupling issues, and model configurations.

In Chapter 3, the results will be shown and there will be some discussion. In the last chapter, some conclusion will be made, and possible future work will be discussed.

Chapter II   Experimental Methods

2.1 Model Description

2.1.1 SiB Description

The Simple Biosphere (SiB) Model is a land surface model developed by Sellers and his colleagues (Sellers *et al.* 1996a, Sellers *et al.* 1996b) and originally designed as the land surface component of the Colorado State University General Circulation Model (CSU GCM), but its capability is good for mesoscale modeling as well (Denning *et al.* 2003). The details about SiB 2.5 (version 2.5) are described quite clearly in the papers of Sellers *et al*. A big-picture view of the model follows.

SiB 2.5 uses three major concepts in its model implementation: entities, exchanges of tracer/energy between entities, and semi-empirical formulas for photosynthesis and respiration. The entities are the atmosphere at the reference height (ARH), canopy air space (CAS), canopy, water puddles, and the ground/soil. There are water vapor/latent heat (LH), sensible heat (SH), and carbon exchanges between ARH and CAS, between CAS and canopy, and between CAS and the ground. In addition, there is water/LH exchange between water puddles and CAS, and between the ground and the air directly

above the ground. Semi-empirical formulas for photosynthesis and respiration will be described later.

SiB 2.5 is driven by 1) wind speed at ten meters above the ground, 2) temperature at two meters, 3) relative humidity at two meters, 4) total incident solar radiation, and 5) precipitation.

Figure 2.1 shows the framework of SiB 2.5, including entities and exchanges between them. Note that how photosynthesis and respiration work is not shown due to space limitation.
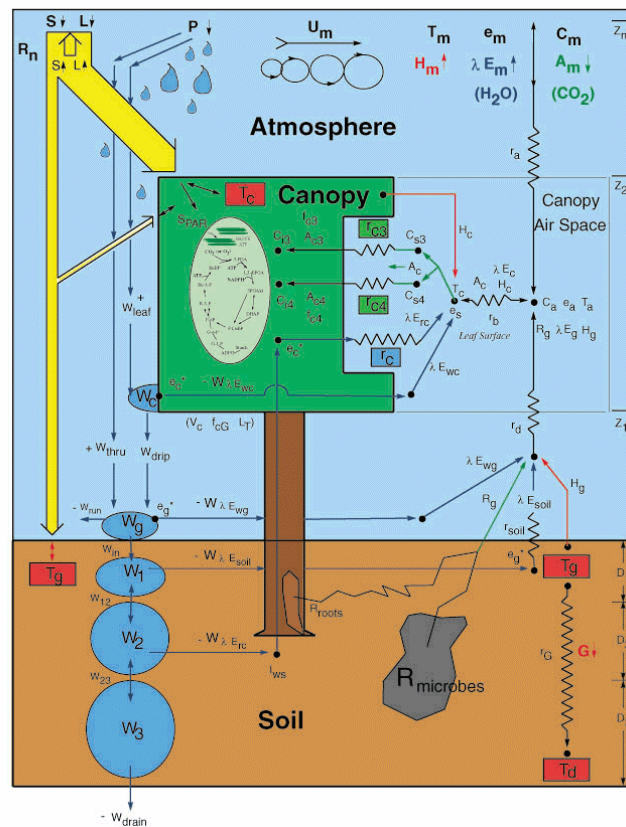

Figure 2.1: Framework of SiB 2.5 model.

2.1.1.1 The Ground/Soil

There are three layers for soil water content: surface layer, root zone, and recharge zone. Soil moisture in the first layer (W_1) is recharged by the infiltration of precipitation into the upper soil moisture store (W_{in}), depleted by the flow between surface layer and root zone (W_{12}), and evaporated to the air right above the ground ($W_{\lambda E_{soil}}$). Soil moisture in the second layer (W_2) is determined by the flow between surface layer and root zone (W_{12}), the flow between root zone and recharge zone (W_{23}), and flow from the soil to the root system ($W_{\lambda E_{rc}}$). Soil moisture in the third layer (W_3) is determined by the flow between root zone and recharge zone (W_{23}), and gravitational drainage from recharge soil moisture store (W_{drain}).

SiB 2.5 has seven layers for soil temperature. For deep soil, soil temperature is influenced by heat diffusion between soil layers. The equation for soil energy of the top layer takes into account absorbed net radiation (R_n), latent heat flux (λE_{soil}), sensible heat flux (H_g), heat diffusion from the top layer to deep layer, and energy transfers due to phase changes of surface water/snow/ice.

2.1.1.2 Exchange Formulas

No matter the exchanges occur between the ARH and the CAS, between the CAS and the soil, or between leaf surface and the CAS, the exchange equations share a similar form, which is

$$\text{flux} = \frac{\text{potential difference}}{\text{resistance}}$$

The potential difference for SH is the product of air density (ρ), specific heat of air at constant pressure (c_p), and temperature difference between the two entities (ΔT) that are communicating. Therefore, SH flux has the form:

$$H = \frac{\rho c_p \Delta T}{r_H},$$

where H is SH flux and r_H is the resistance for SH flux and must be parameterized.

Similarly, the potential difference for LH is the product of air density (ρ), specific heat of air at constant pressure (c_p), and vapor pressure difference between the two entities (Δe), divided by psychrometric constant (γ). So, LH flux has the form:

$$\lambda E = \frac{\rho c_p \Delta e / \gamma}{r_{\lambda E}},$$

where λE is LH flux and $r_{\lambda E}$ is the resistance for LH flux and is parameterized similar to r_H.

For CO_2 flux, the potential difference is the CO_2 concentration difference between the two entities (ΔC) divided by atmospheric pressure (p). It has the form:

$$A = \frac{\Delta C / p}{r_A},$$

where A is CO_2 flux and r_A is the resistance for carbon dioxide exchange. Notice that r_H, $r_{\lambda E}$, and r_A can be different from each other by some simple ratio. The idea of total resistance of a series of resistors applies to this concept just as it does to electric circuits.

2.1.1.3 Energy Exchange with the Atmosphere

The exchanges of water/LH, SH, and CO_2 exist between the ARH and the CAS. In our coupled model, the ARH is the lowest level of our atmospheric part. Therefore, the interface between the atmosphere and the land surface is actually the exchange between the CAS and the ARH. SH and water/LH exchanges between the land surface and the atmosphere are

$$H_c + H_g = \frac{(T_a - T_m)\rho c_p}{r_a}$$

and $\quad \lambda E_c + \lambda E_g = \frac{(e_a - e_m)\rho c_p / \gamma}{r_a},$

where H_c is SH flux from the leaf surface to the CAS, H_g is SH flux from the ground to the CAS, T_a is the CAS temperature, T_m is the ARH temperature, λE_c is the LH flux from the leaf surface to the CAS, λE_g is the LH flux from the ground to the CAS, e_a is the CAS water vapor pressure, e_m is the ARH water vapor pressure, and r_a is the aerodynamic resistance between the CAS and the ARH. The subscript 'c' denotes canopy (leaf) values, 'g' denotes ground values, and 'm' denotes the mixed layer (the atmosphere

at the reference height). Because we assume sensible heat does not accumulate in the canopy, SH flux from the CAS to the ARH is equal to the sum of H_c and H_g. Similarly, LH flux from the CAS to the ARH is equal to the sum of LH flux from the leaf surface to the CAS, LH flux from the ground surface water puddles, and LH flux from the ground to the CAS. The resistance is determined by an empirical function:

$$r_a = \frac{\left[\frac{1}{k}\ln\left(\frac{z_m - d}{z_0}\right)\right]^2}{u_m},$$

where z_m is the reference height, k is Von Karman constant, d is the canopy zero plane displacement, z_0 is the canopy roughness length, and u_m is the friction velocity.

2.1.1.4 Leaf-level Photosynthesis and Respiration

The Ball-Berry-Collatz Equation (Collatz *et al.* 1992, Collatz *et al.* 1991) links photosynthesis and leaf-level conductance ($g_s = 1/r_c$) together as follows:

$$g_s = m\frac{A_n h_s}{C_s}p + b,$$

where A_n the is leaf-level net photosynthesis rate, h_s is the relative humidity on the leaf surface, C_s is CO_2 pressure at the leaf surface, p is the air pressure, and m and b are the slope and intercept to fit this straight line equation. This empirical equation allows us to calculate conductance or resistance between the chloroplast and leaf surface if we have good photosynthesis rate estimation. Knowing the conductance, we can calculate the water/LH and CO_2 exchange at the leaf surface.

In the Farquhar-Berry Model, photosynthesis rate is parameterized as follows:

$$A_n = \min(A_c, A_L, A_s) - R_d,$$

, where A_c is enzyme kinetic limitation for photosynthesis, A_L is light limitation, A_s is starch limitation, and R_d is autotrophic respiration. Nitrogen is a limiting nutrient in plants, and A_c is proportional to leaf nitrogen concentration; plants cannot allocate all of their nitrogen to leaves, and also their ability to regenerate ribulose-bisphosphate carboxylase-oxygenase (RUBISCO, the ezyme that fixes carbon from the air) after it reacts with oxygen or carbon dioxide is limited by nitrogen content. A_L limitation comes from the plant available light, so it is controlled by the weather and solar angle. A_s is determined by starch consumption and re-allocation after the vegetation produces it. There is a trend to slow down photosynthesis when starch accumulates on leaves. All the three limitations are also regulated by soil water stress and leaf surface temperature stress.

Autotrophic respiration (R_d) is the sum of "maintenance respiration" and "growth respiration". Maintenance respiration results from what plants must do to function well and maintain their lives. In SiB 2.5, only maintenance respiration of leaves is calculated separately; growth respiration and other form of maintenance respiration, for example maintenance respiration of root systems and stems, are combined with heterotrophic respiration as a single quantity (see ground respiration in the next section).

2.1.1.5 Ground Respiration and Leaf Respiration

Ground respiration (R_g), composed of autotrophic respiration from the root system and heterotrophic activity, is determined by both soil temperature and soil moisture in the model. While there is optimal soil moisture for ground respiration for each of the soil types, soil temperature scales ground respiration by a "Q-10" relationship:

$$\text{scale ratio} = \exp\left[\ln(Q_{10})\frac{T-298}{10}\right];$$

that is, respiration increases "Q_{10} times" when soil temperature increases by 10 degrees. A similar idea applies to leaf respiration, although it is leaf surface temperature that causes the Q-10 effect in this regard. Q_{10} ranges from 1.6 to 2.4 in SiB 2.5 for different respiration of the ecosystem and is determined by extensive field experiments.

Another scale factor for ground respiration, called respiration factor, must be specified to the soil to scale the amount of CO_2 that is released from the ground. Respiration factor is given so that annual net photosynthesis (photosynthesis minus respiration) is zero. In other words, SiB 2.5 assumes there is no CO_2 uptake on an annual basis, because we still know little about carbon pools and their rate of change (probably very small from the perspective of land carbon storage). It will be shown how to get respiration factor for my experiment Section 2.3.2.2.

2.1.1.6 Flora-Level Photosynthesis

Photosynthesis for the whole domain can be obtained from the extension of leaf-level

photosynthesis. First, photosynthetically active radiation (PAR) as a function of canopy

depth (vertical direction) is assumed to be an exponential function decreasing downward:

$$PAR = PAR_0 e^{-kLAI},$$

where PAR_0 is the PAR at the top of canopy, k is an empirical constant, and LAI is the

leaf area index, accumulated from the top of canopy down to some point in the canopy.

The function simply says that solar radiation within the canopy is absorbed by leaves in

an exponential way as a function of depth. We then assume that plants allocate their

nitrogen (the resource for photosynthesis) accordingly. Therefore,

$$A = A_0 e^{-kLAI} \quad \text{and} \quad g_c = g_{c,0} e^{-kLAI},$$

where subscript 0 denotes canopy top. Photosynthesis and conductance decrease

downward as an exponential function. And we define:

$$\int_0^{L_T} e^{-kLAI} dLAI = \frac{1}{k}\left(1 - e^{-kL_T}\right) = \frac{FPAR}{k},$$

where L_T is accumulated LAI for the whole canopy and is derived from NDVI

(Normalized Difference Vegetation Index). FPAR, defined as $\left(1 - e^{-kL_T}\right)$, is "fractional

photosynthetically active radiation". Hence, for any grid cell with FPAR, we can

calculate the average photosynthesis rate and conductance for the whole grid cell as

follows:

$$\overline{A} = A_0 \frac{FPAR}{k} \quad \text{and} \quad \overline{g_s} = g_{s,0} \frac{FPAR}{k}.$$

Furthermore, by using NDVI, we can add up the photosynthesis in each grid cell to obtain photosynthesis for the whole simulation domain. Note that the equations used here are their simplified forms that do not deal with non-green leaves or vegetation clumping.

2.1.1.7 Inputs to SiB 2.5

SiB 2.5 requires input parameters including a soil map, vegetation map, and NDVI map (from satellite) as surface characteristics and parameterizes latent heat flux, sensible heat flux, surface albedo, upward longwave radiation, and photosynthesis together with CO_2 flux. The role of NDVI will be discussed in Section 2.2 (Data Preparation section).

2.1.2 BRAMS Description

Regional Atmospheric Modeling System (RAMS) is a regional model developed at Colorado State University. RAMS has successfully simulated many atmospheric phenomena including mesoscale convective systems, thunderstorms, hurricanes, airflow around buildings, etc. (Cotton *et al.* 2002, Pielke *et al.* 1992) The following description of RAMS is adapted from the RAMS Technical Description, which is available at RAMS website. Note that only the non-hydrostatic mode and the numerical schemes that are used in this research are described. RAMS/LEAF (Land Ecosystem-Atmosphere Feedback, the land surface submodel in RAMS) and how it is initialized are not described, since LEAF is replaced with SiB in this work. The original convection scheme (Kuo scheme), and soil/vegetation parameterizations in the coupled model are replaced, so I

have omitted their descriptions as well. Note that the replacement of the Kuo convection

scheme with the Grell convection scheme, as discussed in Section 2.1.2.8 changes the

model name from RAMS to BRAMS (Brazilian RAMS).

2.1.2.1 General Concept

RAMS uses an Eulerian modeling approach. Its general equations have the form as below:

$$\frac{\partial A}{\partial t} = -u\frac{\partial A}{\partial x} - v\frac{\partial A}{\partial y} - w\frac{\partial A}{\partial z} + S \, ,$$

where A is the variable that is of interest, u is x-direction velocity, v is y-direction

velocity, and w is vertical velocity. S is force for momentum equations, or energy

source/sink for the thermodynamic equation, or water source/sink for the water species

mixing ratio continuity equation, and so on. Mass conservation is enforced by the

following form of the mass continuity equation:

$$\frac{\partial \pi'}{\partial t} = -\frac{R\pi_0}{c_v \rho_0 \theta_0}\left(\frac{\partial \rho_0 \theta_0 u}{\partial x} + \frac{\partial \rho_0 \theta_0 v}{\partial y} + \frac{\partial \rho_0 \theta_0 w}{\partial z}\right)$$

, where π is the Exner function, R is the universal gas constant, c_v is the specific heat

of dry air at constant volume, ρ is air density, θ is potential temperature, and u, v, and

w are wind velocities. The subscript 0 denotes the value at a reference level, and the

prime denotes a perturbation. All variables are grid-volume-averaged quantities, while

the overbar has omitted for conciseness. The Exner function is a pressure-like variable,

and is defined as:

$$\pi = c_p\left(\frac{p}{p_0}\right)^{\kappa} \, ,$$

34

where c_p is the specific heat of dry air at constant pressure, and $\kappa = c_v / c_p$.

For the non-hydrostatic model, RAMS uses forward time differencing for the thermodynamic variables and leapfrog differencing for the velocity components and pressure.

2.1.2.2 Grid Structure

RAMS uses the staggered Arakawa C grid (Mesinger and Arakawa 1976). All mass-related variables are located at the center of the grid cell, while y-direction velocity is located 1/2 Δy to the north and south of the center, and x-direction velocity is located 1/2 Δx to the east and west. The horizontal grid uses a rotated polar stereographic projection. The vertical structure employs the σ_z terrain-following coordinate (Clark 1977). The mapping between the vertical velocity component and the horizontal velocity components is considered. Vertical levels can be defined by the user or set to geometrical-increasing upward. By doing this, near the ground the model can have very small vertical level spacing to resolve boundary layer phenomenon, while aloft it adopts large vertical level increments to save computer resources.

2.1.2.3 Nesting

A feature of RAMS we are making use of in this work is grid nesting. While a parent grid (PG) covers a larger domain and uses larger grid spacing, the nested grids (NGs) focus on

a smaller domain under intensive investigation and use finer spacing to resolve smaller features.

RAMS grid nesting technique is described in Clark and Farley (1984) and Clark and Hall (1991). The technique applies two-way communication of all prognostic variables between any NG and its PG. To conserve the volume integrals of density-weighted quantities (such as potential temperature and moisture) between grids, they are multiplied by density prior to their communication from either grid to the other. An NG has shorter time step than its parent. The PG marches its prognostic variables forward by one time step first. The updated values of the PG are then interpolated in time to match the time step of its NG, and interpolated in space to match the NG cell size. The values of prognostic variables along the boundary of the NG are replaced by the values from the interpolation (both in time and space) of its PG. On the other hand, the NG is then updated in a series of smaller time steps until it catches up to the simulation time of the PG. The averages of the prognostic variables over each set of the NG cells, which occupy a single PG cell, replace the values of the prognostic variables for that PG cell.

2.1.2.4 Boundary Conditions

Regional models would require boundary conditions to constrain the simulation. For the normal velocity (the velocity perpendicular to the boundary), the general form of the boundary condition is the basic radiative condition:

$$\frac{\partial u}{\partial t} = -(u + c)\frac{\partial u}{\partial x},$$

where u is the velocity in the x-direction and is normal to the western and eastern

boundaries. Phase velocity, c is based on the Orlanski (1976) scheme, the modified

Klemp and Lilly scheme (Klemp and Lilly 1978), or the Klemp and Wilhelmson (1977)

scheme.

The variables other than the normal velocity are defined 1/2 Δx or Δy away from the

normal velocity components, and the boundary conditions that can be assigned for them

include zero gradient conditions, constant inflow and/or outflow conditions, or radiative

outflow conditions. For the top boundary, a simple wall ($w = 0$) or the Klemp and Durran

(1983) gravity wave radiative condition applies.

2.1.2.5 Boundary Nudging

The prognostic fields (u, v, θ_{il}, π, and r_T) can be nudged toward observational data or

reanalysis data to implement four-dimensional data assimilation (4DDA) or boundary

nudging. 4DDA is not discussed here, because it is not used in this research.

Boundary nudging serves two purposes: 1) to introduce time-varying information about

external forcing into the model domain, and 2) to damp information propagating from the

interior toward the lateral boundary. Usually nudging only applies on the lateral boundary

regions of the coarest grid. The nudging term can be written as:

$$\frac{\partial \phi}{\partial t} = \frac{\left(\phi_{obs} - \phi_m\right)}{\tau},$$

where ϕ is the desired variable, the subscripts "obs" and 'm' denote observational data and model data respectively, and τ is the nudging timescale. The larger τ is, the weaker the nudging strength is.

2.1.2.6 Data Analysis

For simulations using observational data to start a run or exchange exterior forcing with the interior, RAMS needs data for initial conditions and lateral boundary information. Various observational and reanalysis data, such as NCEP Eta reanalysis data, NCEP/NCAR reanalysis data, rawinsondes, and surface observations, can be processed with a mesoscale ISentropic ANalysis package (RAMS/ISAN package, Tremback 1990). ISAN adopts a "hybrid" vertical coordinate, a mixture of isentropic and the terrain-following σ_z coordinates. ISAN uses the σ_z terrain-following coordinate in the lowest layer, whose depth (usually the depth of the boundary layer) can be assigned by the user, to avoid the problem of intersection between the ground surface and isentropes and to avoid the problem of small vertical increasing or even decreasing potential temperature in the planetary boundary layer (PBL). To keep the advantages of isentropic coordinates, blending is adopted in the transition layer from σ_z coordinate to isentropic coordinate, while pure isentropic data analysis is used aloft.

2.1.2.7 Parameterizations

A turbulent mixing parameterization, surface layer parameterization, soil and vegetation

parameterizations, convection parameterization, and radiation parameterization are used

in RAMS.

a. Eddy Flux Parameterization

RAMS uses K-theory to parameterize the unresolved transport of the prognostic variables

due to turbulent mixing. In K-theory

$$\left(\frac{\partial u_j}{\partial t}\right)_{turb} = \frac{\partial}{\partial x_i}\left(\overline{u_i'u_j'}\right) = \frac{\partial}{\partial x_i}\left[-K_{mi}\left(\frac{\partial u_i}{\partial x_j}+\frac{\partial u_j}{\partial x_i}\right)\right]$$

$$\left(\frac{\partial \phi}{\partial t}\right)_{turb} = \frac{\partial}{\partial x_i}\left(\overline{u_i'\phi'}\right) = \frac{\partial}{\partial x_i}\left[-K_{hi}\left(\frac{\partial \phi}{\partial x_i}\right)\right]$$

where u_i is the momentum in i direction, x_i is i-direction coordinate, ϕ represents the

scalar of interest, K_{hi} is the eddy mixing coefficient for scalars which applies to the i-

direction, and K_{mi} is the eddy mixing coefficient for momentum which applies to the i-

direction. Subscripts i and j indicate the directions, while the prime indicates the

deviation from Reynolds average. RAMS allows the user to choose the appropriate eddy

mixing coefficient, K, from various turbulent mixing parameterizations. They include,

but are not limited to, the parameterizations of Mellor-Yamada, Horizontal Deformation,

Deardorff, etc.

b. Radiation Parameterizations

Harrington (1997) two-stream radiation scheme is used in this study. The two-stream

equation adopts matrix forms its solution follows adding method (Liou 1992). Three solar

radiation bands and five infrared bands are considered. The model uses the Fast

Exponential Sum-Fitting (FESFT) method of Ritter and Geleyn (1992) for computing the

absorption by gaseous CO_2, H_2O, and O_3. Band limits, Rayleigh scattering, and

continuum absorption calculations are included. Cloud optical properties are computed

for each form of condensate (cloud water, rain, pristine ice, snow, aggregates, graupel,

and hail) as well as water vapor. The extinction coefficient and absorption coefficient for

liquid water drops are computed following Mitchell's (1997) modified Anomalous

Diffraction Theory (ADT) method. For ice phase hydrometeors, the extinction coefficient

and absorption coefficient for hexagonal plates, hexagonal columns, and rosettes are

calculated following Mitchell and Arnott (1994). For the bulk microphysical model,

gamma distribution functions for the hydrometeors are assumed (same as in mirophysics

parameterization, see below) and the optical properties are averaged over each band using

the method of Slingo and Schrecker (1982). For the bin microphysical model, optical

properties are computed for each bin of the hydrometeor distribution functions at the

mean size of a given bin.

c. Microphysics Parameterization

Microphysics parameterization of RAMS is implemented by the Cotton group of CSU. Different levels of microphysics parameterization can be used according to the details of the particular experiment. A higher level marches microphysics variables forward in a more prognostic way. Usually, the highest level of the bulk microphysics parameterization is used; this level handles cloud water, rain, pristine, ice, snow, aggregates, graupel, and hail diagnostically or prognostically according to the user's choice. Cloud concentration nuclei (CCN) and the nuclei for snow, aggregates, graupel, and hail can be provided as input or prognosed, while pristine ice number concentration must always be prognosed. The shape of the gamma distributions of all hydrometeors must be specified. This parameterization includes the physical processes of nucleation of ice crystals, collisions, evaporation, condensation, sublimation, freezing, melting, shedding, sedimentation, etc., especially precipitation.

d. Surface Flux Parameterization

Surface LH and SH flux parameterizations are designed and implemented following the methodology in SiB 2.5 as discussed, while momentum flux parameterization is implemented following the methodology in RAMS.

Momentum flux is implemented as follows.

$$\overline{w'u'} = -(a^2 F_m)u^2$$

$$a^2 = k^2 / (\ln \frac{z}{z_0})^2,$$

where u is the horizontal wind speed, w is the vertical velocity, $\overline{w'u'}$ denotes the time

mean transient vertical momentum flux of the horizontal wind, a is the drag coefficient

in neutral conditions, k is the von Karman constant, z is the height of interest, z_0 is

roughness length, and F_m is defined as below.

For stable conditions:

$$F_m = \frac{1}{\left[1 + 10R_{iB}/(1 + 5R_{iB})^{1/2}\right]}$$

(Louis 1979)

For unstable and neutral conditions:

$$F_m = 1 - \frac{10R_{iB}}{1 + 75a^2(\frac{z}{z_0} \times |R_{iB}|)^{1/2}}$$

(Holtslag and Boville 1993)

R_{iB} is bulk Richardson number and can be calculated from vertical wind shear and local

lapse rate of temperature.

2.1.2.8 The Grell Scheme and Parameterization of Shallow Convection
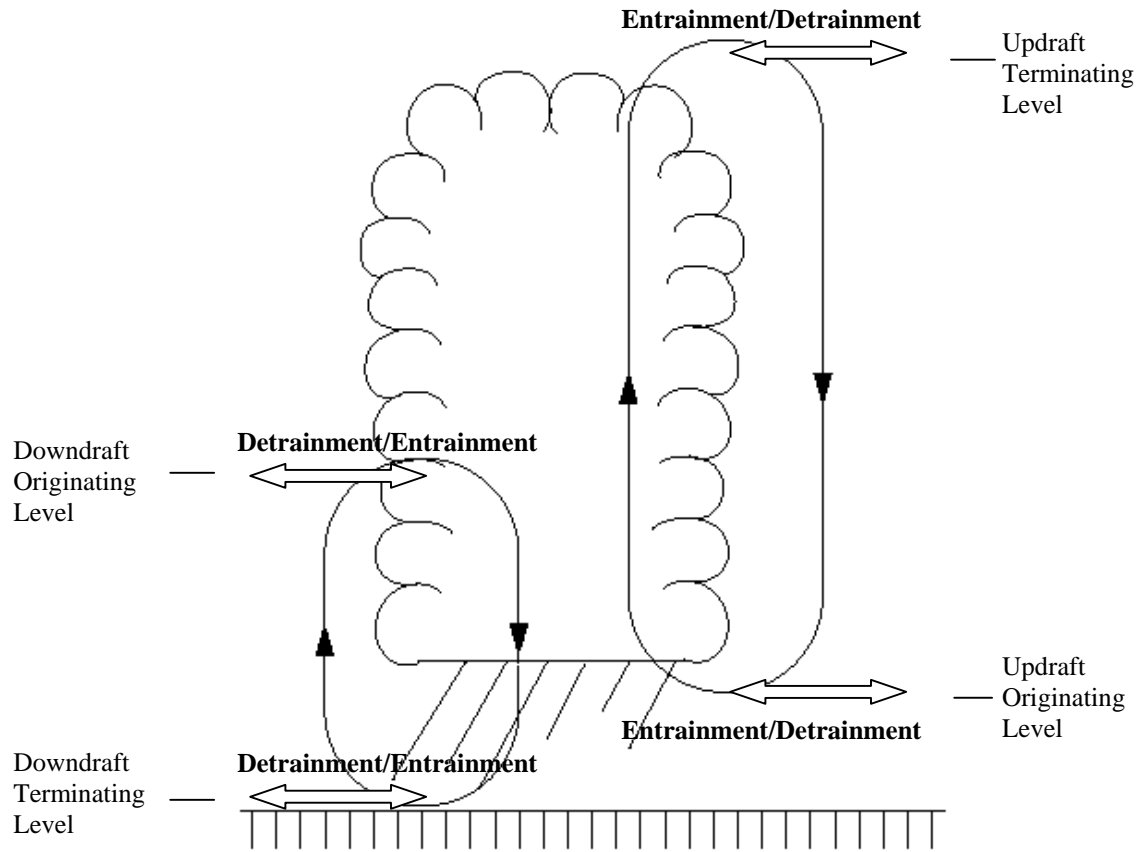
Figure 2.2: Framework of Grell Scheme.

The Grell scheme (Grell 1993, Grell *et al.* 1991) is used in this research as the convective

parameterization. This scheme assumes that deep convective clouds are all of one size.

Two steady-state circulations, caused by an updraft and a downdraft, comprise one cloud.

Since the scheme ignores entrainment and detrainment except at the levels of origin or

termination of updrafts and downdrafts, the Grell scheme is suitable for a grid cell as

small as 10-12 km and it is not necessary to assume that the fractional area coverage of

updrafts and downdrafts in the grid column is small (Pielke Sr. 2002). Mass flux between

the levels of origin and termination of updrafts and downdrafts is constant, and the

originating mass flux of the downdraft is made a function of the updraft mass flux and the reevaporation of convective condensate. The concepts of moist static energy tendency and available buoyant energy for stabilization/destabilization are used throughout the scheme.

The shallow convection scheme parameterizes PBL-forced shallow non-precipitating convection as well as mid-tropospheric shallow convection caused by other subgrid-scale effects (Grell *et al.* 1995). It is assumed to be forced by PBL energy fluxes or radiational cooling tendencies. This parameterization has strong lateral mixing, does not have convective downdrafts, and causes no precipitation. Its mass flux is determined based on cloud-work function (the kinetic energy generation per unit cloud-base mass flux).

Grell and Freitas et al. (personal communication, University of San Paul, 2004) implemented the Grell and shallow convection schemes in RAMS and called it Brazilian Atmospheric Modeling System (BRAMS). In the latest version of BRAMS, the Grell scheme can transport passive tracer, which was not available in original RAMS Kuo scheme. Multiple choices of closure types for Grell scheme can be used.

2.1.3 Model Coupling

Many efforts have been made to couple land surface models and atmospheric models (Chan *et al.* 2004, Denning *et al.* 2003, Nicholls *et al.* 2004). The exchange of energy/momentum/tracer between them is the major issue of concern. While vegetation is

not stressed (that is, when there is adequate soil water content, moderate canopy space temperature, and adequate canopy space humidity), plants open their stomata and photosynthesize/transpire. This process allows the plants to absorb CO_2, a requirement for the creation of photosynthate; however, this process also allows water vapor to escape from the leaves. This moisture loss must be compensated in the plant through its drawing of soil water into the plant via the root system. Ball-Berry-Collatz Equation provides a link between photosynthesis and stomatal conductance, which makes it possible to parameterize CO_2 exchange together with water vapor exchange between vegetation and the atmosphere at the same time. Along with the other parameterizations (soil water movement and plant water consumption, solar radiation reflection or absorption, etc), the land surface can be simulated in a more realistic way than ever.

The Denning group of CSU and Freitas *et al.* of USP (University of São Paul, Brazil) have cooperated to couple BRAMS (adapted from RAMS 5.04) with SiB 2.5, effectively implementing realistic diurnal, synoptic, and seasonal exchanges of SH, water/LH, and CO_2 between the land surface model (SiB) and atmospheric model (BRAMS) have been implemented. Momentum flux near the surface is parameterized, and the methodology is described in Section 2.1.2.7 part d. Also BRAMS' surface shortwave albedo is replaced with SiB's surface albedo. Extensive tests have been made.

2.2 Data Preparation

2.2.1 Meteorological Data for RAMS Initialization and Boundary Nudging

NCEP (National Center for Environmental Prediction) Eta model reanalysis data for AWIP Grid 212, which has 26 pressure levels and grid spacing of about 40 km, is extracted and re-formatted for RAMS/ISAN input. AWIP Grid 212 is a 40-km Lambert Conformal grid extending from roughly 20 N to 60 N latitude, covering most of North America. The original dataset contains horizontal velocity, temperature, geopotential height, and specific humidity. I convert specific humidity to relative humidity in pre-processing program for compatibility with RAMS/ISAN. Eta model output stores horizontal wind components, u and v, relative to Lambert-Conformal map projection (Office Note 388, GRIB Documentation, 1998). New version of RAMS/ISAN package has a subroutine to rotate the wind automatically to another projection that we want. After the ISAN process is complete, the data are used as initial condition and boundary nudging weather data for the simulation.

2.2.2. Anthropogenic CO_2 Source
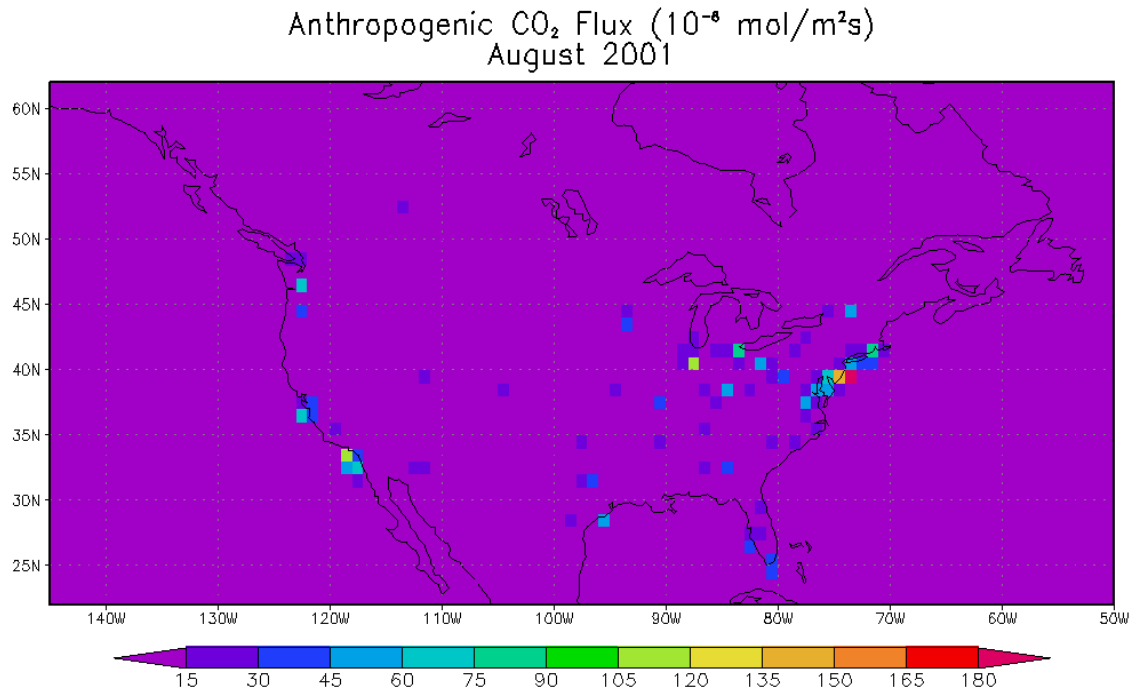
Figure 2.3: Map of anthropogenic CO_2 source. Adapted from Andres, 1996.

My anthropogenic CO_2 source from fossil fuel burning and cement manufacture is acquired from Carbon Dioxide Information Analysis Center (CDIAC) website and is created by Andres *et al.* (1996). Andres *et al.* used the fossil fuel consumption of every country and population density at every latitude and longitude degree to calculate CO_2 anthropogenic source strength for year 1995 (the latest available gridded dataset). The emission strength is scaled to 1.112 times for August 2001 based on the fossil fuel consumption record. Anthropogenic CO_2 then emits constantly on each grid point of the SiB-RAMS simulation domain at each time step. These emissions represent the non-negative CO_2 source from human being and its influence has proved to have a small impact on the CO_2 concentration field of my experiments.

2.2.3 Sea-Air CO$_2$ Flux
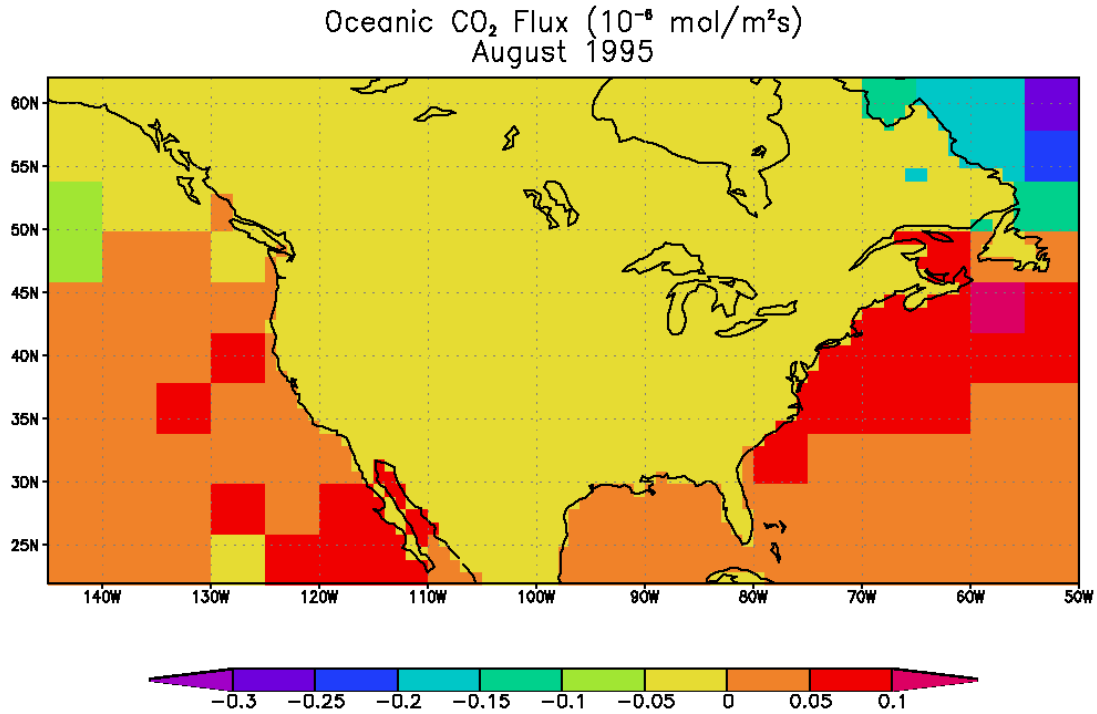
Figure 2.4: Map of sea-air CO$_2$ flux. Adapted from Takahashi, 2002.

The climatological spatial distributions of monthly net sea-air CO$_2$ flux is estimated for

the reference year of 1995 by Takahashi *et al.* (2002) based on more than one million

sea-air CO$_2$ partial pressure difference measurements and wind speed 10 m above the sea

surface. The original grid increment of this dataset is 5-degree by 4-degree and now re-

gridded (not interpolated) into 1 degree by 1 degree. Similar to anthropogenic CO$_2$ source,

the model emits/uptakes CO$_2$ at each time step constantly. Its influence has a significant

impact on the CO$_2$ concentration field of my experiments as well. Note that this sea-air

CO₂ flux is not scaled to August 2001 as for anthropogenic CO_2 source, because there is little information about its interannual variability.

2.2.4 Land Surface Parameters and NDVI
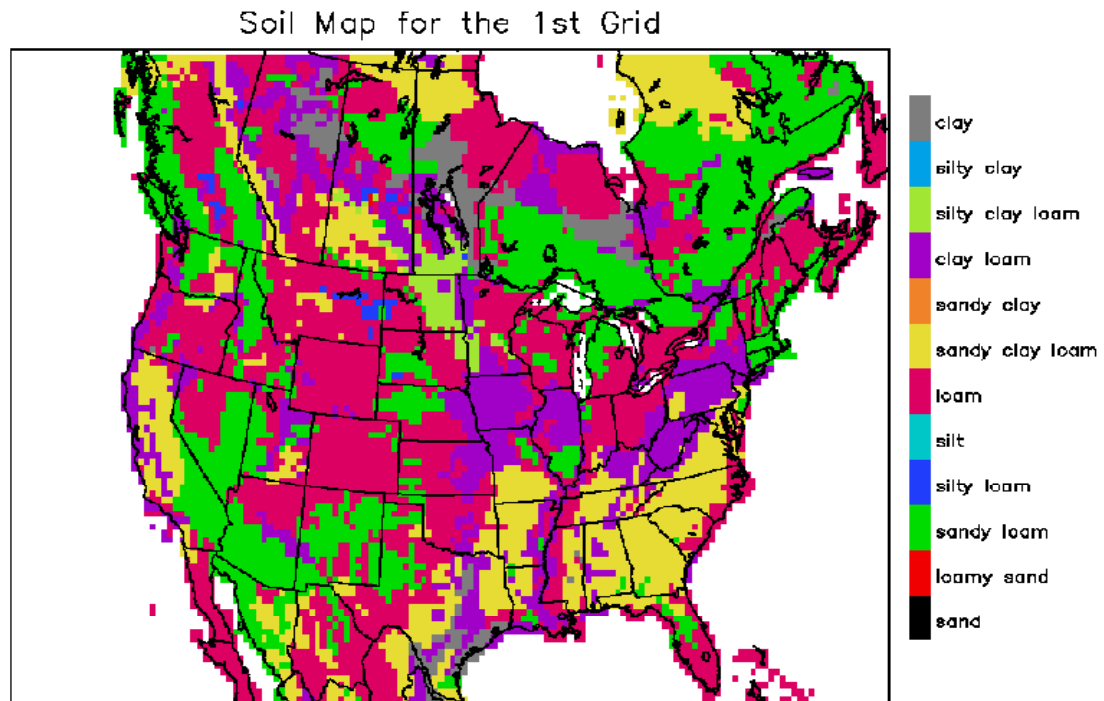
Figure 2.5: Soil map for the first grid. Adapted from IGBP soil type data.
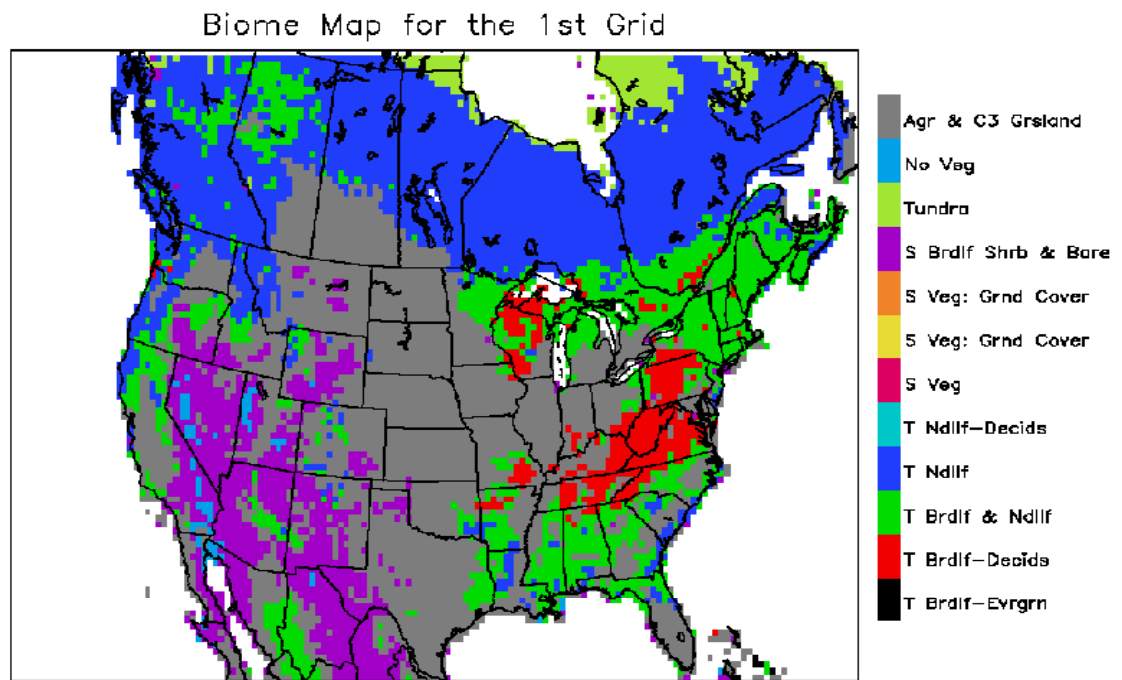
Figure 2.6: Biome map for the first grid. Adapted from satellite data product of U. of Maryland.

The soil map for SiB is a product of the International Geosphere-Biosphere Programme (IGBP), with resolution of 10 km. Soil types are converted from IGBP definition to SiB classes. The biome map is a satellite data product of the University of Maryland and had the resolution of 1 km. Biome types are also converted to SiB classes. Standard RAMS topography data from U.S. Geological Survey (USGS) is used and has 1-km resolution. Sea surface temperature is from the standard RAMS global monthly climatological data.
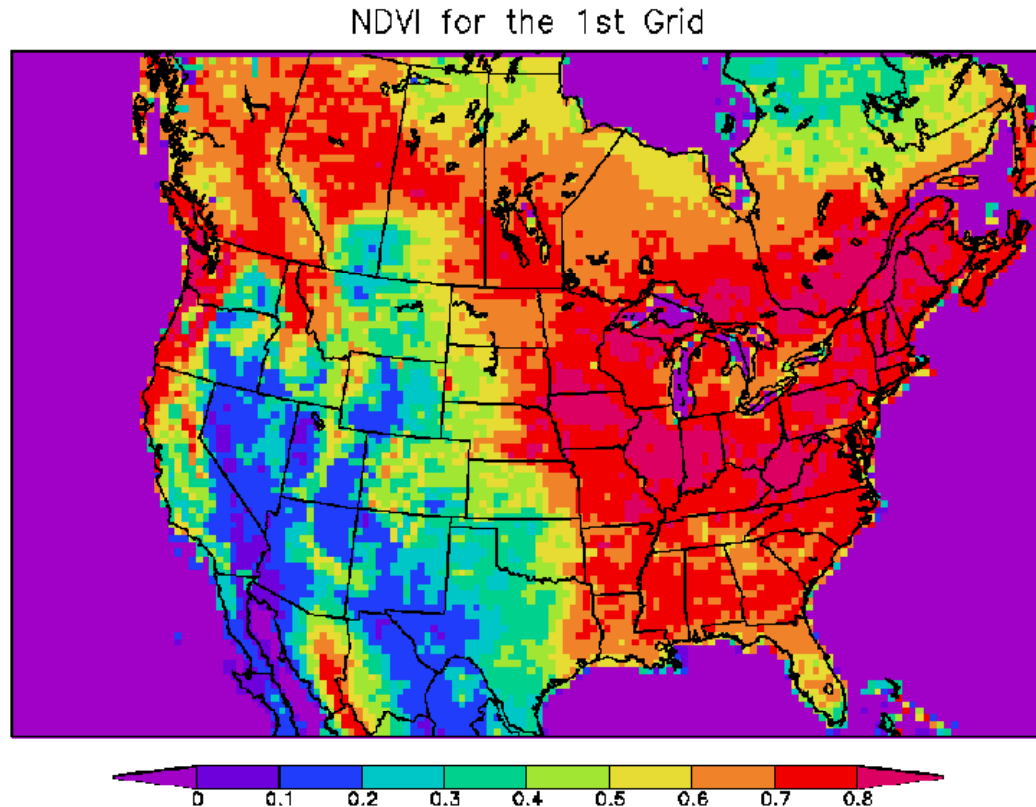
Figure 2.7: NDVI map for the first grid. Adapted from SPOT satellite data.

The Normalized Difference Vegetation Index (NDVI) is from the French satellite SPOT

(Systeme Probatoire d'Observation de la Terre) dataset with a resolution of 1 km. Surface

albedo, surface roughness, photosynthesis rate, and evaporation rate are primarily

determined by NDVI, according to Sellers *et al.* (1996), and NDVI is actually a measure

of the "greenness" of the land surface using the inherent absorptive and reflective

properties of vegetation. NDVI and knowledge about other surface properties, such

biome type and soil class, can be integrated to determine surface characteristics. In

essence, the greener the surface is, the more leaves there are. The more leaves there are,

the lower the albedo, the higher the surface roughness, and the stronger

photosynthesis/evaporation it is.

The SPOT NDVI data is a maximum value composite for the time period of 10 days (its

time resolution). Any points that are listed as "bad values" due to ice/snow or cloud are

filled by interpolation of the closest values in time in that pixel. Then the data are re-

projected into lat/lon coordinates. Finally, the biome map from University of Maryland is

used to "mask" NDVI values; basically, any pixel that is water in the biome map has to

be water in the NDVI map as well.

2.3 Model Configurations

2.3.1 Model Configurations and Input Data

Three grids are used in this research to achieve the goal of downscaling. Grid 2 and Grid

3 have the WLEF site at the center (see Section 2.4 for details). This nesting method

helps to scope synoptic, mesoscale, and small-scale phenomena at the same time. This is

especially valuable when both local surface CO_2 budget and horizontal CO_2 advection are

important to tower CO_2 observation during a frontal passage.
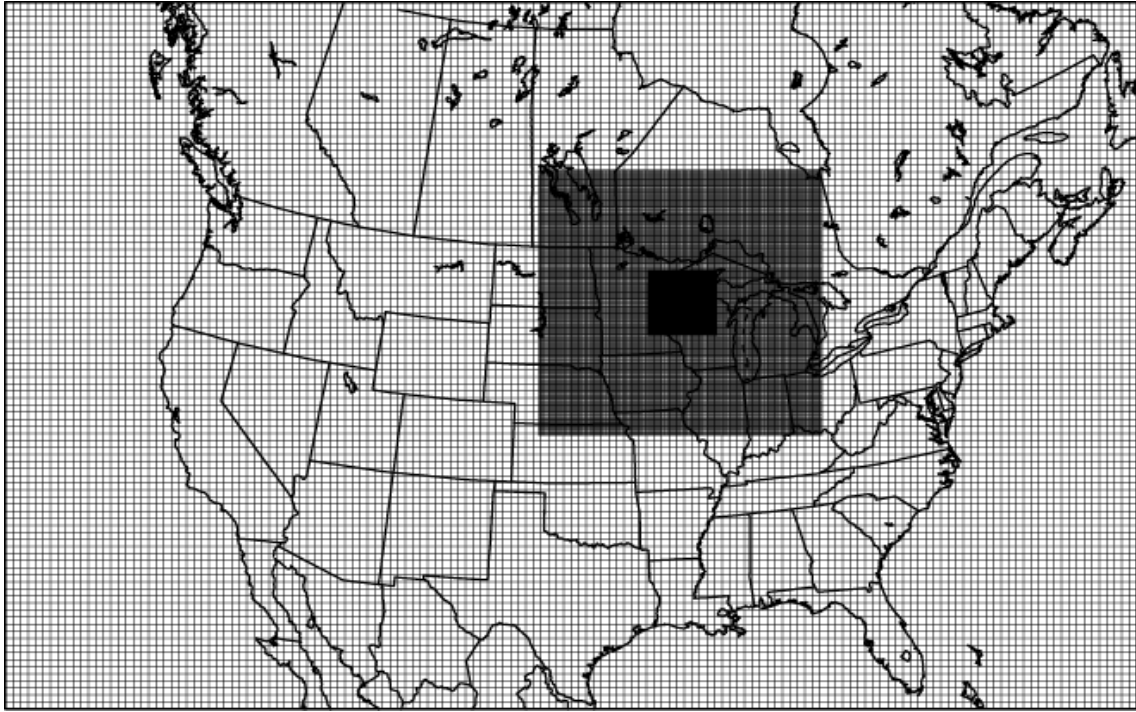
Figure 2.8: SiB-RAMS grids in this study.

Table 2.1

	1st Grid	2nd Grid	3rd Grid
Cell Numbers	150 x 100	150 x 150	182 x 182
Grid Spacing	40 km x 40 km	10 km x 10 km	2 km x 2 km
Timestep	60 s	30 s	10 s
Convection Scheme	Grell	Grell	Full Microphysics

Table 2.1 shows the basic grid configurations. As for vertical resolution, various grid

spacing is used, ranging from 60 m near the surface to 1000 m well into the stratosphere.

The possibility to use another finer grid inside the third has been explored. Several of the preliminary tests show that it is not suitable to compare the tower observation flux data, including NEEC and energy flux, with the model results of the grid point closest to the tower location in the fourth grid. The reason is because the tower flux observations represent the flux from the area of several square kilometers surrounding the tower. The "footprint" of the tower is always a few times larger than the area of any grid cell in the fourth grid of the test run. Because the signals inside the fourth grid have to aggregate before they are used in the comparisons and the signals from the third grid are more comparable even without aggregation, the idea to use the fourth grid is abandoned to save computer resources in the simulation.

The following shows other configurations used in this research.

- Simulation period – 00Z 2001/08/01 – 00Z 2001/08/21

- Projection – Polar stereographic projection

- Meteorological fields initialization – NCEP Eta 40 km Reanalysis Data

- First grid lateral boundary nudging

- Topographic data - RAMS standard USGS topography with silhouette average and topography wavelength smooth method

- RAMS standard sea surface temperature data

- SPOT NDVI, IGBP soil map, and U. of Maryland biome map

- Boundary condition - Klemp/Wilhelmson boundary condition for normal velocity

- Boundary condition - Zero gradient inflow and outflow boundary condition for variables other than normal velocity

- Harrington two-stream radiation parameterization

- Land surface model – SiB 2.5 with the land surface momentum flux parameterization adapted from Holtslag and Boville (1993) and Louis (1979)

- Mellor/Yamada eddy flux parameterization

- Microphysics parameterization

- Soil moisture from offline SiB spin-up output

- Gridded anthropogenic CO_2 source and sea-air CO_2 flux

2.3.2 Land Surface Initialization

2.3.2.1 Soil Moisture

Soil moisture is a variable to which one must pay close attention when simulating the land surface. It has been shown that not only do models require significant "spin-up" to achieve soil moisture levels in equilibrium with the climate, but also soil moisture has a strong impact on mesoscale weather phenomena (Pielke 2001). In addition, soil temperature and moisture of the top layer may have strong interaction with the atmosphere.

To overcome soil moisture problem, I spin up offline global SiB 2.5 using NCEP/NCAR reanalysis driver data from the year 1991 to the year 2001. After doing so, I insert the output into my SiB-RAMS grid points in the coupled model for every necessary surface variable, including soil water content fraction, soil temperature, canopy space

temperature, snow depth, canopy temperature etc. The model is "trained" for another 10 days (2001/08/01 – 2001/08/10) before the period of interest. The problem of small-scale features and heterogeneity will be discussed at the beginning of Chapter III.

2.3.2.2 Respiration Factor

As discussed in Section 2.1.1.5, SiB needs "respiration factor" to balance the carbon budget on an annual basis, which means that our biosphere in SiB 2.5 is designed to be non- source/sink by default. This kind of "constraint" is reasonable because the soil carbon pool changes over time very slowly. Therefore, originally when we run offline SiB driven by meteorological data, we must run it twice. The first run provides the amount of net assimilation aboveground. Then we calculate a respiration factor for each grid cell based on that net assimilation and use that respiration factor as input for the second run. In the second run, this respiration factor scales ground respiration so that it is equal to the net assimilation aboveground. This guarantees neutral CO_2 budget on an annual basis with a balance between aboveground net assimilation and ground respiration. Note that although SiB is necessarily balanced in the annual mean, it is designed to capture the diurnal and seasonal variability of photosynthesis and respiration during the year, allowing for realistic sources and sinks of CO_2 within the year.

Due to excessive computing resources required to run the SiB-RAMS simulation with my chosen grid-nesting regime for one full year to get the respiration factor, I instead run offline SiB 2.5 using NCEP/NCAR reanalysis driver data with the grid spacing of 1-

degree by 1-degree. I then use the offline SiB output to determine the respiration factor

for my SiB-RAMS simulation. For each grid cell of my SiB-RAMS run with the same

biome type as the offline SiB grid cell in which the SiB-RAMS grid cell resides, I assign

the SiB-RAMS grid cell the same respiration factor as the offline SiB grid cell. Otherwise,

I search the surrounding offline SiB grid cells nearby for the same biome type and use

that respiration factor instead. In a few cases for which the same biome type in or around

an offline SiB grid cell does not exist, I fill in a respiration factor equal to the

corresponding global biome-type average respiration factor. By doing so, the respiration

factor remains the same while the SiB-RAMS grid cell resides in the same climate zone

and in the same vegetation zone as the offline SiB grid cell.

For the first grid, the agreement on biome type between a SiB grid cell and any SiB-

RAMS grid cell residing in it or located nearby is 88.5%; for the second grid, the

agreement is 93%; for the third grid, it is down to 51.8%. The main reason for the low

biome type agreement within the third grid is that the biome is recorded as 70%

deciduous broadleaf and 30% needleleaf, which causes ambiguity when the model tries to

find the composite in between. It is not appropriate to go further for another nested grid

inside the third grid, since the agreement for a 1-km by 1-km grid might have only 45.5%

agreement on biome type with offline SiB. The high agreement on biome type between

offline SiB grid cells and SiB-RAMS grid cells ensures the validity of this research to

investigate local ecosystem response to the weather change.

2.3.2.3 Morphological Table

A morphological table is a table that provides some important physical properties of vegetation based on biome type. It includes inflection height for leaf area density, leaf width, leaf length, maximum LAI, etc., and most important of all, the 98th percentile of NDVI (ND98). ND98 is used to calibrate NDVI values because different satellite observation datasets might have slightly different NDVI values, even when simultaneously watching the same vegetation from their orbits. ND98 has to be re-calculated for each NDVI dataset (eg. SPOT, GIMMS, etc.). In our case, we calculate the 98th percent NDVI value for each biome type based one year of 1-km SPOT NDVI data. The ND98 value is most important not only because it is used for calibration but also because it is used to determine FPAR, an important control on photosynthesis.

2.4 Case Description

I have made my simulation to surround the 447-meter tall WLEF TV tower, located in the Chequamegon National Forest, 14 km east of Park Falls, Wisconsin. The tower has equipment to measure meteorological constituents (such as wind and temperature) and CO_2 concentration at 11, 30, 76, 122, 244, and 396 m, and equipment to measure their fluxes at 30, 122, 396 m. The CO_2 data are available every 12 minutes, and the frequency of measurements of temperature, water vapor mixing ratio, and wind speed and direction is 5 Hz (Davis *et al.* 2003). This site is chosen because measurements made from the mid-boundary layer reflect the influence of a large heterogeneous area.
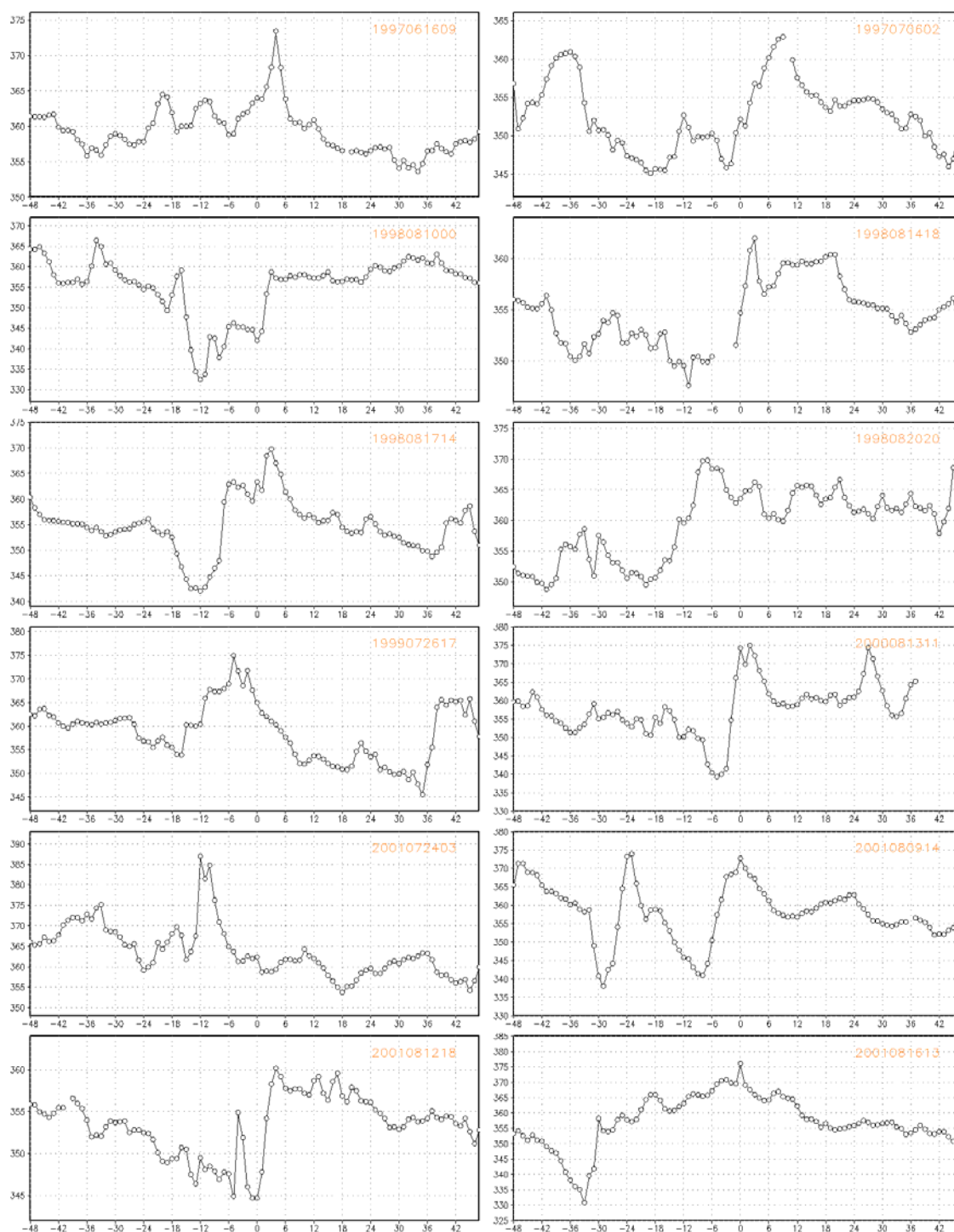
Figure 2.9: CO_2 mixing ratio at 396 m of the WLEF tower during 12 frontal cases.

In the months of June, July, and August 1997 – 2001, I identify from surface analysis

weather maps 51 cold fronts passing the WLEF tower site. Most of them occurred in

August. I double-identify the fronts using the tower data when wind direction shifts from

southwest to northwest for all the three equipped levels (30 m, 122 m, and 396 m), at

which wind direction is measured. Due to the fragmented data and ambiguous signals, I

can only identify 14 fronts from WLEF-observed wind direction shifts out of those 51

cases using my front-arriving definition. And only 12 out of the 14 have [CO_2] data at

396 m around the time when the fronts arrived.

Figure 2.9 shows the CO_2 mixing ratio during the 12 frontal passages. The x axis is the

hour relative to the front-arriving hour (when the wind direction shifts from southwest to

northwest for 30 m, 122 m, and 396 m). -1 means one hour before front-arriving hour, 2

means 2 hour after and so on. The number at the upper right corner of each panel is the

frontal-arriving time. For example, "1997061609" means that a cold front arrived at the

WLEF tower at 09Z 1997/06/16. It is quite obvious that the CO_2 concentration has strong

variations during frontal passages, and the CO_2 concentrations often have spikes that are

associated with the fronts' timing.

Each front has its own structure and concomitant weather condition. Therefore, we have

to consider each case separately to see what it can tell us. In this research, I shall present

a case in which CO_2 enrichment occurs during a frontal passage. I have chosen a summer

cold front case in which [CO_2] is rising during the frontal passage. A cold front arrived at

the Wisconsin WLEF TV tower at 7 AM local standard time (LST), August 16th, 2001

(13Z 2001/08/16). I have chosen this case because the data available during this time

period had relatively few gaps, and the event happened in the morning, the time for

convective boundary layer build-up. After assessing some possibilities, we developed

three hypotheses to explain [CO_2] rising when a front passes the tower:

Hypothesis 1: Ecosystem Response

> The ecosystem may have some response to the change of the weather, altering the
>
> [CO_2]. The weather ahead of a cold front is usually warm (or even hot) and humid,
>
> while the weather behind a cold front is cool (or even cold) and dry. Air
>
> temperature and humidity may influence the photosynthesis and/or respiration
>
> rate to some significant degree. Also, the weather near the frontal zone is often
>
> cloudy. As the clouds block sunlight, it may slow down photosynthesis,
>
> depending on how much diffusive solar radiation the plants can obtain. While
>
> ground respiration of the ecosystem does not change as quickly due to moister
>
> soil (the result of precipitation and less shortwave radiation with the passing of a
>
> front), this can lead to accumulation of CO_2 in the boundary layer.

Hypothesis 2: Horizontal Advection

> Generally, before a cold front passes, wind blows from the southwest. After the
>
> front passes, the wind blows from the northeast. The difference of [CO_2] between
>
> the southeast air mass and the northeast air mass may be able to explain the [CO_2]
>
> change measured at the tower.

Hypothesis 3: Vertical Mixing

> When a front passes the tower, there is usually strong vertical convection. Since
>
> the boundary layer has relatively low [CO_2] compared to the free atmosphere

during summer, vertical mixing may bring down air of relative high [CO_2] from

upper level into the boundary layer. Therefore, the [CO_2] rises in the boundary

layer air being measured by the tower instruments.

Figure 2.10 show the surface analysis with 500 hPa geopotential height contour for 12Z

2001/08/16, the approximate time of the frontal passage that I am studying and
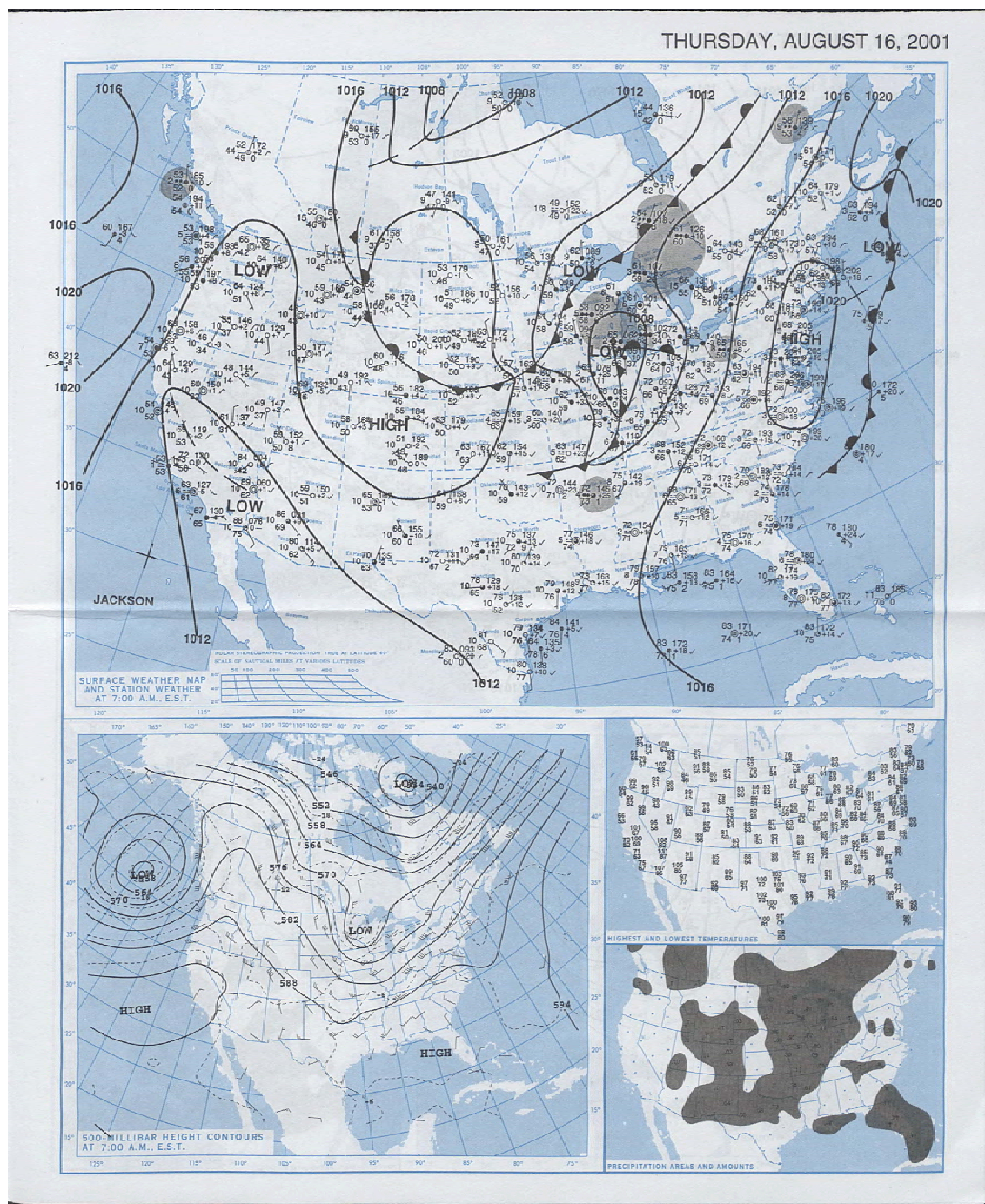
simulating.

Figure 2.10: North America surface analysis, 500 hPa height contours, highest and lowest temperatures, and precipitation maps at 12Z August 16th, 2001. From NOAA Central Library, U.S. Daily Weather Maps Project.

A low-pressure system formed in the southwest part of Ontario, Canada on 8/15 and
moved southeast to Lake Superior on the 8/16. The wind blew from the northwest at the
WLEF tower when the cold front was established from the center of the low, stretched to
southwest, and extended to Nebraska. At 10Z, 8/16, the WLEF site reported a wind
direction change at 396 m from southwest to northwest, while at 02Z 8/17 it reported
0.76 mm of rainfall. Air temperature and pressure did not deviate significantly from the
average diurnal cycle, but relative humidity dropped sharply after the rain. Radar detected
potential rain clouds (not shown) after the wind direction shifted. There happened to be
another low pressure system to the south. The low came out from the east side of the
Rocky Mountains on 8/14 and moved to the west bank of Lake Michigan on 8/16.

Figure 2.11 shows $[CO_2]$ at different levels around the time of frontal passage. We can
see that $[CO_2]$ started to increase slowly from the morning of 8/15. If we define the time
of wind direction shift as front-arrival time, $[CO_2]$ began to decrease within a couple of
hours of the frontal arrival, depending on level height. More interestingly, $[CO_2]$
variation became larger after that.
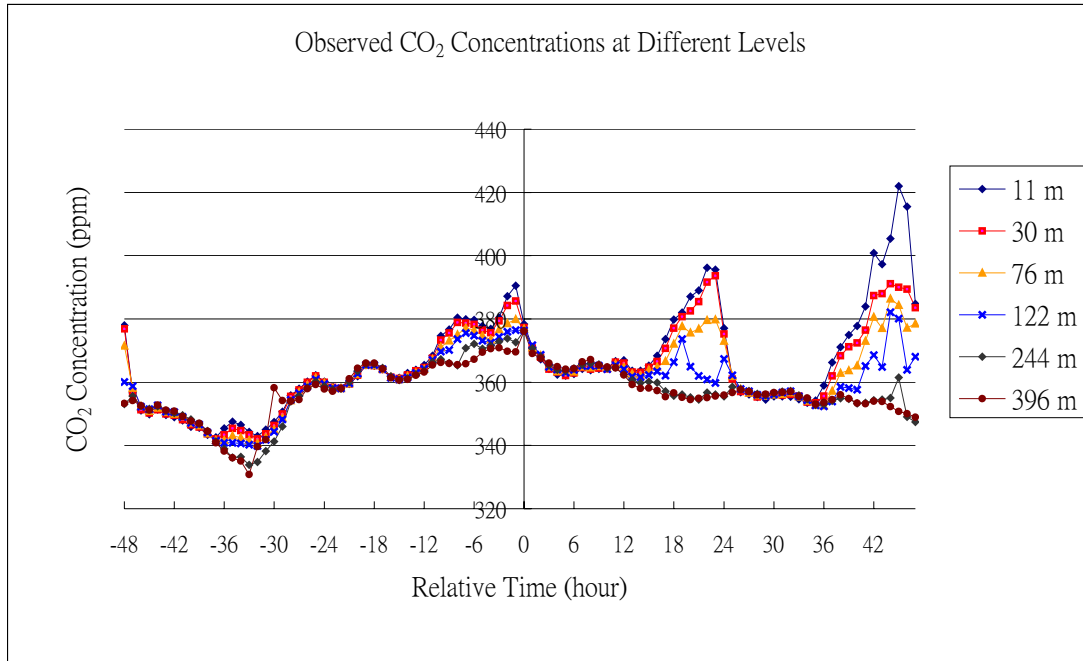
Figure 2.11: CO_2 concentrations during the period of 96 hours around front arrival hour of the case (13Z 2001/08/16).

Another reason why this case was chosen is because the CO_2 concentration rose more than 40 ppm at almost all the levels within 30 hours before the front arrived. The 40ppm rising alone is more than twice the seasonal variation of the observed by flasks in the North Pole, about five times of it in Hawaii, more than 20 times of it in the South Pacific Ocean, and about 40 times of it in the South Pole. Apparently inland CO_2 concentration varies much larger than the seashore or sea surface, and the CO_2 variability in the North Hemisphere is strongly influenced by the land biophysical processes. The front arrived in the early morning, and the effect of CBL build-up (local scale) and the pressure systems (synoptic scale) make this case interesting. The response of ecosystem to the weather is also one of the most important concerns in the thesis.

Chapter III   Result

This chapter focuses on the results of data analysis and model simulation. As mentioned in Chapter II, WLEF tower gathers the data at one single geographical point. CO_2 pulses, either from the ecosystem or from somewhere else delivered by any kinds of transport, are considered as "signals" in this research. The signals carry the unique characteristics from their sources/sinks, such as different carbon isotope ratio and different concentrations. Measurements at several different levels make it possible to detect the signal in vertical direction. In order to get horizontal signals, however, a tower network or model simulation is necessary.

Section 3.1 will talk about offline SiB 2.5 spin-up model results, which in turn feed in online SiB-RAMS simulation as initial conditions; Section 3.2 will compare model meteorological results with observations during the period of interest (00Z 2001/08/11 – 00Z 2001/08/21); Section 3.3 will compare model CO_2 concentration and flux with the observations; the last section, Section 3.4, will attempt to find out the reason for CO_2 rising before the frontal passage and CO_2 decrease after that at the WLEF tower, using both the results from tower data analysis and model simulation.

3.1 Pre-run

3.1.1 Offline SiB 2.5 Spin-up

Avissar and Liu (1996) argued that mesoscale landscape spatial heterogeneity might trigger formation of mesoscale circulation and affect the precipitation regime. Soil moisture is also one of the most important variables in SiB 2.5 that determines photosynthesis and respiration rate. Therefore, it is necessary to find out the best solution for soil moisture initialization.

As a first step to running SiB-RAMS for the period between 2001/08/01 and 2001/08/21 with our case happening on 2001/08/16, we must first "spin up" or run SiB for several years offline (separately from RAMS), forced by weather reanalysis data, in order to allow slowly evolving fields, such as soil moisture, to equilibrate to realistic values for August 2001. Offline SiB 2.5, driven by NCEP/NCAR weather reanalysis data, needs at least several years to equilibrate soil moisture of the deep layers, while all other surface variables can be equilibrated in a few days by the weather. I spun up offline SiB 2.5 for the period between January 1991 and August 2001 (hereafter SPNP). SPNP has a spatial grid spacing 1-degree latitude by 1-degree longitude, which is consistent with its driver data. However, for my simulation in SiB-RAMS, the first grid has grid spacing 40 km by 40 km, while the second has 10 km by 10 km, and so on (see Chapter II). Therefore, several grid cells in my first grid of SiB-RAMS simulation consist of one grid cell in SPNP. The soil water content (SWC), in unit of volume fraction, in SiB-RAMS is assigned according to offline SiB 2.5 spin-up result, when the SiB-RAMS grid cell resides on the offline SiB 2.5 grid cell.

Soil Water Content of the 1st Layer (volume fraction)
1st Grid, 00Z 2001/08/01

Soil Water Content of the 2nd Layer (volume fraction)
1st Grid, 00Z 2001/08/01
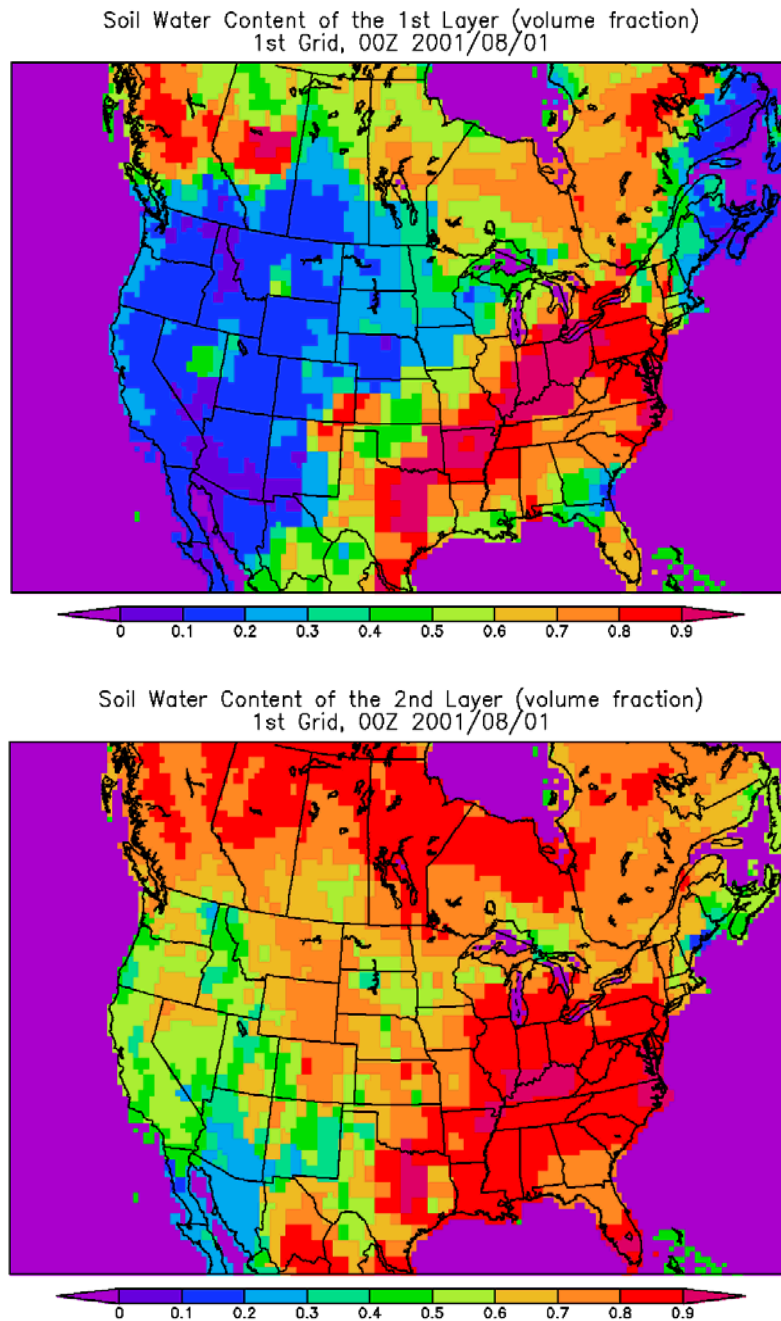
Figure 3.1: Soil water content of the first grid after ten years offline spin-up.

Figure 3.1 shows the resultant soil water content (SWC) of SPNP, which is at the first

hour of August 2001. The upper panel is for the first layer (surface layer, 0 – 2 cm), while

the lower panel is for the second layer (root zone, 2 – 90 cm or deeper, depends on biome

type). The unit is "volume fraction", which indicates the amount of water in the soil as a

percent of available pore space. The SWC of the first layer is very sensitive to the

weather and varies based on precipitation and energy balance in the time scale of days.

Note that SWC is also determined by soil type. The higher the percentage of clay in the

soil, versus sand and silt, the more porosity the soil has. This means that when two

different types of soil contain the same amount of water in a fixed volume, the one with

the higher percentage of clay has the lesser volume fraction of water. Therefore, both

precipitation and soil type determine soil water content in the unit of volume fraction. In

the upper panel, we can see that middle to lower Mississippi Basin and northern Texas

have very high soil water content in the first soil layer. That is because in spring the

precipitation zone is located there. Also, wet soil in the southwest corner of Canada

reflects the fact that it is a humid temperate zone. The lower panel shows that a high

water content zone exists in the eastern part of the U.S. and to the west of Hudson Bay of

Canada. This is a result of high precipitation climate in those two areas.

3.1.2   Model Training

Although using offline SiB to initialize the SWC for the SiB-RAMS run is quick and

convenient, one drawback is a lack of heterogeneity at the finer scales. Obviously we

cannot keep it for the inner grids. The SWC of the first layer (0 – 2 cm) is quite sensitive

to the recent weather (a few days), and the model "training" is done for at least 10 days

(8/1 – 8/10) before the period of our interest (8/11 – 8/21) with the frontal event on 8/16.

Therefore, this heterogeneity problem should be unnoticeable for the first layer, especially for the first layer of the first grid, which has grid spacing close enough to offline SiB.

The other drawback of using the offline SiB SWC output for soil moisture initialization is the incorrect reproduction of energy budget at least for the first few days. The outgoing energy is partitioned into LH, SH, and outgoing radiation. Apparently, if the SWC initialization cannot represent very well in the finer scales, it would influence LH flux and in turn the partition of outgoing energy. The solution to this problem is left here as a future work.
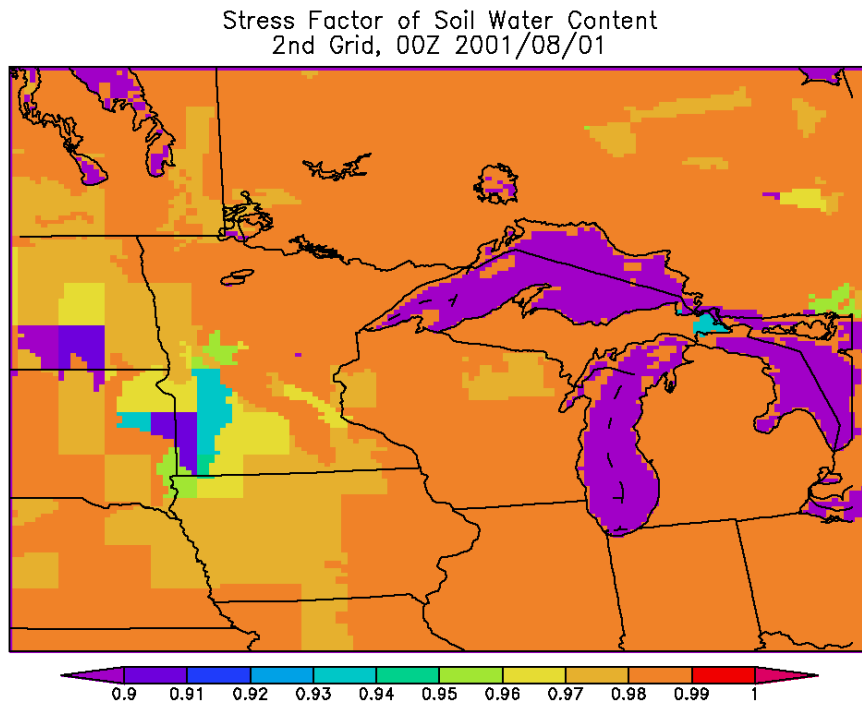
Figure 3.2: Stress factor of soil water content of the second layer after ten years offline spin-up.

Figure 3.2 assists in explaining the use of SWC of the second layer from the offline SiB result. It shows the "stress factor" of SWC in SiB. The stress factor in SiB is used to regulate the photosynthesis, and it has the value of 1 to represent no stress situation and the value of 0 to represent full stress. This stress factor only depends on the SWC of the second layer. When the soil dries out, the photosynthesis rate is lessened by the ratio of the stress factor. Figure 3.2 shows that the stress factor of the SWC in the second layer is essentially not going to influence photosynthesis and respiration within the inner grids. For the first grid, the problem is even smaller, because the grid spacing of the first grid is 40 km, which gets reasonable heterogeneity from the 1-degree by 1-degree offline SiB spin-up, and the stress factor for the first grid is always higher than 0.9 as well.

On the other hand, respiration is also a function of the SWC of the second layer. As the soil moisture increases to an optimal value, the respiration rate reaches its maximum. The influence in this manner is much smaller than the soil temperature and usually negligible.

Model training is required in addition to the offline spin-up for at least a few days before the period of interest, because there is always some internal inconsistency between the initial condition and model behavior. For example, SiB-RAMS is initialized with Eta reanalysis data, which has significantly different topography, parameterizations, and even numerical methods than SiB-RAMS. SiB-RAMS "pulls" its solution (integration over time) from the model initial condition to meet the internal characteristics of SiB-RAMS. Also, model training provides better representation and heterogeneity of soil moisture and other SiB variables.

3.2 Meteorological Parameters Comparison

North America crosses five different time zones. Therefore, for convenience, Greenwich time will be used for the rest of this chapter. Greenwich time is 6 hours ahead of the local standard time (LST) in Wisconsin. This means, when the time denotes 12Z in the plots, it represents 0600 LST in Wisconsin, which is early in the morning. Likewise, 18Z is actually noon for the central U.S.

The model meteorological results are compared with the weather maps and tower observations in this section. The comparisons of most of the traditional meteorological parameters, such as pressure, wind field, temperature, water vapor mixing ratio, and energy fluxes will be shown for the period between 00Z 8/11 and 00Z 8/21. The observations have some discontinuities due to equipment failure and the interruption of wild animals.

3.2.1 Model vs. Analysis

Figure 3.3: Model sea level pressure and lowest level wind vector.

Figure 3.3a shows the sea level pressure and lowest level wind vector of model output at

12Z 8/16, one hour before the cold front arrived at the WLEF tower in the real world.

Our frontal case that stretched through Wisconsin and Iowa (the brown dash line) does

not show up in the figure. It passes WLEF and vanishes about eight hours earlier in the

model (not shown), and the northerly winds take over. In the real world, the front was

quite weak as well and disappeared soon. The low-pressure center in the model is located

near the eastern border of Indiana instead of Illinois on the surface weather map (Figure

2.10). On the consecutive surface analysis weather maps (not shown here), the low-

pressure center originated from the east side of Rocky Mountains, and then moved from

Kansas and Nebraska to Wisconsin and Illinois in 24 hours, while the model output

animation (not shown here) shows that the center moves from a close originating spot to

the eastern border of Indiana.
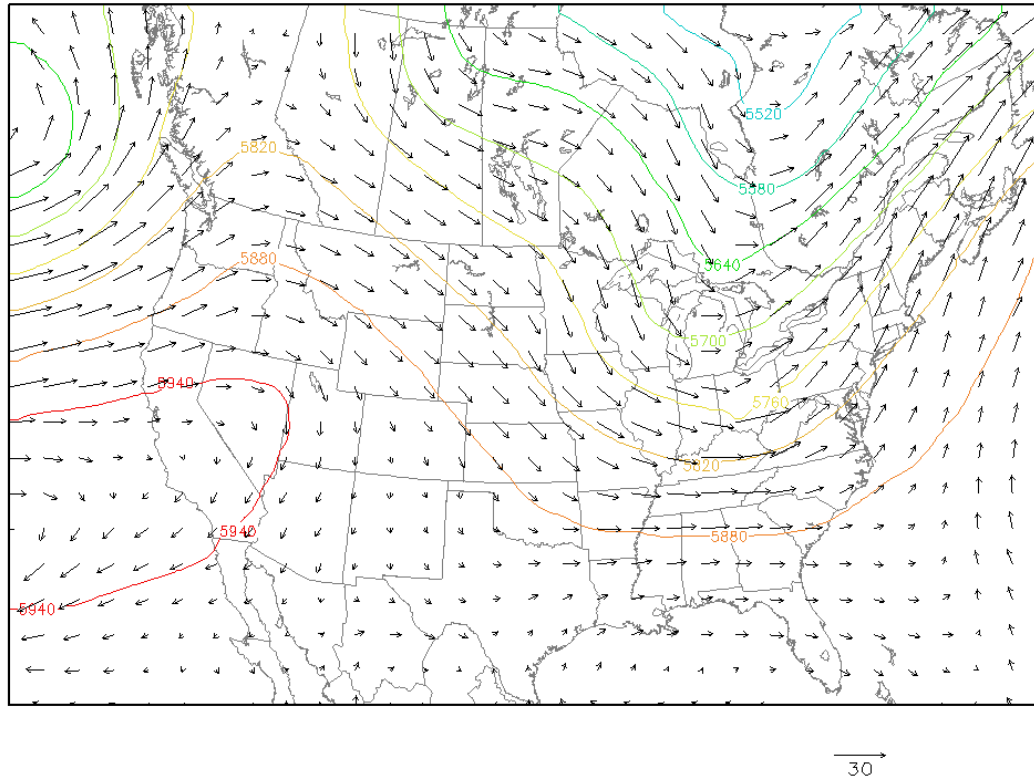
Figure 3.4: Model geopotential height and wind vector for 500-hPa pressure level.

Figure 3.4 shows the 500-hPa geopotential height and wind vector. The result is a very

good match with the analysis map (Figure 2.10), except for the low lope to the southwest

of Lake Superior not showing in the model.

3.2.2 Model vs. Tower Observation

I use the datasets from two different tower observations to compare with the model results. One is from WLEF and the other is from ARM (Atmospheric Radiation Measurement) Program, Oklahoma.

The information about the WLEF site can be found in Chapter II, the case description section. The Southern Great Plains ARM site is located in Lamont, Oklahoma. Its coordinate is Latitude: 36° 36' 18" N, Longitude: 97° 29' 6" W. As at the WLEF tower, the ARM site includes a flux tower to measure CO_2, LH, and SH fluxes continuously (Sheridan *et al.* 2001). The vegetation is crop around the ARM tower.

A. WLEF

For the following several figures, the black line indicates the model output, while the green line indicates the observations, unless otherwise noted. These single-point comparisons are done between the closest model grid point to the WLEF site in the third grid (the finest grid) and the observations.
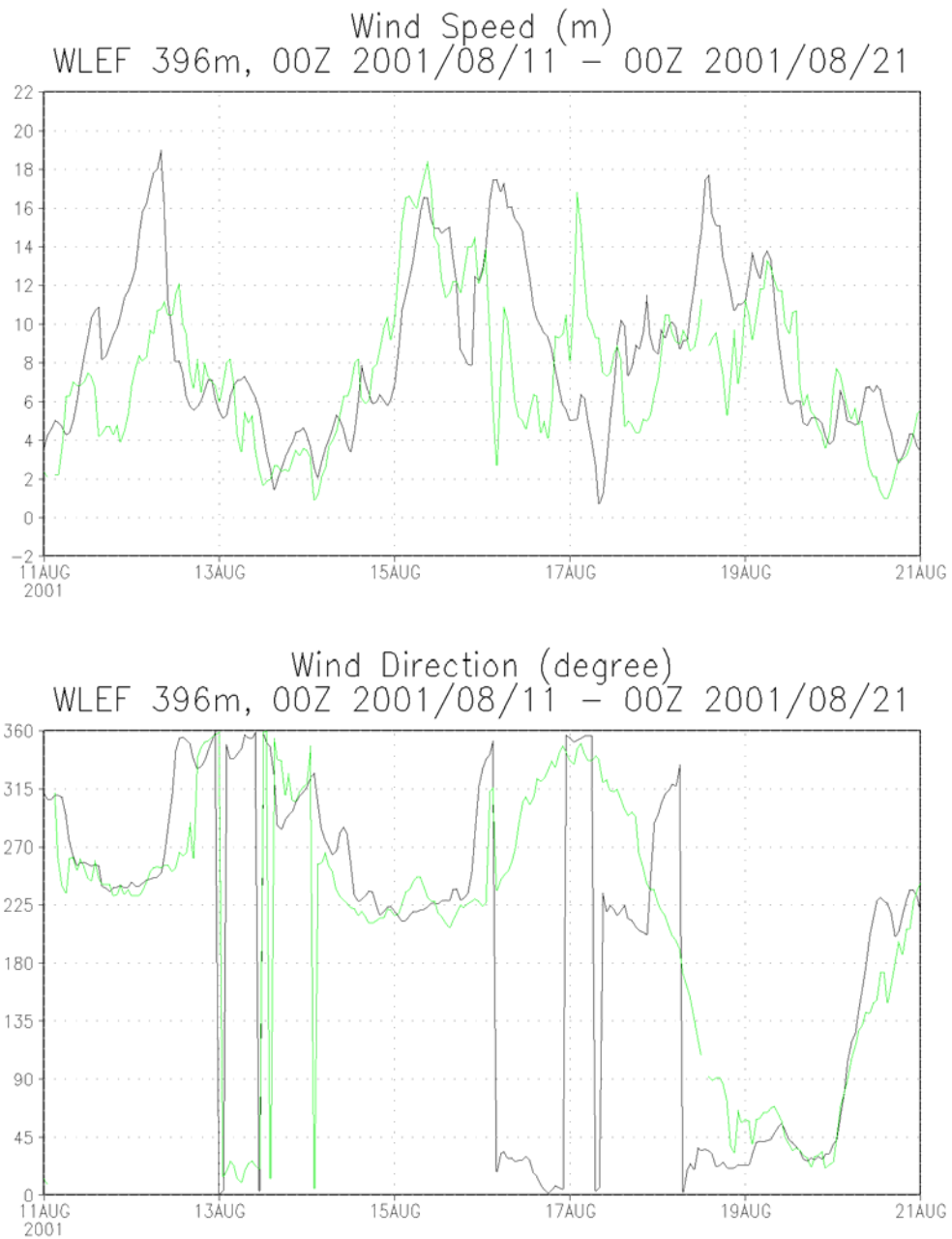
Figure 3.5: Wind speed and wind direction comparison.

Figure 3.5 shows the comparison of wind speed and wind direction between the model

output and WLEF observation at 396 m. The upper panel shows that overall the model

wind speed matches the tower observation quite well. However, the speed spike on 8/17

in the data happens on 8/16 in the model, and the spike on 8/12 is overestimated in the model.

The lower panel shows that the simulated wind direction also matches the observations well generally, but there are mismatches on 8/16 and 8/17. While the observations show the wind direction changing from northwest to north and back to northwest on late 8/16 and early 8/17, the simulation shows wind direction changing from northeast to north and southwest. The green line (tower data) shows that the wind direction changes from southwest to northwest twice on 8/15 and 8/16, while the black line has just one and happens a few hours earlier.

The mismatch of wind direction actually tampers with the reproduction of $[CO_2]$ mixing ratio at 396 m of the WLEF tower. It will be shown later that the southerly wind brings the high-concentration air to the northern Wisconsin on 8/15 in the model and makes CO_2 concentration reach its maximum. This is at least half day earlier in the model than in the real world.
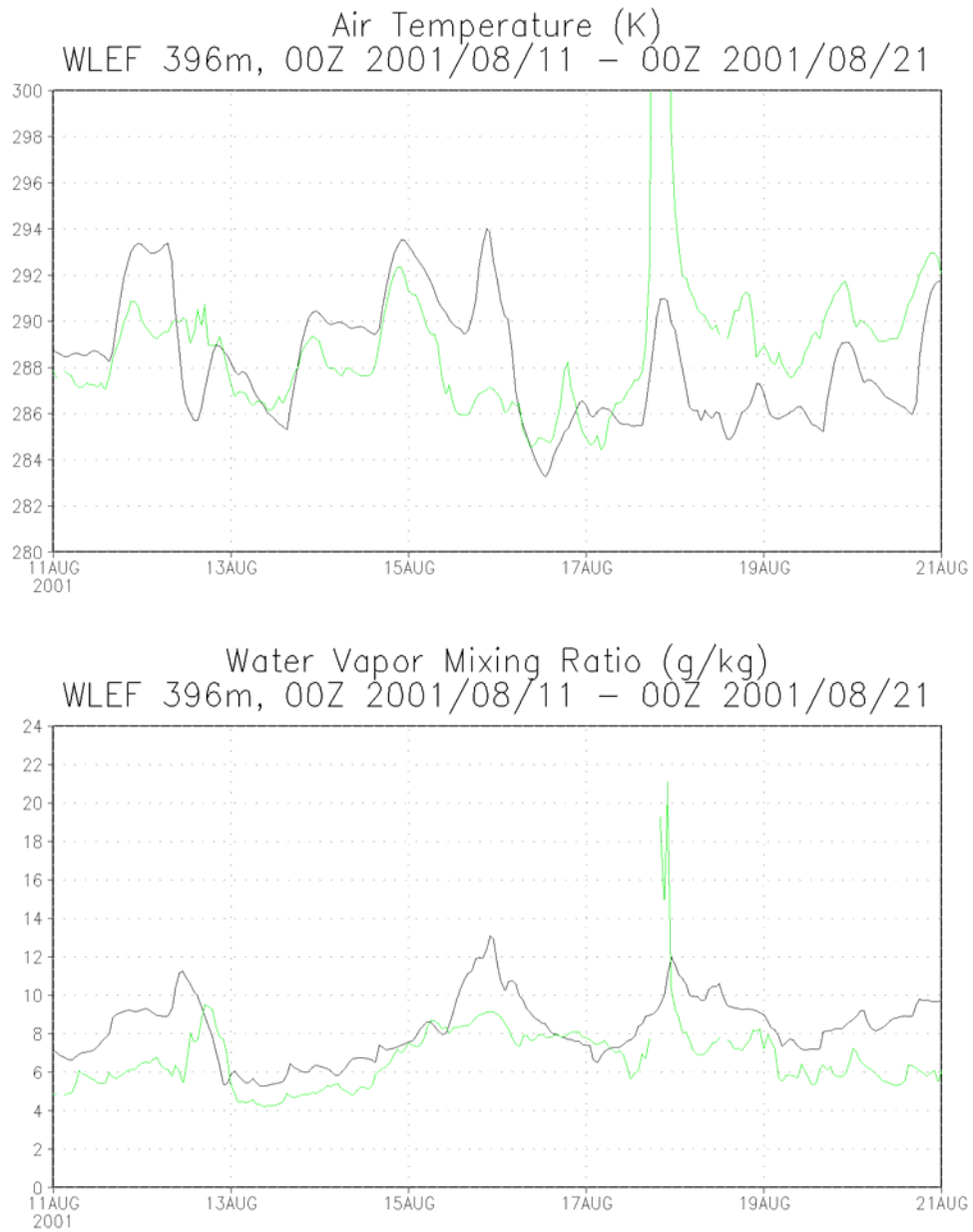
Figure 3.6a: Air temperature and water vapor mixing ratio comparison for 396-m
level.

Figure 3.6a shows the comparisons of temperature and water vapor mixing ratio at 396 m

above the surface. We can see that the observed temperature on 8/17 afternoon is

spuriously high and the observed mixing ratio line is broken following an extremely high

value persistent for a few hours. The discrepancy between the model temperature and the

observed temperature is not very large otherwise. However, on 8/15 and 8/16, the

temperature is overestimated, which might influence other parameters during the frontal

passage. After that spurious spike, the model tends to underestimate air temperature with

a relative stable difference.

On the other hand, the water vapor mixing ratio from the model is very consistent with

the observations, although the model overestimates in the beginning and the end of the

period of interest. In general, the model captures the patterns of rising and falling mixing

ratio quite well, even during these periods of overestimation.
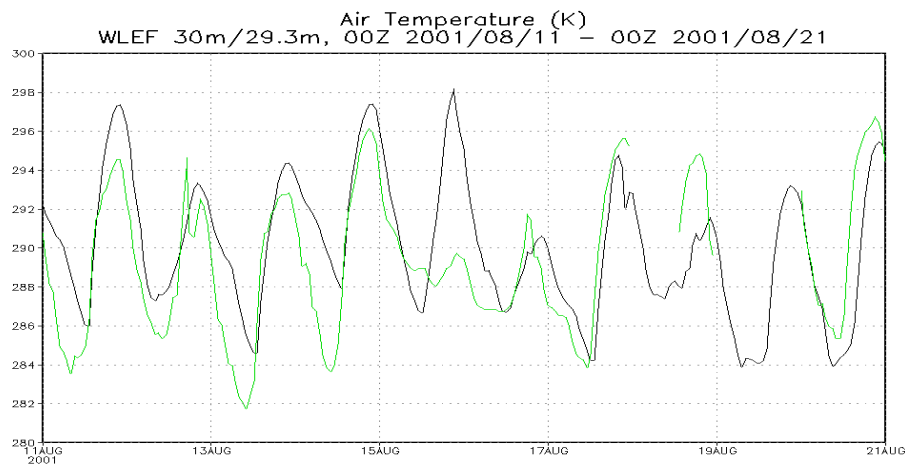
Figure 3.6b: Air temperature comparison for 30-m level.

Figure 3.6b shows the comparison of air temperature at 30 m. The model output and the

observations match quite well except for the daytime of 8/15, which is supposed to be a

cool and cloudy day. The observed temperature started rising from 8/12 to 8/14 and

suddenly dropped during the daytime of 8/15. Temperature variation is smaller on 8/15
and 8/16, probably related to the full-sky cloud cover at that time (will be discussed again
later in this section). The nighttime temperature on 8/15 is higher than usual, and it might
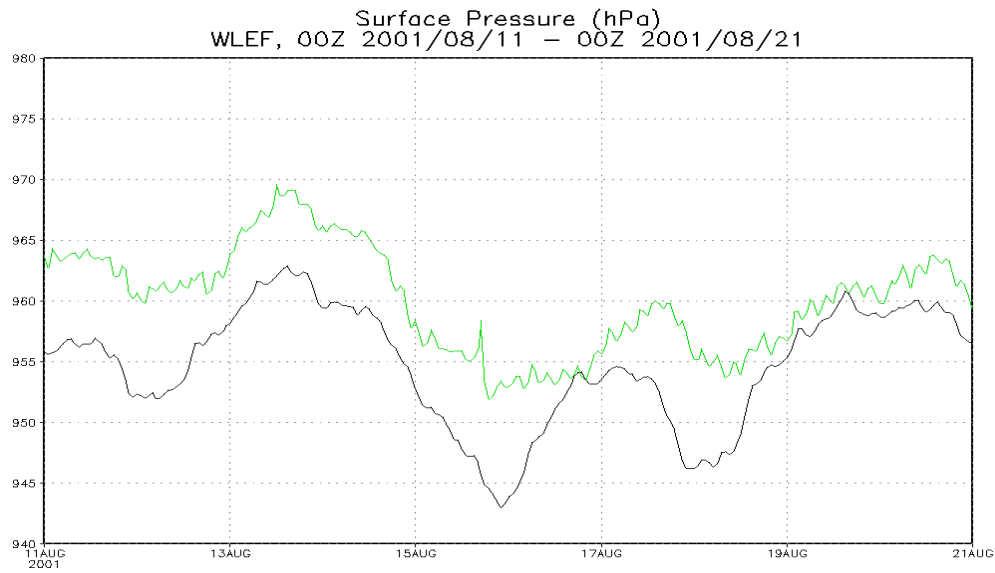enhance respiration.

Figure 3.7: Surface pressure comparison.

Figure 3.7 shows the model pressure at the lowest level, 29.3 m, compared to WLEF
observed surface pressure. In general the surface pressure is a good match between the
model output and observation. In particular, the model simulates quite well the falling
pressures beginning on the 13th and continuing through the 15th. This provides strong
evidence that the model simulates the synoptic event. Note that there is a persistent gap of
about 7 hPa existing. This is likely due in part to the altitude difference (29.3 m vs. the
surface), and in part to the model's systematic underestimation of pressure.

The rising trend on 8/16 in the model is too strong compared to the observation, and the

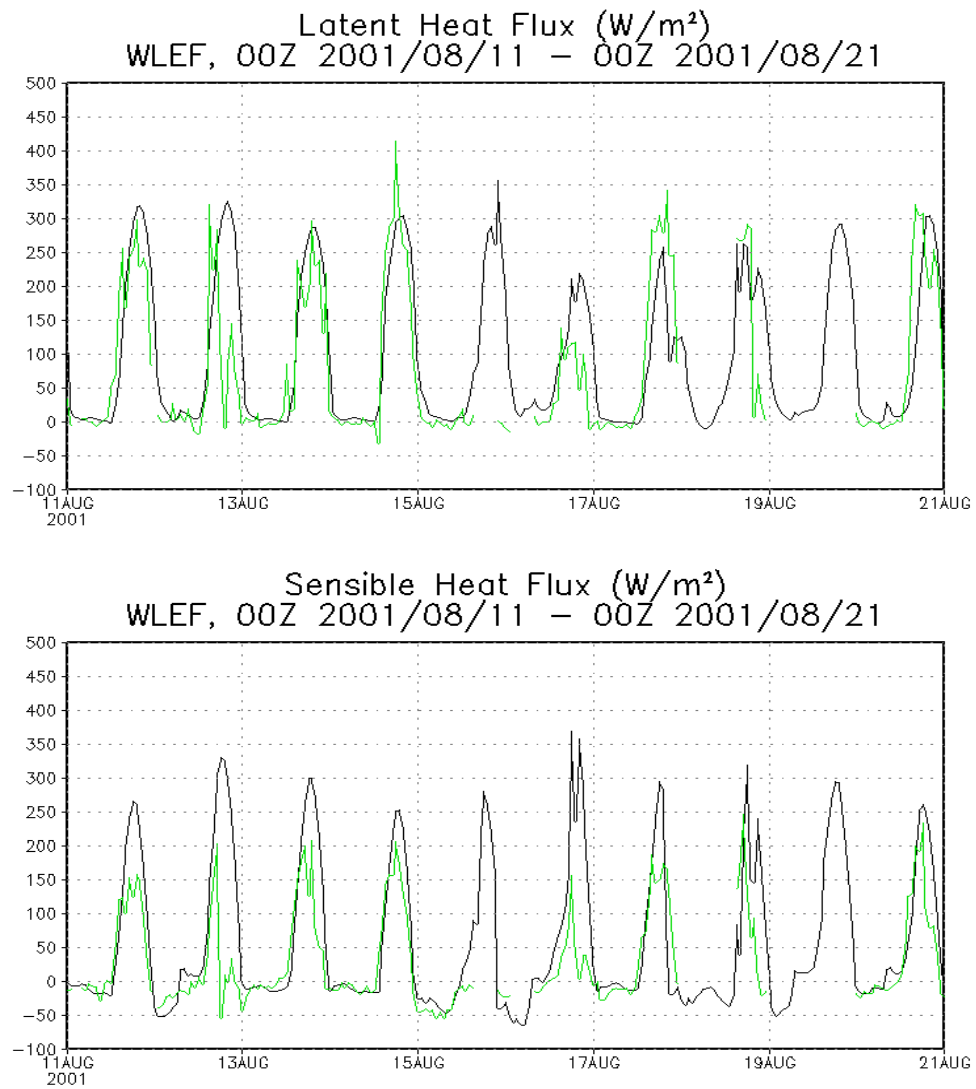maximum value on 8/17 is simulated 12 hours earlier.

Figure 3.8: Latent heat and sensible heat flux comparison.

Figure 3.8 shows that the model LH flux matches observations very well except for 8/13

and 8/16. The model consistently overestimates the SH flux during the daytime. On 8/16,

both of the LH and SH fluxes are overestimated. It will be shown later that both on 8/15

and 8/16, the sky at the WLEF site was overcast. The model did not successfully simulate

the incoming radiation on these two days, and therefore it tended to overestimate the

outgoing energy. Consistent overestimation of SH flux is believed due to the drawback of

the "one-leaf" assumption of SiB, and is being addressed by Baker (personal

communication).
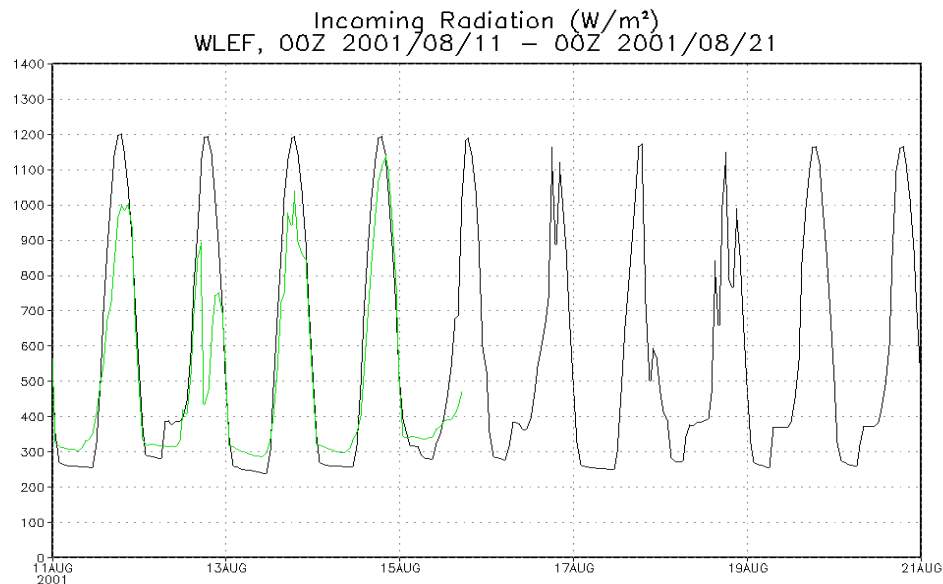
Figure 3.9: Incoming radiation comparison.

Incoming radiation, including downward shortwave radiation and downward longwave

radiation, is shown in Figure 3.9. After 8/15 the data are missing. The radiation in the

model does not vary enough from day to day as in the real world. We can see that

incoming radiation is overestimated on 8/11, 8/12, and 8/13 during the daytime.

Incoming radiation is influenced by clouds. For the first and second grids in the model,

the formation of clouds is determined by relative humidity and the radiation scheme

(Harrington scheme in this research); while for the third grid, the formation of clouds is

resolved. The clouds in turn determine how much radiation comes through the

atmosphere and reaches the surface. Apparently, the model does not do well on 8/12.

Net radiation from the WLEF observation is not comparable with the model, because the

site has the grass clearing ground, whose data cannot compare with the model that has

deciduous broadleaf trees surrounding the tower.

B. ARM

For the following several figures, the black line still indicates the model output, while the

green line indicates the observations. These single-point comparisons are done between

the closest model grid point to the ARM site in the first grid (the only grid that covers
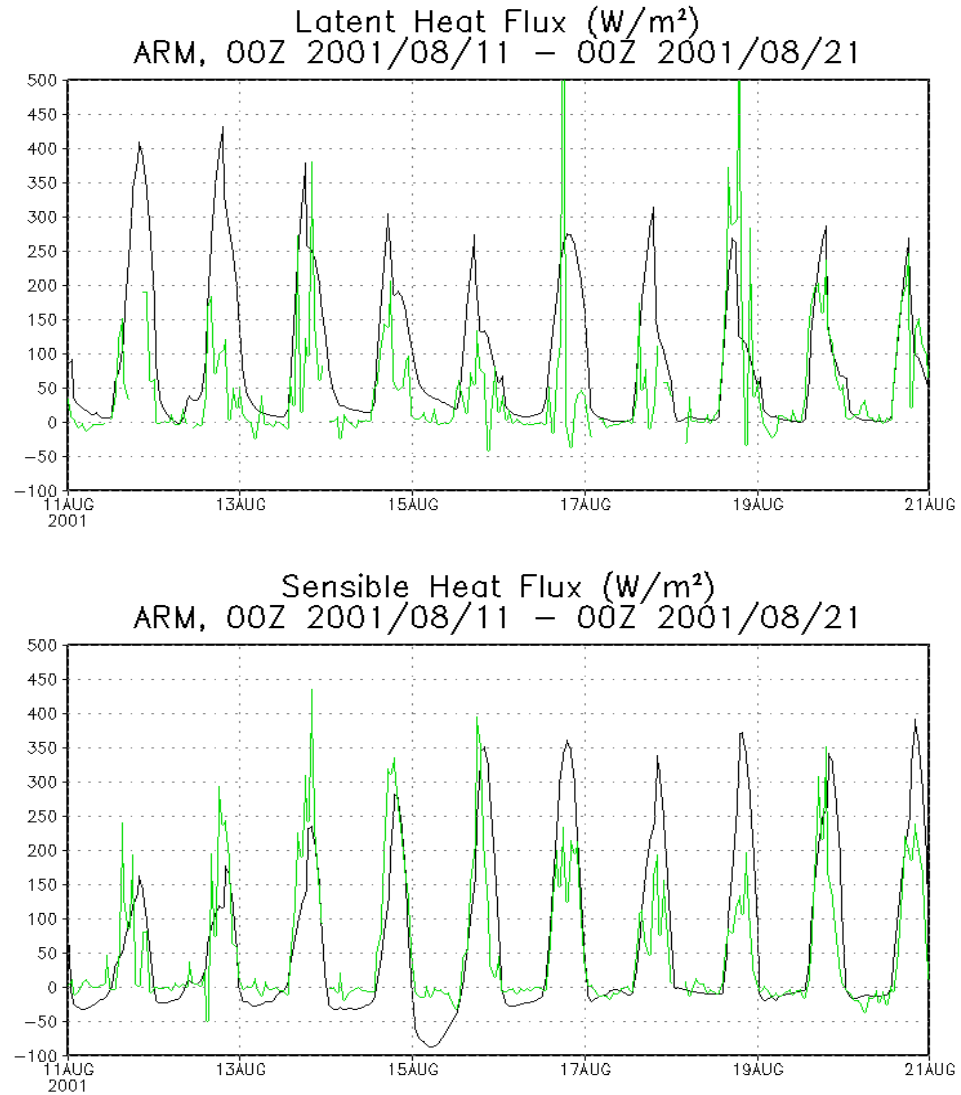
Oklahoma) and the observations.

Figure 3.10: Latent heat and sensible heat flux comparison.

Over all, the model simulates the pattern of LH and SH fluxes on ARM site in Oklahoma, although there are still some discrepancies. For example, the observation shows two dramatic spikes of LH flux on 8/16 and 8/18, which are not in the model result; the model overestimates LH flux on 8/12, 8/15, and 8/17, overestimates SH flux on 8/16, 8/17 and 8/18, and underestimates the SH flux on 8/12 and 8/13. The model still suffers from the

unrealistic cloud formation. The model might be capable of doing a better job if we use another finer grid around the ARM site. The decreasing trend of daytime LH flux from 8/13 to 8/15 is captured; the increasing tread of daytime SH flux from 8/11 to 8/15 is also simulated.

Other meteorological parameters are not suitable for comparisons, because the measuring levels are too different from the model vertical levels.
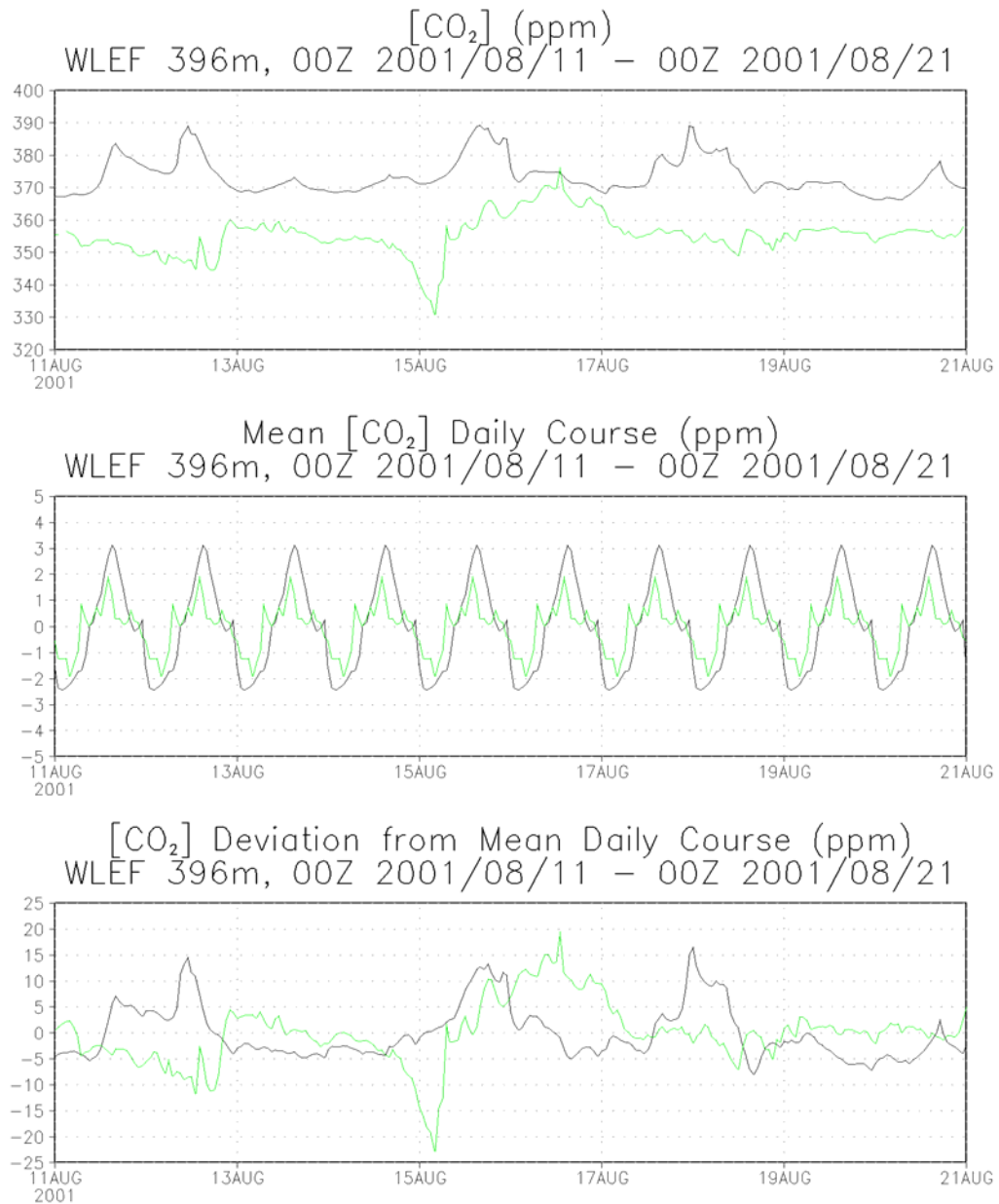
3.3 CO_2 Concentration and Flux Comparison

A. WLEF

Figure 3.11: CO_2 concentration, mean daily course, and its deviation at 396 m.

Figure 3.11 shows the comparison of CO_2 concentration between the model output and

the tower observation at 396 m. The upper panel shows the concentration, the middle one

shows the diurnal composite over this 10-day period, and the lower one shows the

deviation from the diurnal composite. Note that the model is initialized with 370 ppm of CO_2 homogeneously at the first hour of 8/1 so that the persistent gap between the model output and the observations is likely due, at least in part, to the higher initial CO_2 field.

There are three significant events in the observations. The first is the $[CO_2]$ jump on 8/12; the second is the strong dip on 8/15, and the third one is the spike on 8/16. The anomalies are $\pm$ 10 – 20 ppm.

The model does not simulate the strong dip as shown in the observations on 8/15. The cause for that strong dip was probably horizontal advection of lower $[CO_2]$ air, because it happened at night, when there was only respiration releasing CO_2 into the air. There is a $[CO_2]$ spike both in the model output and the observations around 8/11 and 8/12, and there is another one shown around 8/15 and 8/16. The timing of the spikes in the model is at least 20 hours earlier than in the observations. The model CO_2 spike on 8/15 might be caused by the CO_2 advection coming in from the south, and it happens too early in the model. This speculation can be supported by the wind direction mismatch shown in Figure 3.5, and it will be discussed again in Section 3.4.3.

Considering the mean $[CO_2]$ daily course, we can see that the diurnal amplitude in the model output is about 1 ppm larger than in the real world for daytime hours and 0.5 ppm more negative for nighttime. The diurnal signal over this period is so small, so deviation from the mean daily course shows a very similar pattern. The model might suffer from some unknown mechanism resulting in the spikes on 8/11, 8/12, and 8/17.
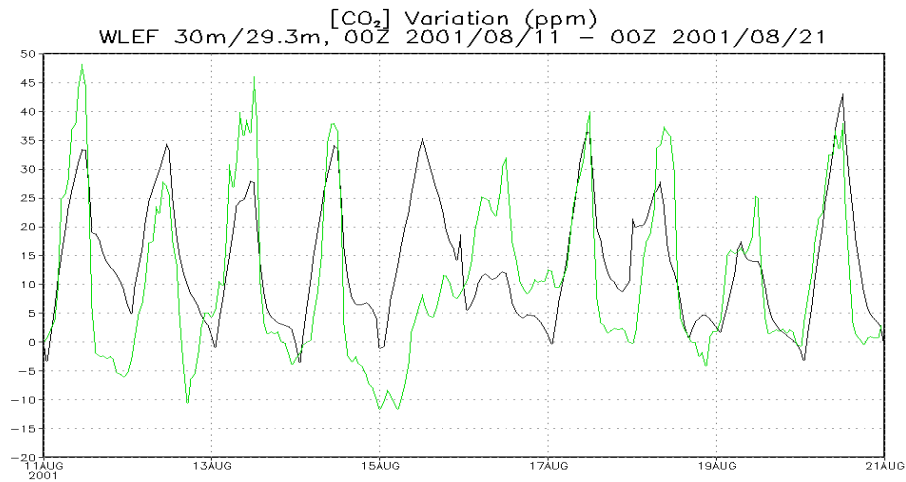
Figure 3.12: CO_2 concentration comparisons at 30 m.

Figure 3.12 shows [CO_2] anomalies at 29.3 for the model and 30 m for the observations.

The model does a very good job and catches the amplitude and timing of diurnal cycle. It

is a pity, however, the only spike during 8/15 – 8/16 is shifted by at least 20 hours earlier.

The strong dip on early 8/15 is missing in the model too. This expresses the difficulty of
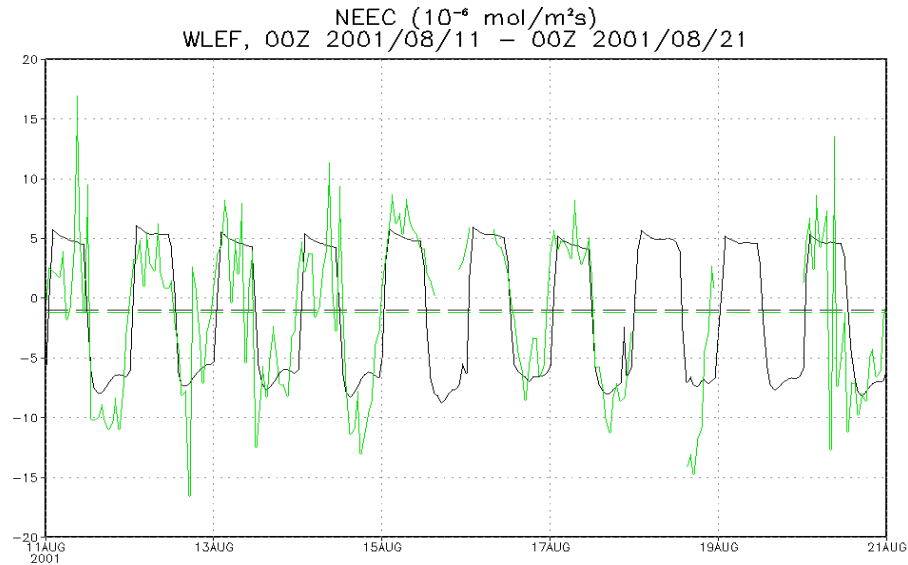
simulating CO_2 signals.

Figure 3.13: Net ecosystem exchange of carbon.

Figure 3.13 shows the comparison of net ecosystem exchange of carbon (NEEC) between

the model output (from SiB) and the observations (measured at 30 m, including the

storage change below 30 m). The green dash line is the time mean for observation over

this period, while the black dash line is the time mean for the model output. We can see

that the pattern in the model output is very fixed, though there is a slight decrease of

negative NEE on 8/18. The model underestimates the daytime negative NEEC on 8/11

and 8/14. Also the model underestimates the nighttime positive NEEC on 8/15. Over all,

the NEEC graph shows the model's reasonable skill in estimating the day-to-day NEEC

variation.

The observations of NEEC show a rather noisy pattern. This is because the data are

derived from eddy covariance of [CO_2] and vertical wind. In the real world, these two

parameters always change with time very quickly, and the observations are also made in the time scale of seconds. In the contrast, the model output is based on the model equations that parameterize the photosynthesis and respiration mechanisms of the plants, and hence it is much more regular due to the stability of numerical computation at each time step.
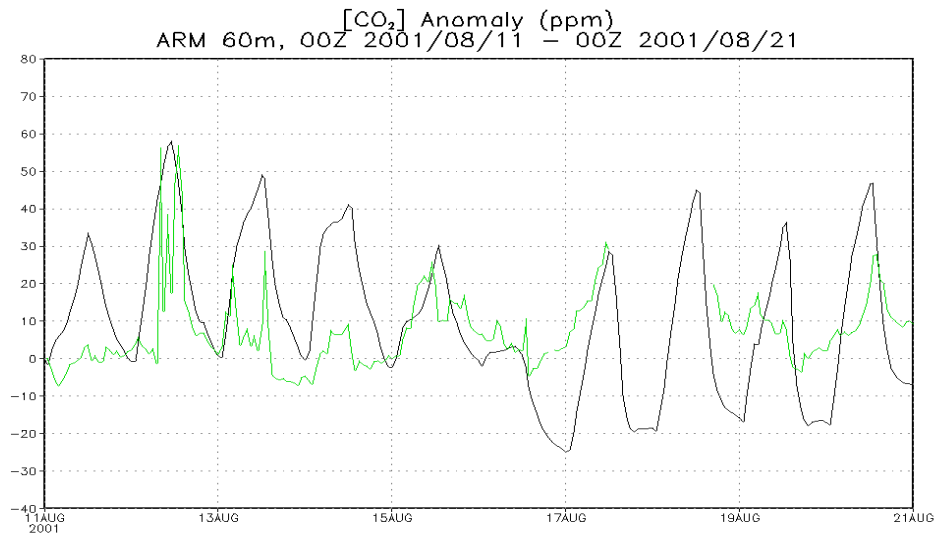
B. ARM

Figure 3.14: CO_2 anomaly comparisons.

Figure 3.14 shows the comparison of CO_2 concentration anomalies between the ARM site observations (60 m) and the output of the closest model point and the closest level (29.3 m). We can see that the amplitude is overestimated in the model except on 8/12 and 8/15. Part of the reason is because the observation height is different from the closest

model level, but the model still produces too strong variation higher aloft (not shown). The model output shows a decreasing trend continuously from 8/12 to 8/16, consistent with the observations from 8/12 to 8/14. Except for the trend, only the timing of the diurnal cycle and the turning point on 8/16 is captured.

CO_2 flux data from the ARM site is not used in this analysis because it is not comparable at all. Some spurious negative dips as strong as 40 umol/m^{2}s and a positive spike as strong as 22 umol/m^{2}s are present in the daytime observations. These are not reasonable at all, so I have chosen to omit a comparison with the model output.

3.4 Discussion

This discussion includes analysis of the ecosystem response to the weather change, vertical mixing, and horizontal transport. The first part will use only tower observation data and try to explain the contribution of the ecosystem to CO_2 variation in this case study. The second and third parts will adopt the model output and support the ideas of the importance of horizontal transport.

Some part of this section will focus on 12Z 8/14 – 12Z 8/18, a four-day period with the frontal arrival in the middle (13Z 8/16). The reason for this is because [CO_2] at all tower observation levels started to rise about 33 hours before the arrival of the cold front by about 40 ppm at each level. The concentration then decreases accompanied with night spikes at lower levels after the arrival, by about 35 ppm in 48 hours. This section will

address the possible reasons for this complex phenomenon, based on the three hypotheses in Chapter I.

3.4.1 Local Ecosystem to the Weather Change

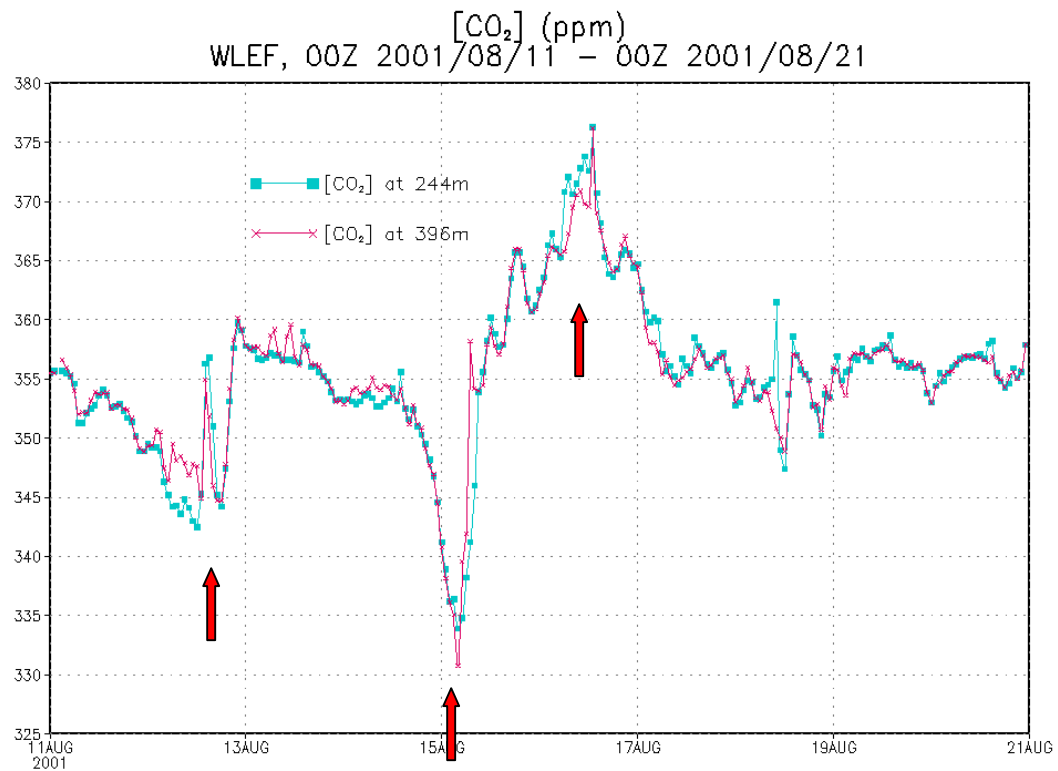3.4.1.1 Some Analysis Based on Observation Data

Figure 3.15: CO_2 concentration at 244 m and 396 m of WLEF tower.

Figure 3.15 shows [CO_2] data at two different levels (244 m and 396 m) on the WLEF

tower from 8/11 to 8/21. This figure is similar to Figure 2.11, but the x axis now is in

Greenwich time. The front arrived at WLEF at 13Z 8/16. Again, there are three possible

synoptic "events" shown here - the jump on 8/11, the strong dip on 8/15, and the peak on

8/16. They affect the entire tower. The CO_2 concentration increased 42.4 ppm at 244 m

and 45.4 ppm at 396 m on 8/15 and 8/16; this event is quite phenomenal, especially when
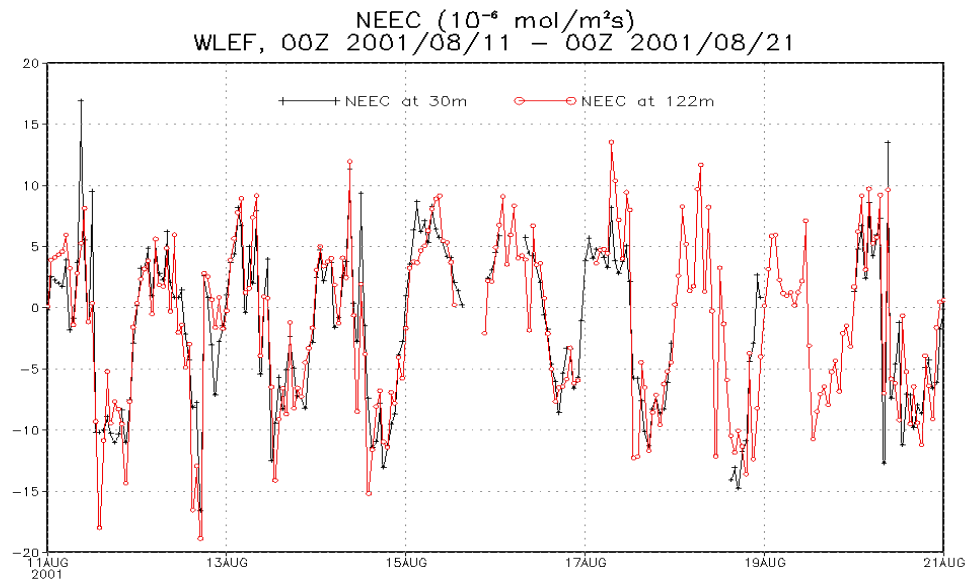
it was captured at both the 244m and 396m levels.

Figure 3.16: NEEC at 30 m and 122 m of WLEF tower.

Figure 3.16 shows the NEEC data for the period of interest at the 30m and 122m levels of

the WLEF tower. The NEEC at 30 m is the sum of the change of CO_2 storage below 30 m

and CO_2 flux at 30 m, and similarly for 122 m. The NEEC at 396 m is not shown here

because it is too noisy as a result of its taking into account the storage changes at all

levels below. We can see that although there is a significant dip of [CO_2] at 244 m and

396 m for the first few hours of 8/15 (Figure 3.15), the NEEC is actually a little higher

than usual at that time.

Unfortunately, we are missing six data points for NEEC during the daytime of 8/15. The

NEEC at 122 m has one negative value right after the missing period, and the NEEC at

30 m and 122 m are both about zero right before the missing period.

The radiation data at WLEF after 8/15 is missing. The best substitute for that is the PAR

data under full cover from the Willow Springs research site (Latitude: 45 degrees 47

minutes N, Longitude: 90 degrees 3 minutes W) 15 km southeast of the WLEF tower,

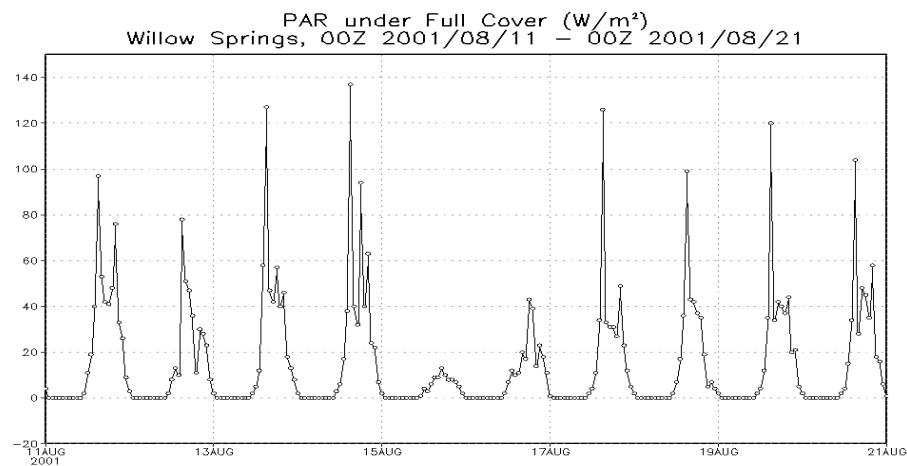because all other related data on the WLEF site or other sites nearby are missing.

Figure 3.17: PAR under full vegetation cover from Willow Springs research site.

94

Figure 3.17 indicates that it was likely very cloudy on 8/15 and 8/16, the key time before the front passed the WLEF tower, because the spikes on 8/15 and 8/16 are very small compared to the other days. This implies that the accumulation of CO_2 at the lower levels at night might not be depleted by photosynthesis during the daytime of 8/15.

Nighttime temperature at the 30-m level of the WLEF tower (Figure 3.6b) on 8/15 is the highest during the period of interest, and its variation on the following day is the smallest. This might explain why the nighttime respiration on 8/15 is a little higher than usual. The weather station data nearby (Phillips, Price County, Wisconsin) shows that the sky started to be overcast since 11Z 8/15. Phillips is at 45.7N, -90.4W, about 25 km south of WLEF tower. It is shown by the station data that the clouds covered the sky from 11Z 8/15 to 10Z 8/17, with only a few other sky conditions in between (1 "CLR", 3 "SCT", and 2 "BKN"). The clouds shaded the surface from sunlight and thus photosynthesis rate might be lower than usual, accompanied by lower temperature. Also, this explains the small LH and SH flux and low temperature on 8/16 (cloudy sky).

Does that mean that the ecosystem response to the weather change is the one and only reason for the $[CO_2]$ dip on 8/15 and spike on 8/16? We need another approach to prove or disprove that and to quantify how much it is responsible for.

3.4.1.2 Vertical Flux Divergence and Other Contribution

CO_2 concentration is determined by surface source/sink and advection as follows:

$$\frac{DC}{Dt} = \frac{\partial C}{\partial t} + u\frac{\partial C}{\partial x} + v\frac{\partial C}{\partial y} + w\frac{\partial C}{\partial z} = S(x, y, z, t),$$

where C is the concentration, u, v, and w are the wind velocities in the x, y, and z directions respectively, and S is the source strength, which has the unit of concentration over time. Let's consider a vertical air column and assume that the source/sink exists only on the surface and that the air is non-divergent, which is true most of the time. Then, we have the average time rate of change of CO_2 concentration in that column aloft as shown in Equation 3.1.

Equation 3.1

$$\frac{\Delta\overline{C}}{\Delta t} = -\int_{z_1}^{z_2}\left[\overline{\vec{u}_{2d}\cdot\nabla_{2d}\overline{C}} + \overline{w}\frac{\partial\overline{C}}{\partial z} + \nabla_{2d}\cdot(\overline{\vec{u}'_{2d}C'})\right]dz - \left[\overline{w'C'}\right]_{z_1}^{z_2}$$

$$= -\int_{z_1}^{z_2}\left[\overline{\vec{u}_{2d}\cdot\nabla_{2d}\overline{C}} + \overline{w}\frac{\partial\overline{C}}{\partial z} + \nabla_{2d}\cdot(\overline{\vec{u}'_{2d}C'})\right]dz - (F_{z_2} - F_{z_1})$$

where $\overline{C}$ is the time mean [CO_2] in the air column, C' is its anomaly, $\overline{\vec{u}_{2d}}$ is time mean horizontal velocity, $\vec{u}'_{2d}$ is its anomaly, ∇_{2d} is the 2-D divergence operator, z_1 and z_2 are two different heights, and F represents vertical turbulent flux. Note that S is gone, because there is no source/sink for a column that does not reach the ground surface. Here I define estimated [CO_2] as the concentration starting from some specific time plus the contribution from the difference of vertical fluxes between above and below the level of interest. This means:

$$C_{est,n} = C_0 + \Delta C_{est} = C_0 + \sum_n (\overline{w'C'})_n\Big|_{z_1}^{z_2}\Delta t_n\,.$$

How much can the flux difference at two levels change the CO_2 mixing ratio? Let's say

there is a column between 30 m and 122 m, with the base area 1 m^2. The column volume

is then

$$V = (122m - 30m) \times 1m^2 = 92m^3.$$

The total mole number of the air in that column is

$$n = \frac{PV}{RT} = \frac{P \times 92}{8.314 \times T} mol.$$

1 $\mu mol / m^2 s$ of flux difference can contribute 1 μmol to the column in 1 second.

Therefore, the CO_2 mixing ratio is changed by

$$\frac{\Delta C}{\Delta t} = \frac{1}{n} \frac{\mu mols^{-1}}{mol} = \frac{8.314 \times T}{P \times 92} ppm / s.$$

The base area is only a dummy variable. For instance, assuming that the layer between

122 m and 30 m is well mixed, if the flux difference is 1 $\mu mol / m^2 s$ with $P = 95kPa$ and

$T = 290K$, the CO_2 mixing ratio is changed by ~ 1 ppm in 1 hour in that layer.

Figure 3.18 shows that the estimated and observed CO_2 concentrations at 76 m and 244 m

of the WLEF tower for a period around 8/16. Here I use z_1 and z_2 as 30 m and 122 m,

respectively. Note that 76 m happens to be the middle point of the layer between 30 m

and 122 m. Therefore, if CO_2 in the layer is well mixed or it increases or decreases with

height linearly, the estimated CO_2 concentration at 76 m can well represent the mean

concentration of the layer. The same is true for 244 m. The gaps exist due to data

discontinuity; any of the measurement discontinuities at the two levels (30 m and 122 m)

will cause a break of the estimated [CO_2] line. We can see that the estimated

concentrations can be much different from the observed. This implies the importance of

the contributions other than vertical turbulent flux. These contributions may be horizontal

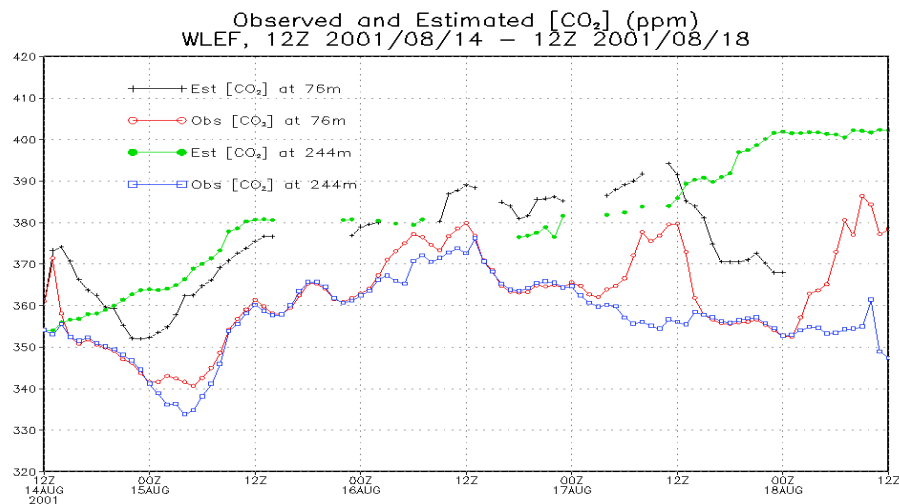advection, vertical advection, and/or horizontal turbulent fluxes.

Figure 3.18: Observed CO_2 concentrations and estimated CO_2 concentrations from vertical flux divergence. The discontinuities are due to missing data, and every succeeding line starts with the end of its proceeding.

Clearly, if we neglect the first term (the integral term) on the right hand side of Equation

3.1, we will misinterpret the influence of vertical fluxes. The black line and the red line

follow each other in a good manner, while the blue line and the green line deviate from

each other a lot. This implies, at least in this case, CO_2 concentration at lower levels is

significantly influenced by vertical flux divergence/convergence, while at upper levels

CO_2 concentration is influenced largely by horizontal advection ($\overline{\vec{u}_{2d}} \cdot \nabla_{2d}\overline{C}$), vertical

advection ($\overline{w}\dfrac{\partial \overline{C}}{\partial z}$), and/or horizontal flux divergence [$\nabla_{2d} \cdot (\overline{\vec{u}'_{2d}C'})$]. On 8/14, 8/15, 8/17,

and 8/18, the vertical fluxes should contribute greatly to increase CO_2 concentration at 244 m, but the observations show a dip on 8/15 and a decreasing trend on the other days. We know that mean vertical velocity ($\overline{w}$) is usually very small and horizontal flux divergence is much smaller compared to horizontal advection term, so the discrepancy naturally comes from the horizontal advection between the two flux measurement levels (z_1 and z_2).

From Figure 3.18, it seems that horizontal advection, vertical advection, and/or horizontal flux divergence between z_1 and z_2 dilutes CO_2, while vertical flux divergence works to increase [CO_2]. But keep in mind that positive horizontal CO_2 advection below z_1 or above z_2 might be responsible for the vertical flux convergence in between. Therefore, horizontal advection can be an indirect reason for CO_2 rising.
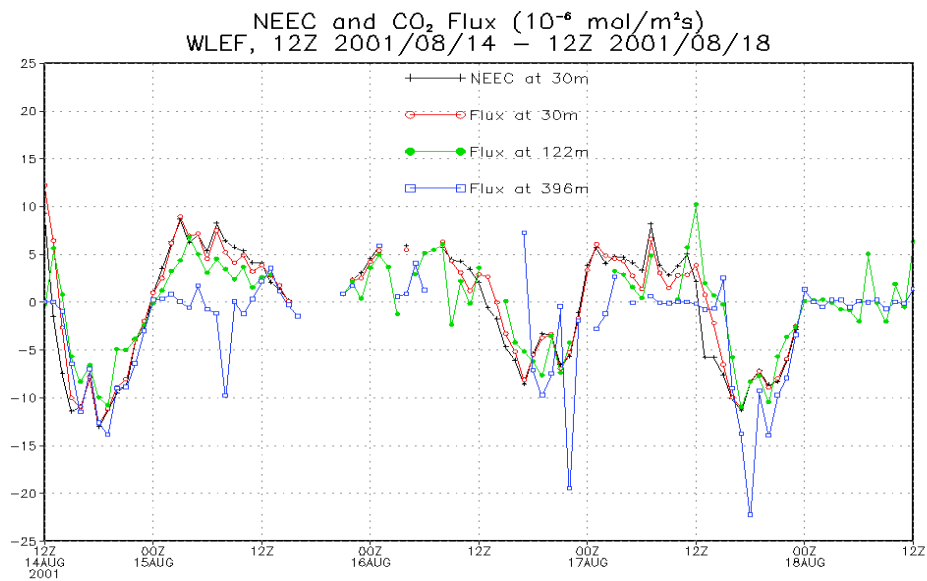

Figure 3.19: NEEC and vertical fluxes at three different levels.

Let's examine the time series of NEEC and CO_2 fluxes. Suppose that NEEC at 30 m is the best substitute for the real NEEC (we never know, since Figure 3.18 shows the importance of the horizontal advection and other mechanisms), does the ecosystem response to the weather change reflect in our tower flux measurements? The answer is that it is not always the case. Some negative values of vertical flux at 396 m occur at night on 8/15, and some negative values of vertical flux at 122 m occur at night on 8/16. Sometimes the flux at 396 m is very close to zero even when the NEEC is quite strong. This means that the signal from the ecosystem (positive flux by respiration) cannot reach higher levels and sometimes the signal is even reversed. During the daytime of 8/16 and 8/17, the negative flux is strengthened at 396 m (more negative). We know that there is not any anthropogenic or bio- source or sink except from the ground surface, so the strengthened part does not belong to the ecosystem.

3.4.1.3 The Signal from the Ecosystem

A simple calculation can make it clear that the ecosystem response to the weather change is not the only reason for CO_2 rising in this case. Assume that:

(1) the depth of mixed layer around the WLEF tower to be only 400 m (this covers 396 m and 244 m); above 400 m, there is a "lid" that blocks the signal on both upward and downward directions.

(2) CO_2 flux at 30 m represents the NEEC signal.

In Figure 2.11, we see that at night, the very shallow stable layer keeps the signal from traveling upward; thus $[CO_2]$ near surface is always higher than the level of 244 m and 396 m. The positive NEEC signal may not be able to reach 244 m and 396 m at all during the nighttime; hence at night, the rising signal detected at 244 m and 396 m with a stable layer below is less than the real signal from the ecosystem with a well-mixed layer up to 400 m. On the other hand, during the daytime, $[CO_2]$ at every level is well mixed and merges into one curve. Apparently the depth of the mixed layer during daytime is more than 400 m; hence, assumption (1) is very conservative for daytime use.

Just like Section 3.1.4.2, these two assumptions allow us to calculate time rate of change of $[CO_2]$ for the air column. Figure 3.20 shows the resultant calculations and compares them with observations.
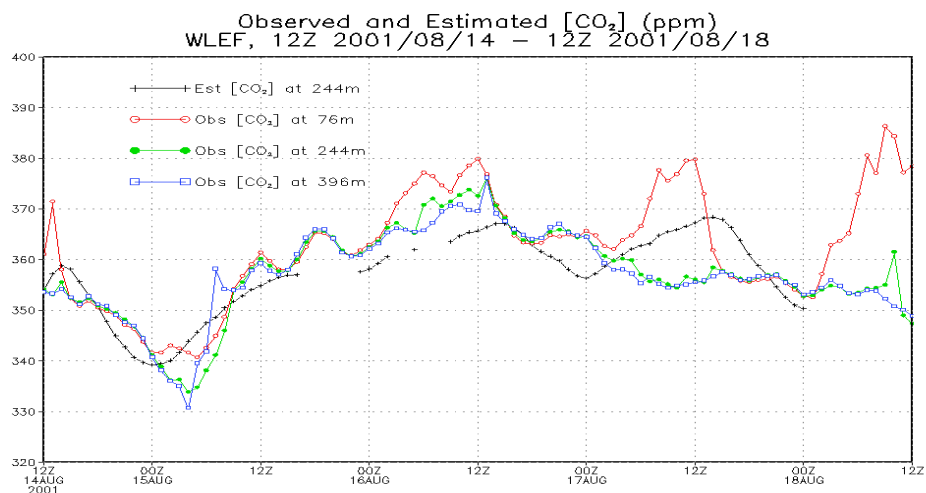
Figure 3.20: Observed and estimated $[CO_2]$ (ppm) based on the assumption of 400-m mixed layer and NEEC signal at 30 m.

Since [CO_2] is well mixed, the time rate of change of estimated [CO_2] at each level is exactly the same, although they might start from different values at 12Z 8/14; hence, only the estimated [CO_2] at 244 m is shown here. The difference of estimated [CO_2] between 00Z 8/15 (minimum) and 15Z 8/16 (maximum) is 27.9 ppm, while the difference of observed [CO_2] between 04Z 8/15 and 13Z 8/16 is 42.4 ppm for 244 m and 45.4 ppm for 396 m. Note that this estimate of 27.9 ppm is probably larger than it should really be in the real world, because the NEEC signal is either trapped near the surface (nighttime) or spread out all the way up higher than 400 m (daytime). Note that there are 6 missing data points during the daytime of 8/15 and 5 during the nighttime of 8/16.

If all our assumptions sustain, overall, NEEC in this case may contribute 2/3 of the rise at 244 m or 3/5 of the rise at 396 m in the period between 00Z 8/15 and 15Z 8/16. The CO_2 variation in this estimation is smaller than the observations, reflecting not only on the weaker dip on 8/15 but also on the milder peak on 8/16.

What if the depth of the mixed layer is larger than 400 m? Zhang (2003) and Denning *et al.* (personal communication) uses radar reflectivity and vertical profiles of CO_2 to investigate the depth of the mixed layer during the day and the depth of stable layer at night for summer time. Their results show that the depth of the mixed layer is more or less about 1,500 m during the day, and the depth of the stable layer is usually shallower than 200 m at night. Similar to their single-column model, we can use SiB-RAMS output to find out the depth based on the vertical potential temperature profile. It is found that in

our model, the depth of the mixed layer is more than 1,100 m during the daytime of 8/15, and before the CO_2 maximum hour (13Z 8/16) the depth has recovered from the nighttime trap to 750 m. Besides, the stable layer for the nighttime of 8/16 is only about 240 m deep. If the depth of the mixed layer is correctly estimated in SiB-RAMS, the contribution of the ecosystem to the CO_2 rising between 04Z 8/15 and 13Z 8/16 is even less than 1/3 for the rising at the 244-m level and less than 3/10 at the 396-m level.

3.4.1.4 Summary

At night on 8/15, respiration of the local ecosystem around WLEF was stronger possibly due to the warm air temperature. Although some important data are missing during the daytime of 8/15, it is likely that NEEC had very small or negative values in that period due to full-sky cloud cover. CO_2 continued to increase from 04Z 8/15 to 13Z 8/16, through two nights and one cloudy day. [CO_2] observations at 76 m and 244 m did not increase as much as the estimation based on vertical flux divergence method on late 8/14 and early 8/15, and it also increased during the daytime of 8/15. The discrepancy between the [CO_2] estimated from vertical flux divergence and observed [CO_2] indicates that horizontal advection might have strong effect on CO_2 concentration, with our usual assumptions of vertical velocity and horizontal flux divergence being very small. The ecosystem response to the weather change is not the only reason why [CO_2] increased so much in this frontal event, although it might contribute 1/3 of the rising within 33 hours.

3.4.2 Vertical Mixing

3.4.2.1 Model Results

Figure 3.21 shows the north-south CO_2 vertical profile from the ground surface to 18,000 meters for the first grid, cutting through the WLEF tower, together with meridional and vertical wind components and their temporal evolution. The WLEF tower is located at 45.9459N, and the vertical solid black lines denote its location in the figures. Vertical wind is very weak compared to meridional wind. This can be seen from the horizontally lying arrowheads. The reason for showing the N-S cross section instead of W-E during our period of interest is that the prevailing wind is in N-S direction.
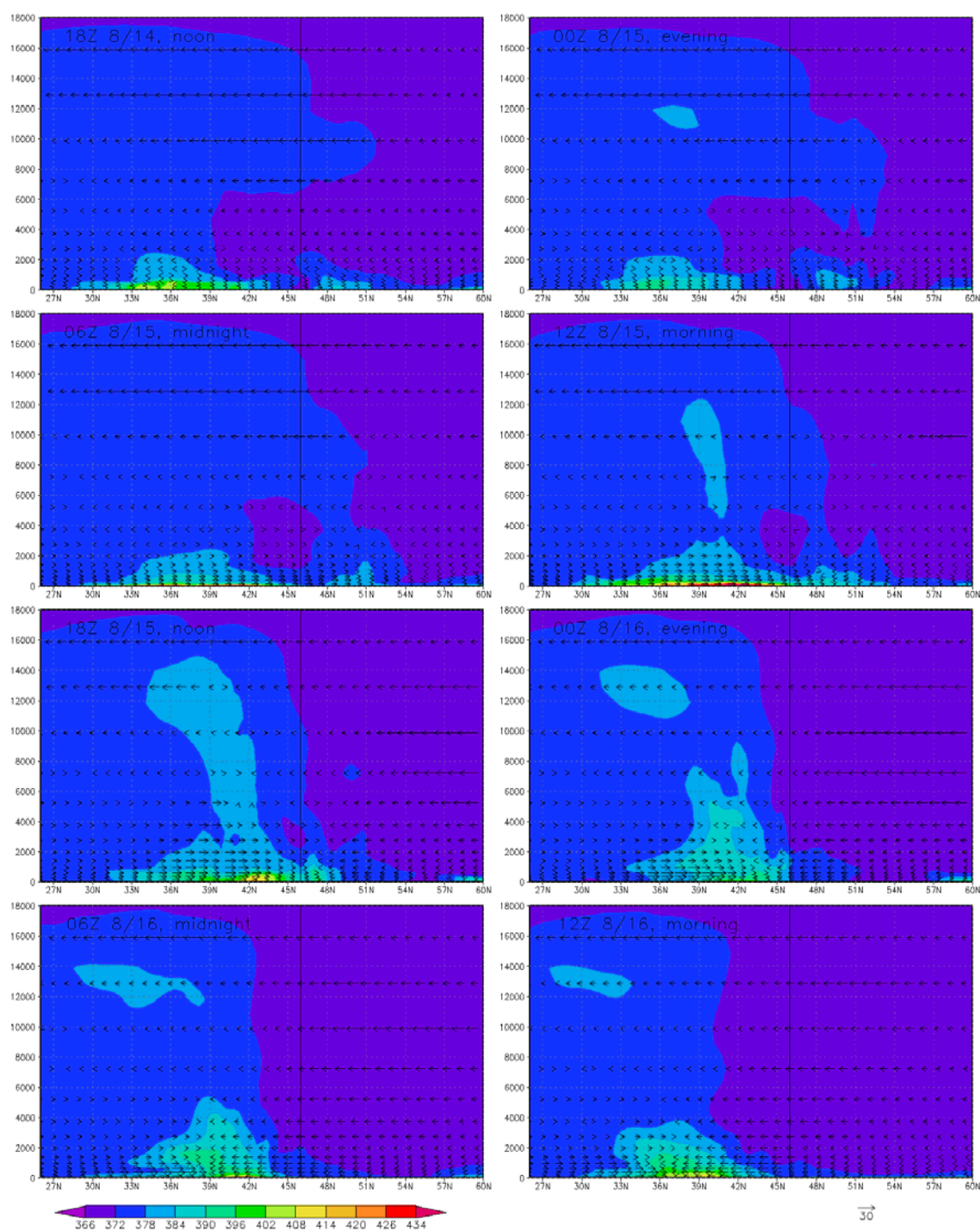
Figure 3.21: N-S CO$_2$ vertical cross section and wind vector for the first grid.

Figure 3.21 shows that there is a CO_2 maximum zone at about 35N (southeast corner of Missouri), and during the daytime (18Z 8/14 – 00Z 8/15) it is depleted. At night (06Z 8/15), CO_2 starts to accumulate in a wide area from 33N to 45N. The CO_2 boundary layer grows while the winds tend to transport CO_2 north in the lower levels. It will be shown later that the growth of CO_2 is related to near surface temperature. There is a convergence zone near the surface from 45N to about 49N, where wind direction switches.

The convergence zone then moves slowly to the south at first (12Z 8/15 – 00Z 8/16). CO_2 seems to be transported upward and a little to the south of the convergence zone. An interesting change occurs between 00Z 8/16 and 12Z 8/16. Let's ignore the possible source/sink from the surface for now. The high concentration zone is originally pushed to the north when it is located to the south of the convergence zone (00Z 8/16). Later on, the zone is pushed to the south when is located to the north of the convergence zone. The switch happens because the convergence zone moves faster than the high [CO_2] zone.

In the model result, the leading edge of the high concentration zone reaches the WLEF site (45.9459N) and resides there for a very short time (12Z 8/15 – 18Z 8/15). CO_2 around WLEF is depleted right after that.

Usually the CO_2 anomalies exist in the lower levels. Hence next we consider for the third grid and lower levels (0 – 2,000 m).
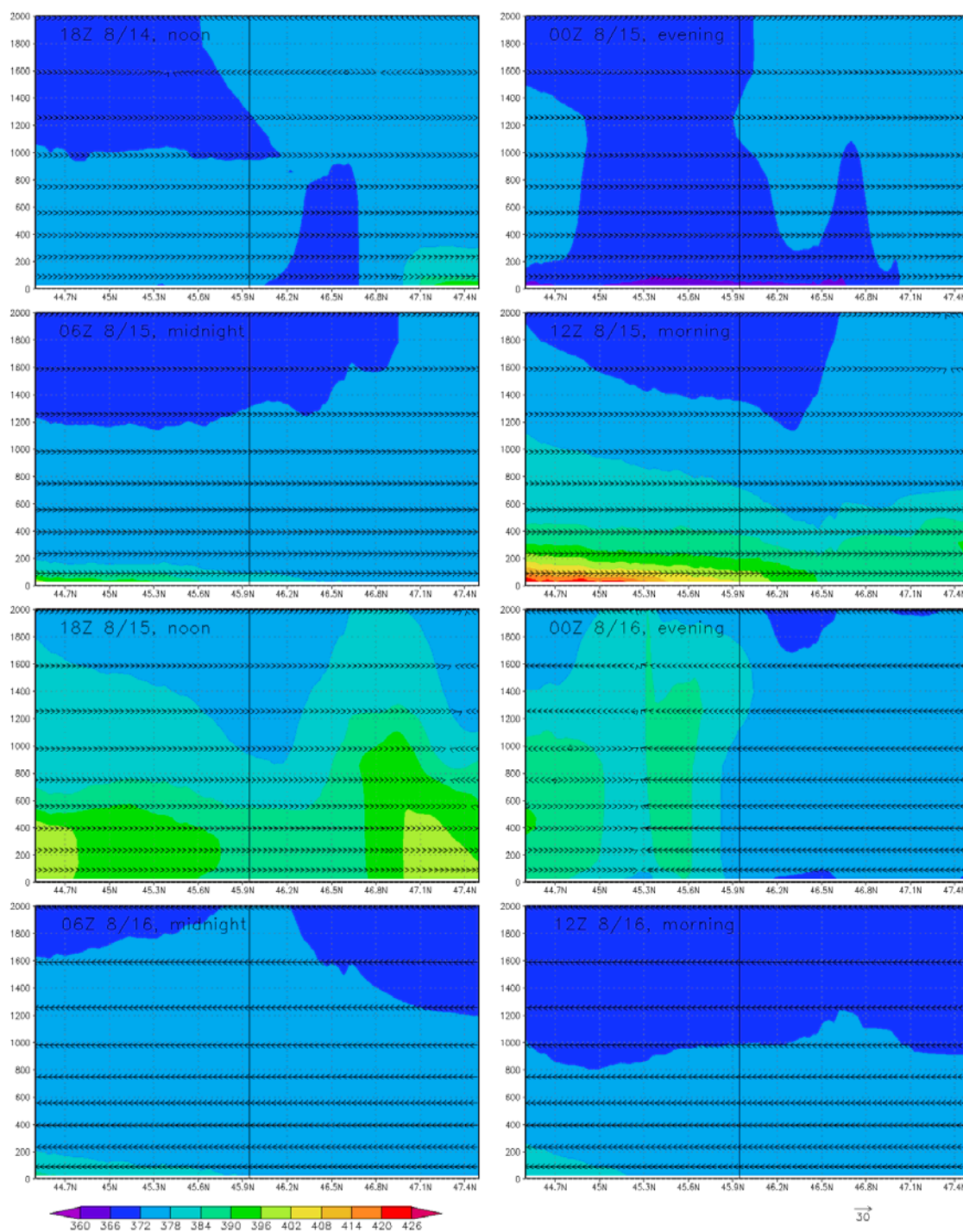
Figure 3.22a: N-S CO_2 vertical cross section and wind vector for the third grid and lower levels from 18Z 2001/08/14 to 12Z 2001/08/16.

This same phenomenon as shown in Figure 3.21 can be seen in Figure 3.22a as well. Note that Figure 3.22 only focuses on the boundary layer around the WLEF tower and that the color bar has different scales now. During the daytime of 8/14 (18Z 8/14 – 00Z 8/15), $[CO_2]$ is lessening, probably due to photosynthesis because we do not see any negative advection at that time. Photosynthesis consumes CO_2 while the mixed layer is growing. Another very shallow low $[CO_2]$ layer also comes out near the surface in the evening.

During the early nighttime of 8/15, respiration does its part and cuts off the low $[CO_2]$ layer from the surface and leaves it as a residual layer aloft. At 12Z 8/15, high concentration air is advected into the domain. The influence at 244 m and 396 m, though, might be small, since at those levels there is less than 12 ppm difference compared to 06Z 8/15. At 18Z on 8/15, high concentration air is pushed to the north continuously and transported to higher levels. This spreads out CO_2-rich air throughout the period between 12Z 8/15 and 00Z 8/16. Although the daytime photosynthesis on 8/15 is strong (see Figure 3.13 in the last section and Figure 3.23 in the following discussion about horizontal transport) near the WLEF tower in the model, it does not consume much of the CO_2 coming from the south, and there is not a low-$[CO_2]$ zone near the surface, as we would usually expect for the daytime. After that, the prevailing wind turns to head south, and the positive CO_2 anomaly is advected out of the domain.

In our data analysis, we found that the daytime photosynthesis around the WLEF tower on 8/15 could be very weak due to full sky cover. However, the model output does not

have it. Daytime photosynthesis and other dynamic reasons, such as diffusion and

horizontal transport, deplete CO_2 on late 8/15 and early 8/16. Thus the model output

shows a decreasing trend of CO_2 on the WLEF site after 17Z 8/15 (Figure 3.11 and

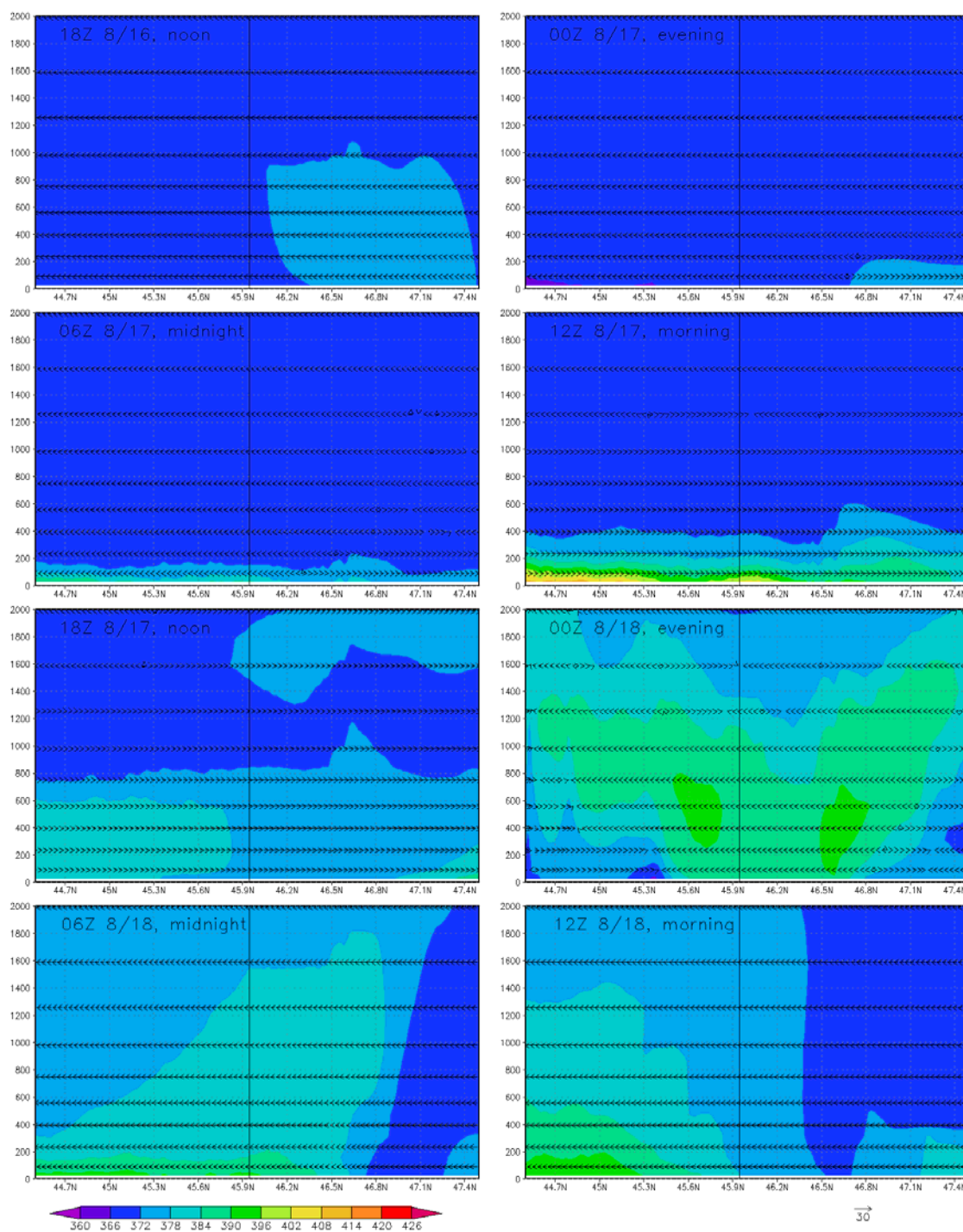Figure 3.12), which is 20 hours earlier than the observations.

Figure 3.22b: N-S CO_2 vertical cross section and wind vector for the third grid and lower levels from 18Z 2001/08/16 to 12Z 2001/08/18.

Figure 3.22b shows that low CO_2 concentration zone builds up during the day between 12Z 8/16 and 00Z 8/17 and a positive anomaly moves in from the north. The mixed layer can reach all way up to 2,000 meters in this area. At night (00Z 8/17 – 12Z 8/17), the low concentration zone is isolated aloft and decoupled from the developing high concentration zone due to nighttime respiration of the surface.

High concentration air intrudes from the west at 00Z 8/18 (cannot be seen in the figures), converges to the north of 46N, and moves to the south after that. Some of the remnants of the convergent high [CO_2] air stays; meanwhile a relative high CO_2 concentration boundary layer builds up again between 06Z 8/18 and 12Z 8/18 to the south of the tower.

3.4.2.2 Summary

The model results show that high CO_2 concentration air is advected into and out of Wisconsin twice in the period of four days. This frequent phenomenon is evidence that we must take into account the synoptic signal when we try to interpret the tower observations. Note the pattern that the leading edge of high CO_2 concentration air moves into the area around the WLEF tower. The air mass is very shallow and slopes upward to the south. Therefore, sometimes only the lower levels can detect the change (12Z 8/15, Figure 3.21) and this measurement should not be used to represent the entire column of air. When there is a convergence zone near surface, CO_2 can be transported upward. This transport can be as rigorous as at 18Z 8/15 (Figure 3.21), but usually, at least in this simulation, CO_2 anomalies stay well below 4,000 meters. If the atmosphere is relatively

unstable during the day and more stable at night, the negative anomaly caused by daytime photosynthesis can decouple from the surface (e.g. 06Z – 12Z 8/17, Figure 3.22b).

The simulation shows that vertical mixing (CO_2-rich air from the free troposphere, see Section 2.4) is not the reason for the CO_2 concentration rising by 45 ppm at 396 m of the WLEF tower in 33 hours, because the vertical wind velocity is always small and the signal is always from the surface or from the horizon. The process to produce the signal from the surface is slow, so is the CO_2 concentration rising; hence, a sudden vertical mixing is very unlikely to be the reason for this "slow motion".

3.4.3 Horizontal Transport

This subsection will emphasize on the role of horizontal advection in the model results. Both NEEC distribution and wind fields will be shown to locate CO_2 source/sink and to identify how horizontal advection does its work. The possible reasons for CO_2 source will be addressed. The influence of horizontal advection on the WLEF site will also be quantified.

3.4.3.1 Spatial Distribution of CO_2 and Its Evolution

There is a cross in each map, indicating the position of the WLEF tower.
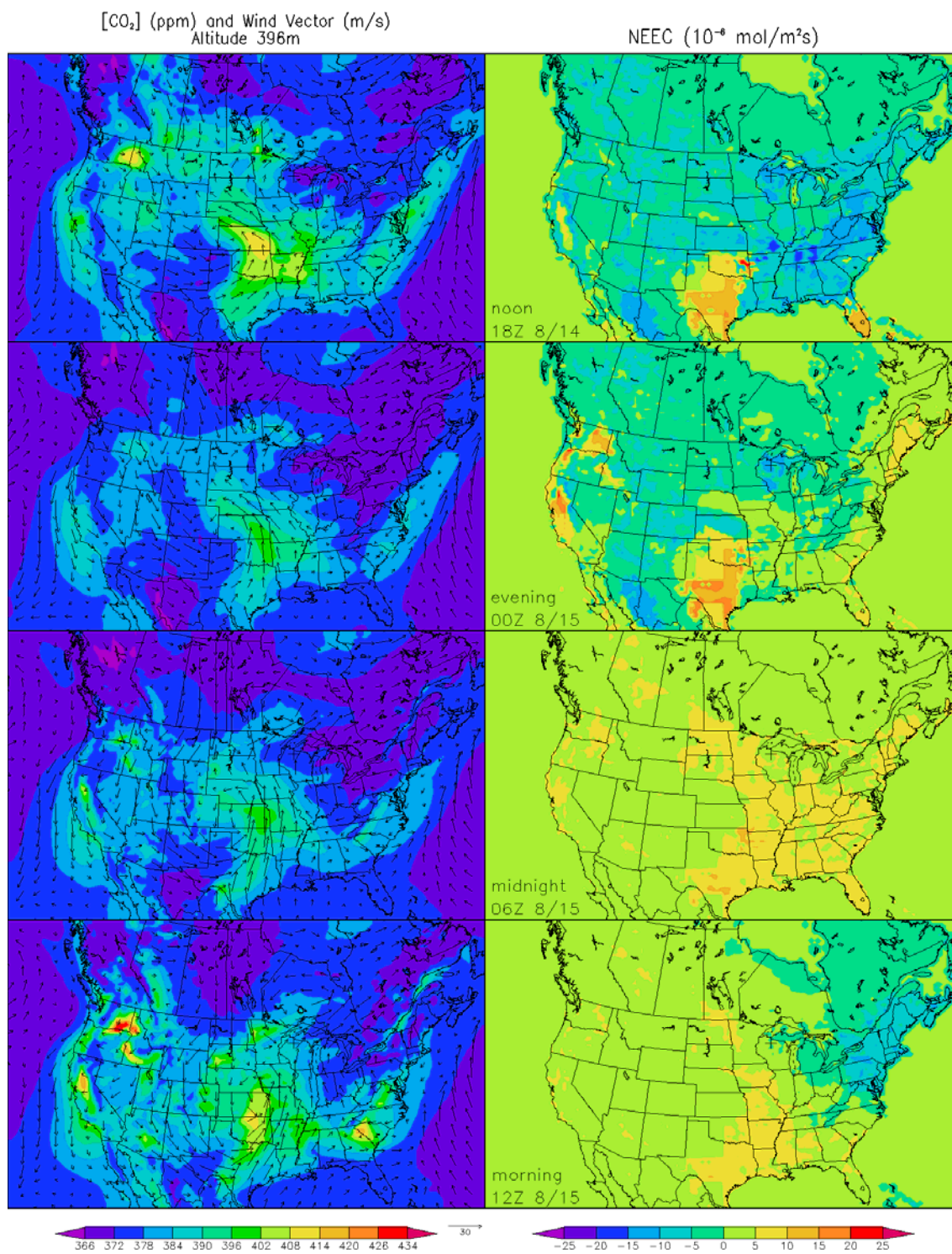
Figure 3.23a: CO$_2$ horizontal advection and NEEC from 18Z 2001/08/14 to 12Z 2001/08/15.

The left panel of Figure 3.23a shows CO_2 concentration and wind field at 396 m above the ground, while the right panels shows NEEC at the same time. We can see from the right panel that even during the day, Texas and Oklahoma are a significant source of CO_2 to the atmosphere. The southerly winds then advect this high CO_2 concentration air northward, over Kansas (as shown at 00Z 8/15), and thus high concentration zone is located to the north (Kansas) of the strong source (Texas and Oklahoma). When the wind direction shifts from southeast to southwest, the shape of high [CO_2] air mass also changes accordingly.
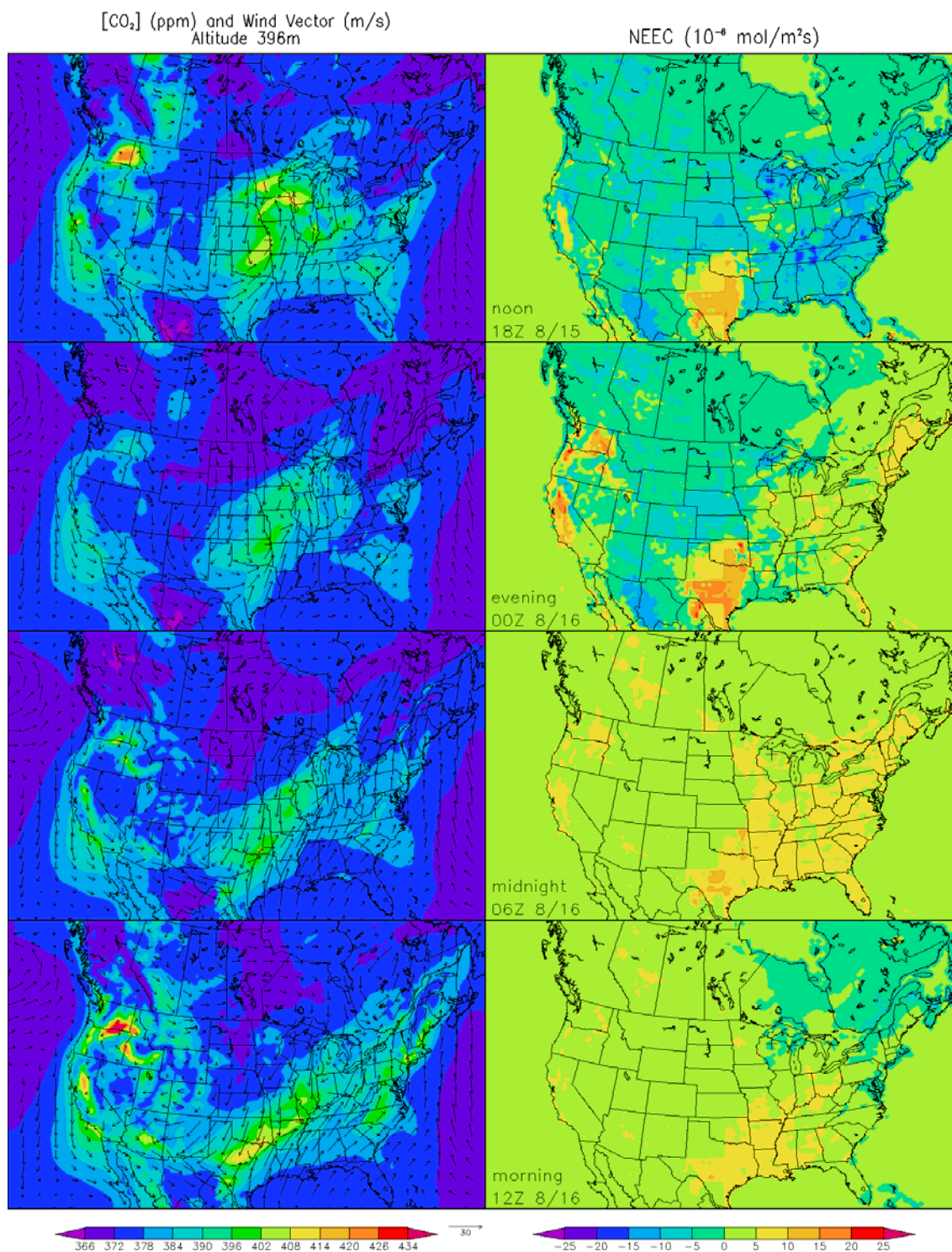
Figure 3.23b: CO_2 horizontal advection and NEEC 18Z 2001/08/15 to 12Z 2001/08/16.

The convergence zone in the Great Plains gradually forms and CO_2-rich air arrives in Wisconsin at 18Z 8/15. Northerly wind dominates in the upper part of the Great Plains and the southerly wind dominates in the lower part, causing this convergence zone. The relative low [CO_2] air from Canada mixes and replaces the high [CO_2] air around WLEF, and "cleans it up". All this happens before the arrival of the front at WLEF in the observations (13Z 8/16).

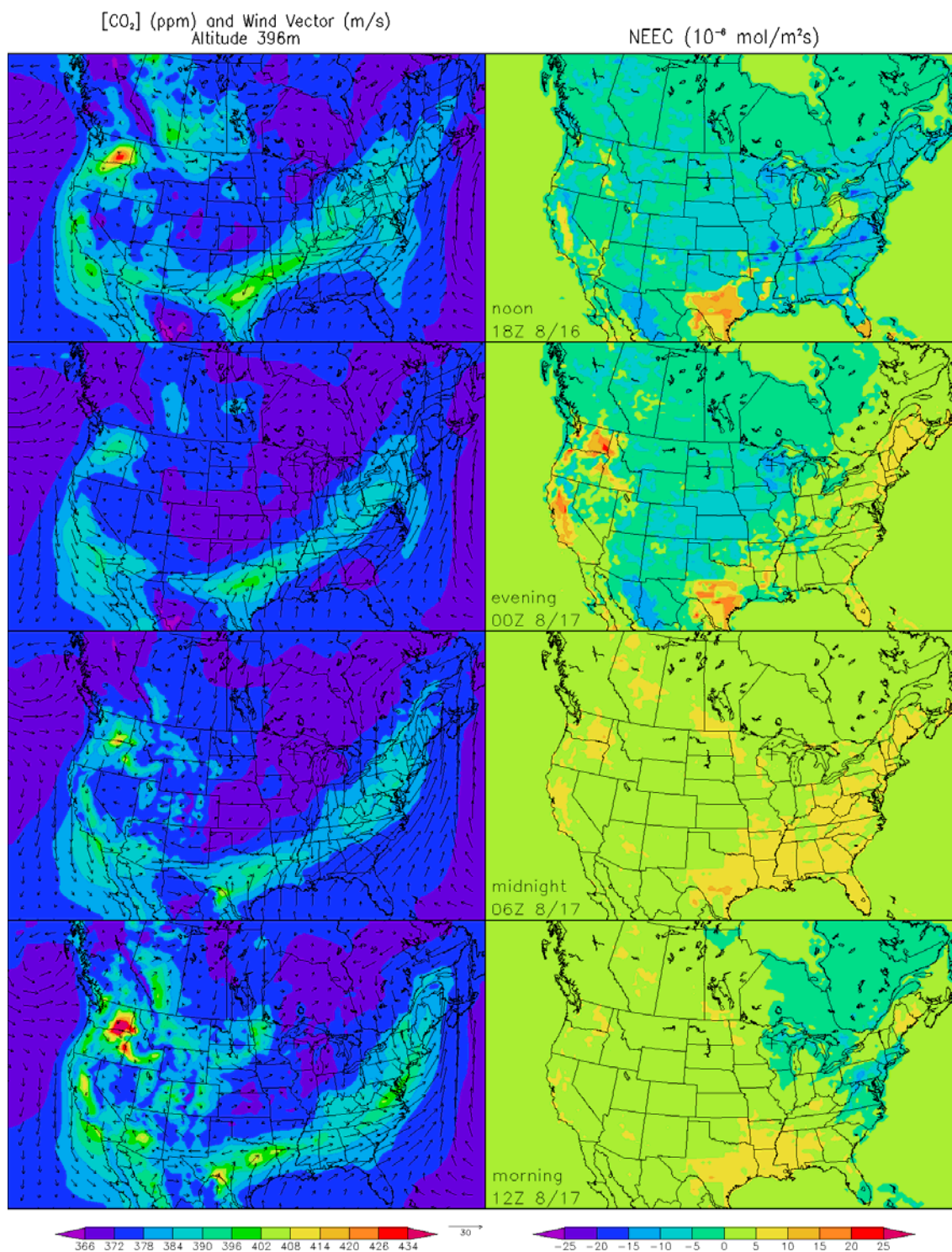**Figure 3.23c:** CO_2 horizontal advection and NEEC 18Z 2001/08/16 to 12Z 2001/08/17.

The huge convergence zone continues to grow and is aligned northeast to southwest across the entire east of the US. Note that most of the country, especially the states in the northeast, continue to draw down CO_2 during the day, Texas continues pumping out CO_2 and the winds advect this relative high [CO_2] air to the east coast.

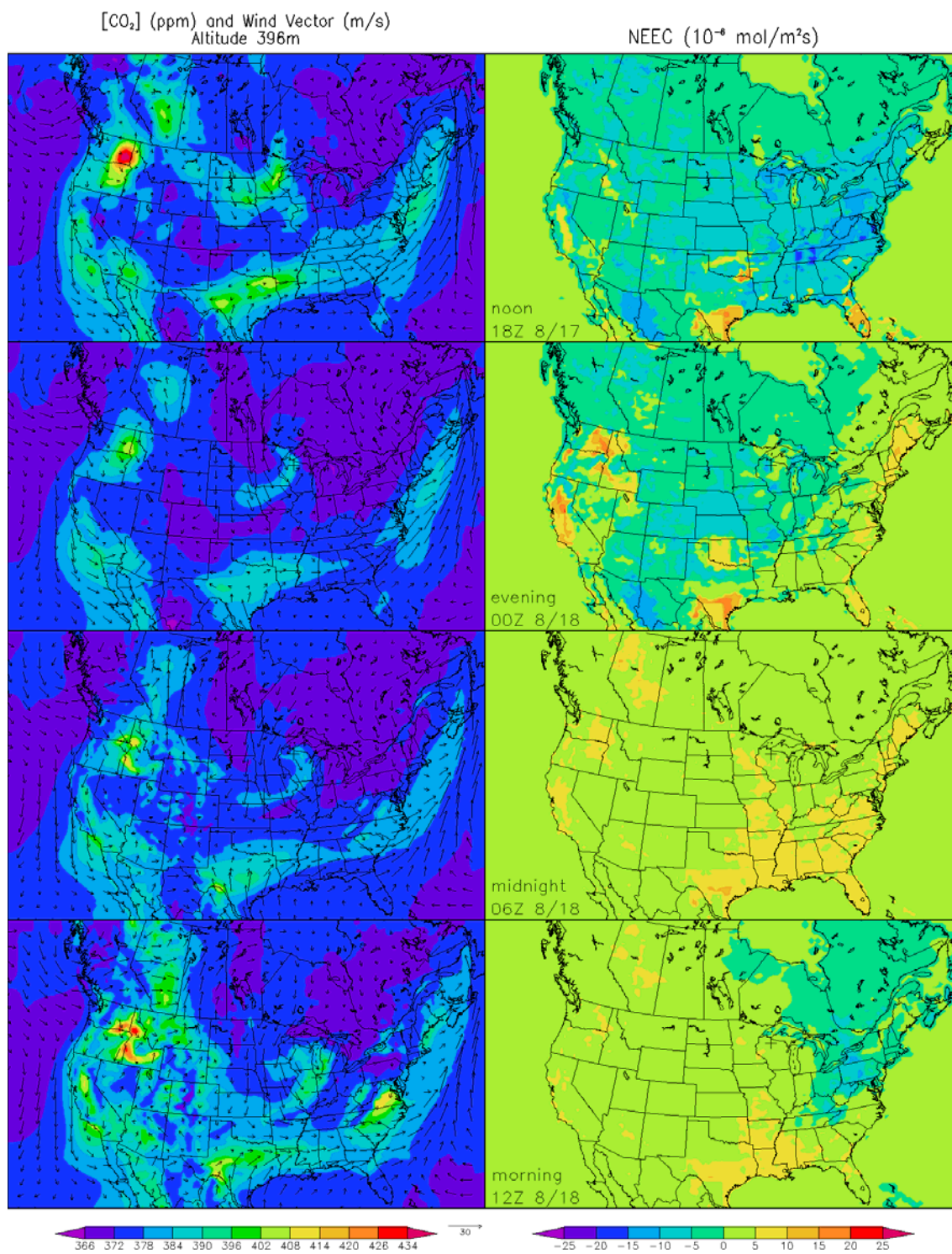**Figure 3.23d:** CO_2 horizontal advection and NEEC 18Z 2001/08/17 to 12Z 2001/08/18.

A small high [CO_2] zone also develops to the northwest of the WLEF tower (shown at 18Z 8/17), and the northwesterly flow advects that air mass across the tower 24 hours after the front. Northerly winds continue to dominate for the remainder of the period of interest.
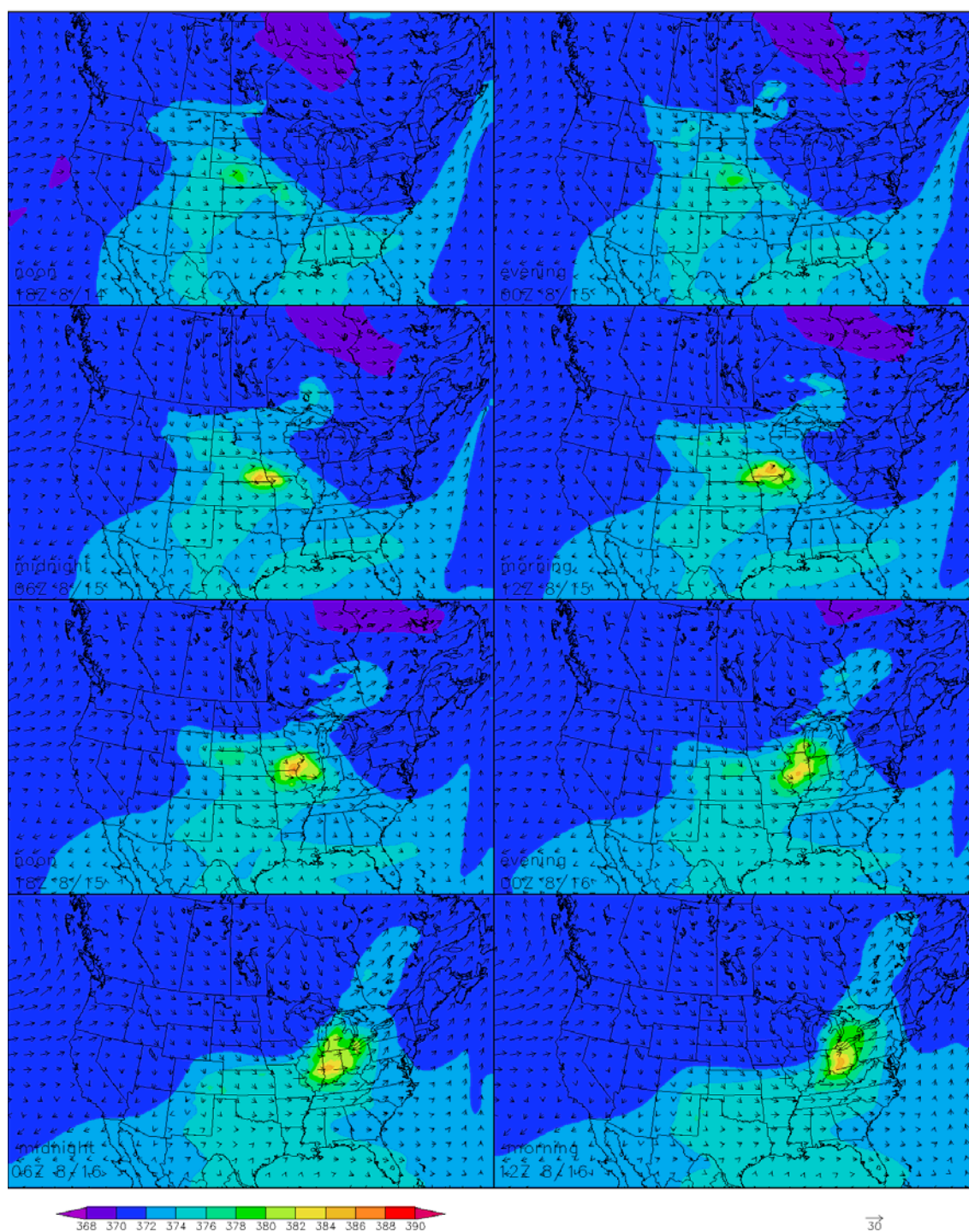
Figure 3.24: CO$_2$ concentration and wind vector in the mid-troposphere.

Figure 3.24 shows the [CO_2] and wind vector in the mid-troposphere. Note that the color bar has different scale now, and the interval is only 2 ppm. The maximum center is located to the east of low-pressure center (not shown), and its source is from below. CO_2 on 500-hPa pressure level comes from the convergence zone near the surface and is carried about 150 km away to the east by westerly. Although some of the signals from the surface can reach this high, they are quite weakened. Others never come up to the mid-troposphere, such as the one in Washington state at 12Z 8/15, because of the lack of coherent near surface convergence.

Two things are worthy of notice. First, the high concentration center on the 500-hPa level is not necessary right above or closely above the high concentration center near the surface. Apparently, the surface low-pressure center is strongly correlated to the CO_2 penetration and always located nearby in the horizontal coordinate. Secondly, our frontal case (the one that arrives at the WLEF site at 13Z 8/16) does not have too much influence on [CO_2] field. Instead, the other front that crosses eastern U.S. carries the anomalies with it to the east coast, which can be seen in Figure 3.23 and Figure 3.24.

The [CO_2] field in the mid-troposphere in the later time is not shown here, because it tells a similar story as follows. There gradually forms two air masses with different [CO_2]. The westerly winds sweep the anomalies to the east and the northerly winds "lock" them in the south. The low-pressure system that originates from the east side of the Rockies brings the [CO_2] "tide" to the upper Great Plains. The [CO_2] flood comes with the low-pressure system, while the [CO_2] ebb goes with its travel to the east coast.

3.4.3.2 High Temperature in Texas and Oklahoma

This part of the section will try to explain why Texas and Oklahoma are the source of CO_2 during the daytime on 8/14 and 8/15. SiB 2.5 considers three different "stress factors", stress factor of SWC at the second layer, stress factor of leaf surface temperature (or skin temperature), and stress factor of water vapor deficit. They regulate photosynthesis. SWC at the second layer changes slowly; it usually takes months before it can change stress factor of SWC to a significant degree. Leaf surface temperature and water vapor deficit, however, changes rather quickly, in the time scale of hours. Water vapor deficit is relative humidity difference between the leaf surface and the CAS, and hence is strongly related to CAS temperature. The difference between CAS temperature and leaf surface temperature is small. Figure 3.25 shows CAS temperature, which is easier to interpret than leaf surface temperature when we consider water vapor deficit.
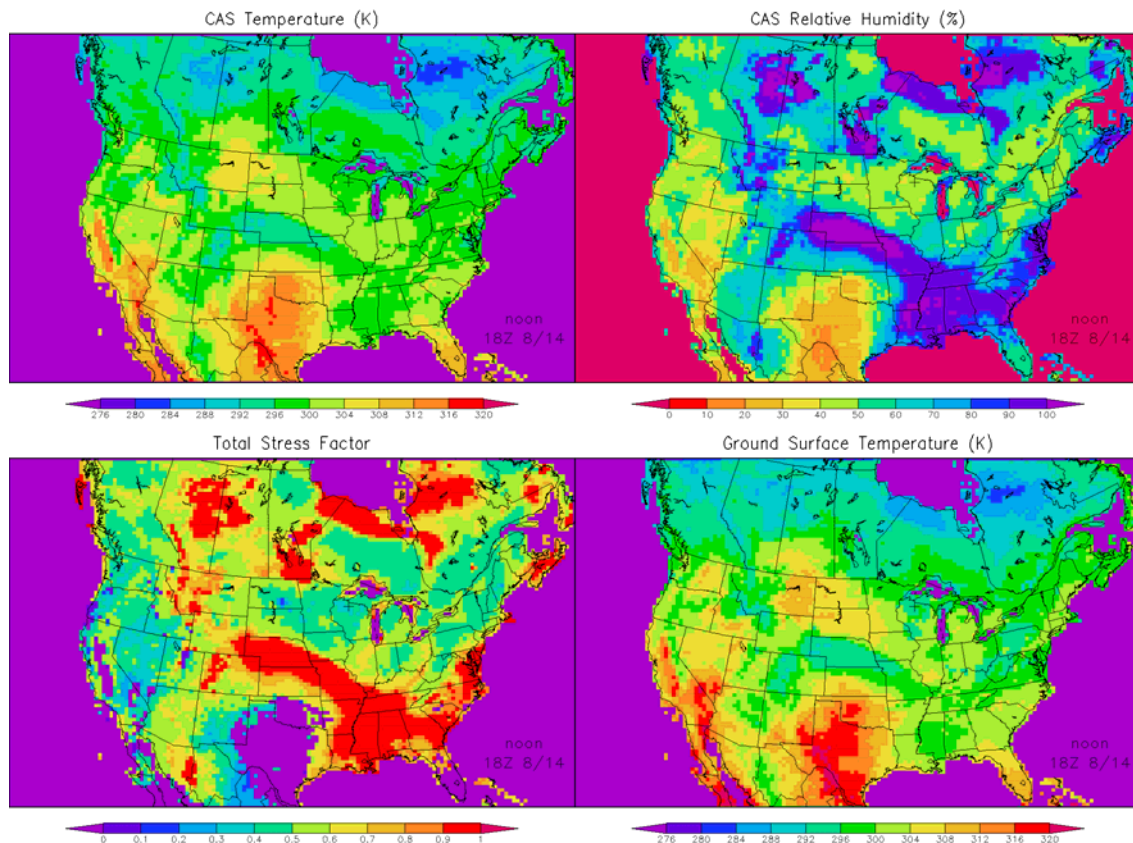
Figure 3.25a: CAS temperature, CAS relative humidity, total stress factor, and ground surface temperature for 18Z 8/14.

Figure 3.25a shows CAS temperature, CAS relative humidity, total stress factor, and ground surface temperature for the first grid at 18Z 8/14. 18Z is actually 12PM LST for the Midwest, when shortwave radiation is at a maximum. Texas and Oklahoma are extremely hot at that time. Also CAS relative humidity is very low (note that the color table is reversed), probably due to the very high temperatures. Therefore, total stress factor (the product of the stress factor of SWC, the stress factor of skin temperature, and the stress factor of water vapor deficit) is down to zero. The vegetation is just stressed out; photosynthesis in that area is shut down. The SWC and the stress factor of SWC are not shown because the stress factor is well above 0.9 (unstressed) throughout the period of

interest. Note that ground surface temperatures in the right lower panel are very high in Texas and Oklahoma. This enhances heterotrophic respiration in the soils, resulting in an additional efflux of CO_2 into the atmosphere.

There is a cool and humid area, which is accompanied by very high stress factor, sticking out from the lower Mississippi basin to Nebraska. It is associated with the rainy and cloudy weather.
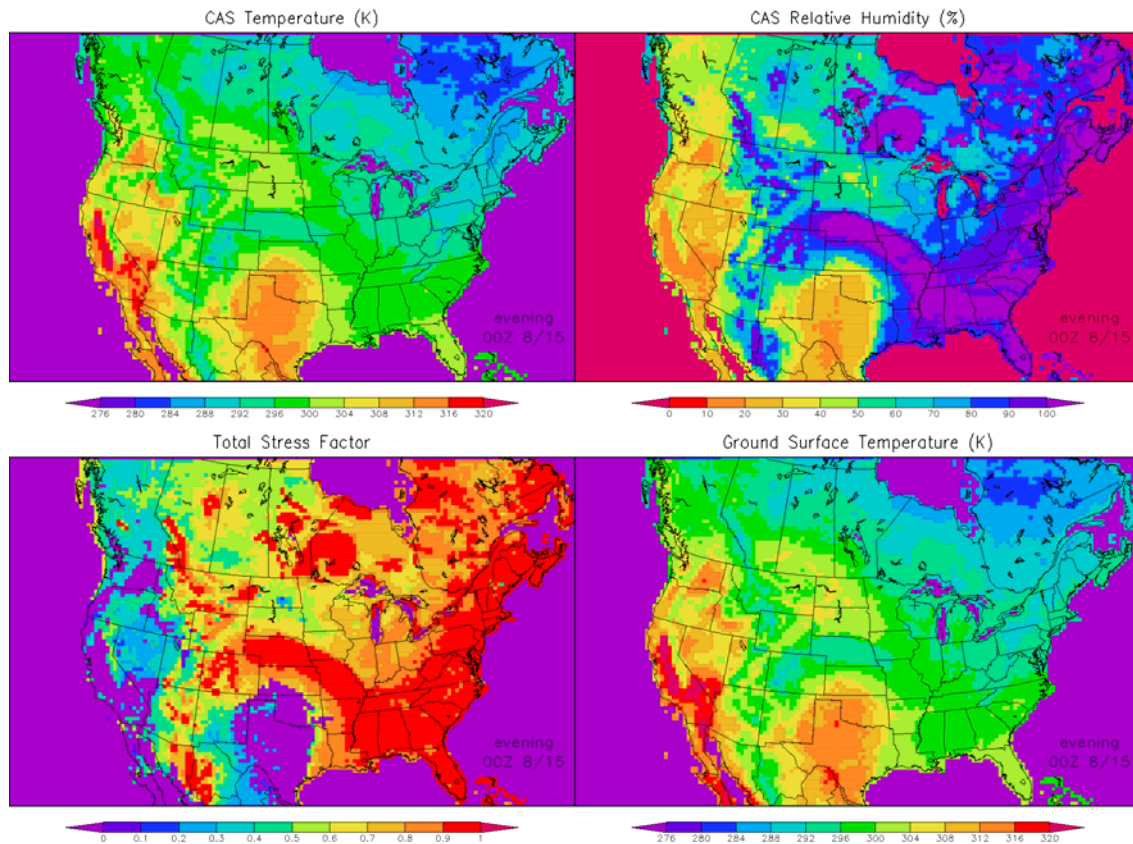

Figure 3.25b: CAS temperature, CAS relative humidity, total stress factor, and ground surface temperature for 00Z 8/15.

Figure 3.25b shows very similar pattern to Figure 3.25a, although it is 6PM LST for Texas. Extreme values of CAS temperatures are present in California, and Texas remains hot at dusk. This situation (the daytime "fire pot" in Texas and Oklahoma) continues for two days until the northerly winds bring cool air down to north Texas (see 18Z 8/16, Figure 3.23c). South Texas, where the southerly flow prevails, continues to suffer from the hot and dry air (from the perspective of relative humidity, not mixing ratio).

The daily highest temperatures of four cities in Oklahoma and Texas on 8/14 and 8/15 from the weather stations data confirm the existence of the heat waves. Oklahoma City (Latitude: 32.983, Longitude: -97.317, Elevation: 226 meters), Austin (Latitude: 30.3 degrees, Lon: -97.7 degrees, Elevation: 189.3 meters), Fort Worth (Latitude: 32.983 degree, Lon: -97.317 degree, Elevation: 226 meters), and San Antonio (Latitude: 29.333 degree, Longitude: -98.467 degree, Elevation: 176 meters) suffered from the hot air as high as 35°C (308K), 37°C (310K), 39°C (312K), and 38°C (311K), respectively.
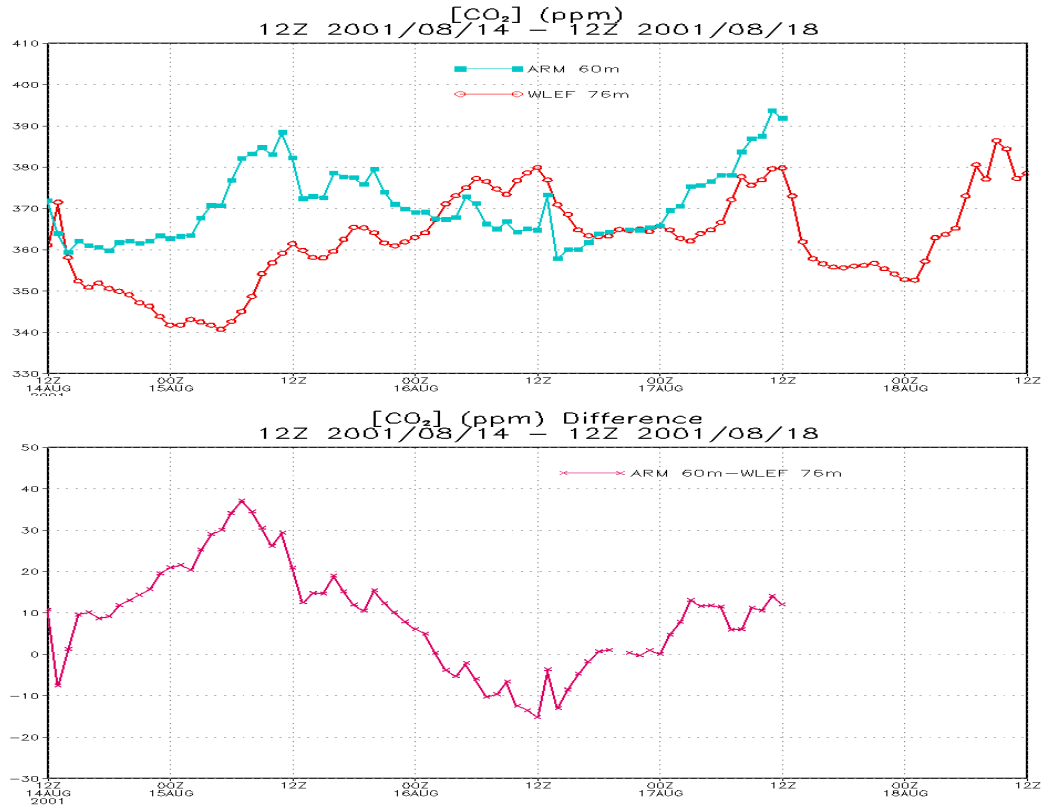
Figure 3.26: CO_2 mixing ratio at the ARM site for the period of 12Z 2001/08/14 to 12Z 2001/08/18 and its difference between the ARM site and the WLEF site.

Figure 3.26 shows the CO_2 mixing ratio measured at the ARM site and its difference from the WLEF site. On 8/15 the difference is as large as 38 ppm. This is strong evidence that there exists a north-south gradient of CO_2 in the real world. On 8/16, the model shows that the northerly wind cools down Oklahoma, so the daytime soil respiration is not so strong anymore and the photosynthesis resumes. It is consistent with the decreasing trend of the observations on 8/16 in the upper panel.

3.4.3.3 Horizontal divergence/convergence of CO_2

An idea similar to section 3.4.1.2 (vertical flux divergence) can apply for horizontal divergence. Let's consider only one level instead of a column and assume that the air is non-divergent.

Equation 3.2

$$\frac{\Delta \overline{C}}{\Delta t} = -\overline{\overline{u}_{2d}} \cdot \nabla_{2d} \overline{C} - \left[\overline{w} \frac{\partial \overline{C}}{\partial z} + \nabla_{3d} \cdot \left(\overline{u'_{3d} C'} \right) \right]$$

Equation 3.2 is another form of Equation 3.1, for a particular level instead of an air column, and the horizontal advection term is considered outside the brackets. If we neglect the second term (the bracket term) on the right hand side of Equation 3.2, we can derive the time rate of change of CO_2 due to horizontal advection.

Figure 3.27 shows the CO_2 concentration estimated based on Equation 3.2 with the neglect of the bracket term. The observations are also shown to compare with the estimates; the model does not have the level of 244 m, so the closest level to 244 m, 236.5 m, is used.
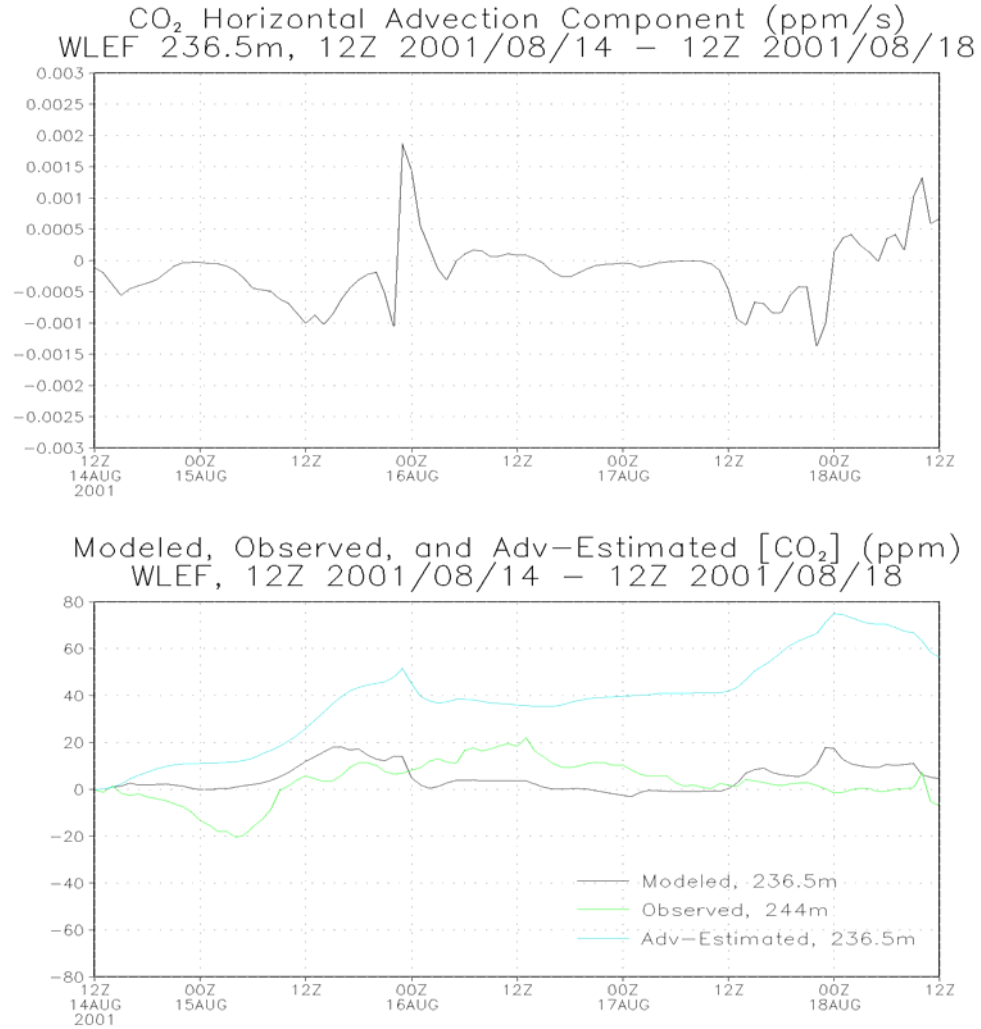
Figure 3.27: CO_2 horizontal advection at WLEF site and $[CO_2]$ time rate of change due to horizontal advection.

Unfortunately, we do not have CO_2 observations nearby at the same levels (396 m or 244 m) as at the WLEF site. Therefore, the model output is the only source that we have to calculate the influence of CO_2 horizontal advection.

The upper panel of Figure 3.27 shows that although the horizontal advection component (the first term on the RHS of Equation 3.2) of the transport equation is usually very close

to zero and has both positive and negative values throughout the period of interest, this component still increases CO_2 concentration at 244 m of WLEF site. The simulated CO_2 (the black line) from the model result does not always follow the estimated CO_2, considering only the influence of horizontal advection. When the modeled CO_2 has a very similar shape as the estimated one, apparently there is a CO_2 sink, consuming the contribution from horizontal advection. The mechanism is either vertical transport (e.g. 18Z 8/15, Figure 3.21) or ecosystem photosynthesis (e.g. 18Z 8/15 – 00Z 8/16, Figure 3.22a). Vertical transport might exist in a form of vertical advection or vertical flux.

3.4.3.4 Summary

The model result shows that horizontal advection is the most important factor that makes CO_2 rise in this case. On 8/14, 8/15, and most of 8/16, Texas and Oklahoma suffer from very high temperatures. These extremely high temperatures shut down photosynthesis in the model and pump out more CO_2 from the ground. This CO_2-rich air then is advected to the north by the wind field of a frontal system.

3.4.4 Section Summary

In Section 3.4.1, we can see that vertical flux divergence increases the CO_2 concentration as well as horizontal advection in Section 3.4.3. Section 3.4.1 is based on observations, while Section 3.4.3 is based on model output.

Horizontal advection might have an indirect influence on vertical flux divergence. For example, horizontal advection brings CO_2-rich air above the level of interest, and that CO_2-rich air is then transported downward by vertical flux to the level of interest. Therefore, the idea that both horizontal advection and vertical flux divergence increase CO_2 concentration at a specific level is not contradictory to each other. The biggest problem, however, is that we do not have a good match of $[CO_2]$ variation between the model output and the observations. So far, we can only prove that both the ecosystem response to the weather change and horizontal advection play important roles in this case.

Chapter IV   Conclusion and Future Work

4.1 Conclusion

The objectives of this study were:

1) to interpret the signal of CO_2 in a frontal event with regard to the ecosystem response to the weather change, vertical mixing, and horizontal advection;
2) to simulate CO_2 rising before a cold front arrived at the WLEF the tower in central Wisconsin on 2001/08/16 and decreasing with its passage; and,
3) to serve as a building block for the integration of an atmospheric model and a land surface model, which will facilitate future work in finding and understanding regional CO_2 sources and sinks.

In pursuit of the first objective, the study employed two major methods, including observation data analysis and a coupled atmosphere-biosphere model simulation. Data analysis of flux and CO_2 concentration observations showed that most of the CO_2 rising signal occurring just prior to a frontal passage in this case study came from the ecosystem response to the weather change, while the simulation confirmed the importance of horizontal advection. Objective 2 and 3 were not pursued separately, but in concert. The results presented in Chapter III directly address objective 2, and were made possible by

model developments and data preparation described in Chapter II, which address objective 3.

Our coupled model, SiB-RAMS, comprises a regional atmospheric model, RAMS, modified to accommodate the land surface model, SiB 2.5, in which Faquhar-Berry model together with Ball-Berry stomatal resistance equation calculates CO_2 flux and water vapor/latent heat flux from the ecosystem at the same time, according to the model weather. In the course of this study, the interface between RAMS and SiB has been built and tested. Tracer exchange, energy exchange, momentum friction, and land surface albedo were considered. Also, a new convection scheme (Grell scheme) has been built in and transports passive tracers. New and high-resolution NDVI, biome type, and soil type maps were used in this research. Offline SiB 2.5 was run for more than 10 years to get soil moisture and respiration factors for the online coupled model, SiB-RAMS. Anthropogenic CO_2 source and oceanic CO_2 flux were also included as inputs to the system.

SiB-RAMS was successful at reproducing many of the aspects of both biospheric and meteorological features, including daily cycles of NEEC, temperature, air pressure, wind direction, and radiation during the period of interest (00Z 2001/08/11 – 00Z 2001/08/21). However, the model did not simulate the very weak photosynthesis rate on 2001/08/15 due to full-sky cloud cover; this conclusion was not proved because of observation data missing. Simulated sensible heat flux and latent heat flux were carefully compared with observations, and were reasonably reproduced; simulated CO_2 concentration in the lower

levels of the coupled model also reflected the influence of net ecosystem exchange of carbon (NEEC). This indicated the successful coupling. Wind direction and wind speed matched observations well except for 2001/08/16 and 2001/08/17. The front in the model that was supposed to arrive at WLEF at 13Z 2001/08/16 moved about eight hours faster at the key time.

NEEC and vertical flux divergence of CO_2 based on tower observations during the period of interest showed that the ecosystem response to the weather change was responsible for part of the $[CO_2]$ rising (more than 40 ppm in 33 hours) from 04Z 2001/08/15 to 13Z 2001/08/16. About 1/3 of the rising might be attributed to NEEC. The rest of it should be due to horizontal advection. CO_2 was depleted by the restored photosynthesis rate after the front on the following day and further washed out by horizontal advection of a lower CO_2 concentration air mass from Canada. The horizontal convergence of CO_2 calculated from the model output showed that horizontal advection increased model CO_2 concentration from 8/14 to 8/18 and it was the most important mechanism for the rising.

Through careful examination of canopy air space temperature and canopy air space humidity in the model, I found that photosynthesis of the ecosystem in Texas and Oklahoma was shut down on 2001/08/14 and 2001/08/15 due to extremely high temperatures near the surface. The CO_2-rich zone was located north of this source, because the prevailing winds were southerly during this period. High concentration CO_2 air was thus transported to northern Wisconsin and stayed for a short period of time (12Z 8/15 – 00Z 8/16). As the convergence zone of a low-pressure system to the north of the

high concentration zone moved slowly to southeast, the enriched air followed accordingly. When the cool air invaded Oklahoma and Texas from the north, it suppressed the CO_2 outgoing pump from the ecosystem in those two states during the daytime, thereby signaling the end of the synoptic event of interest.

Both model output and observation showed that the vertical mixing could be achieved in one hour or two, which was much shorter than the time span of CO_2 rising in this case. Therefore, we ruled out the possibility of vertical mixing as the main reason for CO_2 rising by more than 40 ppm in 33 hours.

CO_2 concentration, different from traditional meteorological parameters, is strongly influenced both by the local land surface and transportation in the time scale of hours. Thus, the reproduction of CO_2 signals is vulnerable to the model failure of the ecosystem response, wind fields, and CO_2 spatial distribution. A slight difference of CO_2 spatial distribution and/or wind fields may cause the signals showing up in the wrong place and at the wrong time. For instance, if the convergence zone (18Z 8/15, Figure 3.21b) that determined the CO_2 transport in synoptic scale in this case was shifted to the south by 1-degree latitude, the WLEF tower might not be able to detect the high concentration signal from Texas and Oklahoma. In essence, the coherent variation of the CO_2 field and wind field strongly influences the results. On the other hand, the failure of reproduction of the local weather may cause the loss of local signal from the ecosystem. For instance, the model did not reproduce the cloudy sky during the daytime of 2001/08/15 successfully,

and thus made the simulated CO_2 at the WLEF site stop accumulating after 17Z 2001/08/15.

The model behaved differently from the observations, from the perspective of single point comparisons (the WLEF site) and surface pressure systems. In the model, horizontal advection played a very significant role, which could be seen from Figure 3.23. There might exist a "downscaling" problem (Castro 2005) in this model. SiB-RAMS, like any other regional models, suffers from losing the atmospheric variability after long forward time integration.

4.2 Future Work

The CO_2 concentration measured in the tower is usually a mix of local, regional, synoptic, and even climatological signals. If we cannot explain any of the CO_2 signals through our understanding of ecophysiology, transport, turbulence, or others, we unfortunately have to filter out the unresolved part and treat it as "noise" before we apply the data in inverse modeling. For example, TransCom 3 (Gurney 2002, see Chapter I) used weekly, large-area representative [CO_2] flask data to implement its continental-scale inverse modeling technology. TransCom 3 cannot use tower observations in GCMs, simply because, without appropriate filtering, the data contains too much "noise", while GCMs cannot "see" the biospheric or atmospheric processes smaller than synoptic scale. Thus, the first goal for further study is to reproduce the signals as accurately as possible, and to design the model to simulate all the ecophysiological and meteorological processes correctly.

This case study can be redone in a few different ways to simulate the details of the wind field right. For example, we can apply numerical weather prediction (NWP) mode on this case, in which we re-initialize the model every 12 hours. By doing so, the weather will not "drift away" too much from the input NCEP Eta reanalysis data. Another option is to do the spectral nudging in the model interior. If we only nudge the large-scale features, we can keep the small-scale features from being smoothed out and obtain reasonable large-scale meteorological fields. These two methods, however, give up some freedom of the predictive skills of the model. Thus, the best and the most laborious solution to this is to find out why, from the modeling perspective, the model did not get the wind field right on 2001/08/16 and 2001/08/17 and fixed the problem.

This case study used Andres' anthropogenic and Takahashi's oceanic CO_2 fluxes as inputs to the domain. Oceanic flux data was for the reference year 1995 and has not been updated since then, although oceanic flux does not change that much in the time scale of months. Anthropogenic CO_2 flux, on the contrary, could have changed a lot. It could also have a huge impact on our simulation. For example, while the weather changed during the frontal passage, people might change their behavior of using gas for their cars. If that emission overwhelmed the ecosystem response and the resultant CO_2 anomaly was later advected to somewhere else, the signal would have been detected by towers. Andres and his colleagues (1995) used fossil fuel consumption and cement manufacture record together with population density to estimate the anthropogenic CO_2 flux, which is used in this study. The biggest weakness of the estimation is that population density is not

necessary proportional to fossil fuel usage. For instance, the power plants that use coal to generate electricity may be located hundreds of miles away from the big cities. Also, while airplanes emit CO_2 in the upper levels to some significant amount, they actually fly over non-resident areas. This issue is now under investigation (Gurney 2005, personal communication). For future work, we recommend using more sophisticated anthropogenic and oceanic CO_2 flux data.

In this case study, soil moisture was also a variable that can be better defined. More realistic soil moisture might be obtained from an on-line SiB-RAMS spin-up. However, my attempt to spin up the coupled model for three more months (May 2001 – July 2001) to obtain internally consistent soil moisture for August 2001 had failed. Fixing the problem of excessive precipitation in the mountains and inner grids is the first step to acclimate the soil moisture to the weather.

The Harrington two-stream radiation scheme was used in this research. This scheme considers CO_2, H_2O, and O_3 for the absorption of both solar and infrared radiation. The spatial distribution of CO_2 and its temporal variation are, however, not considered when calculating gaseous absorption. This implies that we can modify the scheme to better represent the role of CO_2 in the radiation budget since we actually transport it in the model.

Another future work possibility to investigate the sources/sinks of CO_2 and its transport is an isotope collection campaign. If air sample can be collected in Texas and Oklahoma

when the ecosystem is pumping out CO_2, the C^{12}/C^{13} ratio of the dominant C4 plants in these two states can "record" this event; hopefully the signals can later on be advected to Wisconsin. A continuous isotope collection campaign both in Oklahoma and in Wisconsin during the frontal event will help to prove that our model results are correct or not.

Despite these areas of improvements, some encouraging results shed new light on the importance of transport and biospheric processes in determining the atmospheric distributions of CO_2, and lead to different interpretations of the sources and sinks from the land surface. The use of the coupled model in inverse modeling, after we determine how to define our lateral boundary conditions that transport constituent into/out of the regional domain, is expected. Not until we someday can reproduce the CO_2 signals to some accurate degree in the regional scale, we have the confidence to utilize the regional inverse modeling technique. The *a priori* flux estimates ($\vec{m}_p$) and the transport matrix ($\hat{G}$) that are generated by SiB-RAMS, and the observed CO_2 concentration ($\vec{d}_{obs}$) that is obtained from tower observations, can be used in Bayesian cost function (see Equation 1.4 of Section 1.2). The boundary condition of CO_2 has to be considered as a priori flux estimates too. Then by minimizing the cost function, we have the better-resolved *a posteriori* flux estimates in the regional scale.

This study has overcome our previous inability to model the regional-scale CO_2 signal. With sophisticated enough land surface and atmospheric models, we can identify the signals from the ecosystem or from horizontal advection more robustly. This case study

can also be used in the design of tower networks. The long-term goal is to utilize tower

data, with appropriate filtering or averaging methodology to retain signals and screen out

noise to investigate regional CO_2 sources/sinks with appropriate temporal and spatial

resolution.

Reference:

Andres, R. J., G. Marland, I. Fung, and E. Matthews, 1996: A 1 degrees x 1 degrees distribution of carbon dioxide emissions from fossil fuel consumption and cement manufacture, 1950-1990. *Global Biogeochemical Cycles*, **10,** 419-429.

Avissar, R. and Y. Liu, 1996: Three-dimensional Numerical Study of Shallow Convective Clouds and Precipitation Induced by Land Surface Forcing. *Journal of Geophysical Research*, **101,** 7499-7518.

Baldocchi, D. D., 2003: Assessing the Eddy Covariance Technique for Evaluating Carbon Dioxide Exchange Rates of Ecosystems: Past, Present, and Future. *Global Change Biology*, **9,** 479-492.

Bender, M. et al, 2002. *A large-scale CO2 observing plan: In situ oceans and atmosphere (LSCOP)*. NOAA OAR Special Report, 201 pp. Available online: http://www.ogp.noaa.gov/mpe/gcc/co2/observingplan/toc.htm

CarboEurope Integrated Project, 2003. *Assessment of the European Terrestrial Carbon Balance*. Sixth Framework Programme (Global Change and Ecosystems), Contract No. 505572, European Union, 276 pp.

Castro, C. L., R. A. Pielke, Sr., G. Leoncini, 2005: Dynamical Downscaling: Assessment of Value Retained and Added Using the Regional Atmsopheric Mdoeling System. *Journal of Geophysical Research - Atmosphere*, **110 (D5)**, Art. No. D05108.

Chan, D., C. W. Yuen, K. Higuchi, A. Shashkov, J. Liu, J. Chen, and D. Worthy, 2004: On the CO_2 Exchange between the Atmosphere and the Biosphere: the Role of Synoptic and Mesoscale Processes. *Tellus*, **56,** 194-212.

Chen, C. and W. R. Cotton, 1983: A One-Dimensional Simulation of the Stratocumulus-Capped Mixed Layer. *Boundary Layer Meteorology*, **25,** 289-321.

Clark, T. L., 1977: Small-Scale Dynamic Model Using a Terrain-Following Coordinate Transformation. *Journal of Computational Physics*, **24,** 186-215.

Clark, T. L. and R. D. Farley, 1984: Severe Downslope Windstorm Calculations in 2 and 3 Spatial Dimensions Using Aelastic Interactive Grid Nesting - A Possible Mechanism for Gustiness. *Journal of Atmospheric Sciences*, **41,** 329-350.

Clark, T. L. and W. D. Hall, 1991: Multi-Domain Simulations of the Time Dependent Navier-Stokes Equations: Benchmark Error Analysis of Some Nesting Procedures. *Journal of Computational Physics*, **92,** 456-481.

Collatz, G. J., M. Ribascarbo, and J. A. Berry, 1992: Coupled Photosynthesis-Stomatal Conductance Model for Leaves of C4 Plants. *Australian Journal of Plant Physiology*, **19,** 519-538.

Collatz, G. J., J. T. Ball, C. Grivet, and J. A. Berry, 1991: Physiological and Environmental Regulation of Stomatal Conductance, Photosynthesis, and Transpiration - A Model that Includes a Laminar Boundary Layer. *Agricultural and Forest Meteorology*, **54,** 107-136.

Cotton, W. R., R. A. P. Sr., R. L. Walko, G. E. Liston, C. J. Tremback, H. Jiang, R. L. Mcanelly, J. Y. Harrington, M. E. Nicholls, G. G. Carrio, and J. P. Mcfadden, 2002: RAMS 2001: Current status and future directions. *Meteorology and Atmospheric Physics*, **82,** 5-29.

Davis, K. J., P. S. Bakwin, C. Yi, B. W. Berger, C. Zhao, R. M. Teclaw, and J. G. Isebrands, 2003: The Anuual Cycles of CO_2 and H_2O Exchange Over a Northern Mixed Forest as Observed from a Very Tall Tower. *Global Change Biology*, **9,** 1278-1293.

Denning, A. S., M. Nicholls, L. Prihodko, I. Baker, P. L. Vidale, K. Davis, and P. Bakwin, 2003: Simulated Variations in Atmospheric CO_2 over a Wisconsin Forest Using a Coupled Ecosystem-Atmosphere Model. *Global Change Biology*, **9,** 1241-1250.

Eastman, J. L., M. Coughenour, and R. A. Pielke, Sr., 2001: The Regional Effects of CO_2 and Landscape Change Using a Coupled Plant and Meteorological Model. *Global Change Biology*, **7**, 797-815.

Geels, C., S. C. Doney, R. Dargaville, J. Brandt, and J. H. Christensen, 2004: Investigating the Sources of Synoptic Variability in Atmospheric CO_2 measurements over the Northern Hemisphere Continents: a Regional Model Study. *Tellus*, **56B**, 35-50.

Grell, G. A., J. Dudhia, and D. R. Stauffer, 1995: A Description of the Fifth-Generation Penn State/NCAR Mesoscale Model (MM5). *NCAR Technical Note*, 64-72.

Grell, G. A., 1993: Prognostic Evaluation of Assumptions Used by Cumulus Parameterizations. *Monthly Weather Review*, **121,** 764-787.

Grell, G. A., Y. H. Kuo, and R. J. Pasch, 1991: Semiprognostic Tests of Cumulus Parameterization Schemes in the Middle Latitudes. *Monthly Weather Review*, **119,** 5-31.

Gurney, K. R., R. M. Law, A. S. Denning, P. J. Rayner, B. C. Pak, D. Baker, P. Bousquet, L. Bruhwiler, Y. H. Chen, P. Ciais, I. Y. Fung, M. Heimann, J. John, T. Maki, S. Maksyutov, P. Peylin, M. Prather, and S. Taguchi, 2004: TransCom 3 Inversion Intercomparison: Model Mean Results for the Estimation of Seasonal Carbon Sources and Sinks. *Global Biogeochemical Cycles*, **18,** GB1010.

Gurney, K. R., R. M. Law, A. S. Denning, P. J. Rayner, D. Baker, P. Bousquet, L. Bruhwiler, Y. H. Chen, P. Ciais, S. M. Fan, I. Y. Fung, M. Gloor, M. Heimann, K. Higuchi, J. John, E. Kowalczyk, T. Maki, S. Maksyutov, P. Peylin, M. Prather, B. C. Pak, J. Sarmiento, S. Taguchi, T. Takahashi, and C. W. Yuen, 2003: TransCom 3 CO_2 Inversion Intercomparison: 1. Annual Mean Control Results and Sensitivity to Transport and Prior Flux Information. *Tellus*, **55,** 555-579.

Gurney, K. R., R. M. Law, A. S. Denning, P. J. Rayner, D. Baker, P. Bousquet, L. Bruhwiler, Y. H. Chen, P. Ciais, S. Fan, I. Y. Fung, M. Gloor, M. Heimann, K. Higuchi, J. John, T. Maki, S. Maksyutov, K. Masarie, P. Peylin, M. Prather, B. C. Pak, J. Randerson, J. Sarmiento, S. Taguchi, T. Takahashi, and C. W. Yuen, 2002: Towards Robust Regional Estimates of CO_2 Sources and Sinks Using Atmospheric Transport Models. *Nature*, **415,** 626-630.

Harrington, J. Y., 1997: *The Effects of Radiative and Microphysical Processes on Simulated Warm and Transition Season Arctic Stratus.* Ph.D. Dissertation, Colorado State University, Fort Collins, CO, 277 pp.

Haszpra, L., 1995: Carbon Dioxide Concentration Measurements at a Rural Site in Hungary. *Tellus*, **47,** 17-22.

Holtslag, A. A. M. and B. A. Boville, 1993: Local Versus Nonlocal Boundary-Layer Diffusion in a Global Climate Model. *Journal of Climate*, **6,** 1825-1842.

Hurwitz, M. D., M. R. Daniel, P. S. Bakwin, K. J. Davis, W. Wang, C. Yi, and M. P. Butler, 2004: Transport of Carbon Dioxide in the Presence of Storm Systems over a Northern Wisconsin Forest. *Journal of Atmospheric Sciences*, **61,** 607-618.

Klemp, J. B. and R. B. Wilhelmson, 1977: Simulation of 3-Dimensional Convective Storm Dynamics. *Bulletin of the American Meteorological Society*, **58,** 683.

Klemp, J. B. and D. K. Lilly, 1978: Numerical Simulations of Hydrostatic Mountain Waves. *Journal of Atmospheric Sciences*, **35,** 78-107.

Klemp, J. B. and D. R. Durran, 1983: An Upper Boundary Condition Permitting Internal Gravity Wave Radiation in Numerical Mesoscale Models. *Monthly Weather Review*, **111,** 430-444.

Liou, K. N., 1992: *Radiation and Cloud Processes in the Atmosphere*. Oxford University Press, New York, 487 pp.

Law, R. M., P. J. Rayner, L. P. Steele, and I. G. Enting, 2002: Using High Temporal Frequency Data for CO_2 Inversions. *Global Biogeochemical Cycles*, **16,** GB1053.

?, 2003: Data and modelling requirements for CO_2 inversions using high-frequency data. *Tellus B,* 5**5,** 512-521.

Louis, J. F., 1979: Parametric Model of Vertical Eddy Fluxes in the Atmosphere. *Boundary Layer Meteorology*, **17,** 187-202.

Louis, J.-F., 1979: A Parametric Model of Vertical Eddy Fluxes in the Atmosphere. *Boundary Layer Meteorology*, **17,** 187-202.

Lu, L., R. A. Pielke, Sr., G. E. Liston, W. J. Parton, D. Ojima, and M. Hartman, 2001: Implementation of a Two-Way Interactive Atmospheric and Ecological Model and Its Application to the Central United States. *Journal of Climate*, **14**, 900-919.

Mesinger, F. and A. Arakawa, 1976: Numerical Methods Used in Atmospheric Models. *GARP Publication Series, No. 14, WMO/ICSU Joint Organizing Committee*, 64 pp.

Mitchell, D. L., and W. P. Arnott, 1994: A Model Predicting the Evolution of Ice Particle Size Spectra and Radiative Properties of Cirrus Clouds. Part II: Dependence of Absorption and Extinction on Ice Crystal Morphology. *Journal of Atmospheric Science*, **51**, 817-832.

Nicholls, M. E., A. S. Denning, L. Prihodko, P. L. Vidale, I. Baker, K. Davis, and P. Bakwin, 2004: A Multiple-Scale Simulation of Variations in Atmospheric Carbon Dioxide Using a Coupled Biosphere-Atmospheric Model. *Journal of Geophysical Research - Atmospheres*, **109,** D18117.

Orlanski, I., 1976: A Simple Boundary Condition for Unbounded Hyperbolic Flows. *Journal of Computational Physics*, **21,** 251-269.

Pielke, R. A., 2001: Influence of the Spatial Distribution of Vegetation and Soils on the Prediction of Cumulus Convective Rainfall. *Reviews of Geophysics*, **39,** 151-177.

Pielke, R. A., W. R. Cotton, R. L. Walko, C. J. Tremback, W. A. Lyons, L. D. Grasso, M. E. Nicholls, M. D. Moran, D. A. Wesley, T. J. Lee, and J. H. Copeland, 1992: A Comprehensive Meteorological Modeling System - RAMS. *Meteorology and Atmospheric Physics*, **49,** 69-91.

Pielke Sr., R. A., 2002: *Mesoscale Meteorolgical Modeling*. Vol. 78, *International Geophysics Series*, Academic Press.

Potter, C. S., J. T. Randerson, C. B. Field, P. A. Matson, P. M. Vitousek, H. A. Mooney, and S. A. Klooster, 1993: Terrestrial Ecosystem Production - A Process Model Based on Global Satellite and Surface Data. G*lobal Biogeochemical Cycles,* 7**,** 811-841.

Ritter, B., and J.-F. Geleyn, 1992: *A Comprehensive Radiation Scheme for Numerical Weather Prediction Models with Potential Applications in Climate Simulations.* Monthly Weather Review, **120**, 303-325.

Schimel, D. S., 1995: Terrestrial Ecosystems and the Carbon-Cycle. G*lobal Change Biology,* 1**,** 77-91.

Schmid, H. P., 2002: Footprint Modeling for Vegetation Atmosphere Exchange Studies: A Review and Perspective. A*gricultural and Forest Meteorology,* 1**13,** 159-183.

Sellers, P. J., D. A. Randall, G. J. Collatz, J. A. Berry, C. B. Field, D. A. Dazlich, C. Zhang, G. D. Collelo, and L. Bounoua, 1996: A Revised Land Surface Parameterization (SiB2) for Atmospheric GCMs. Part I: Model Formulation. *Journal of Climate,* 9**,** 676-705.

Sellers, P. J., S. O. Los, C. J. Tucker, C. O. Justice, D. A. Dazlich, G. J. Collatz, and D. A. Randall, 1996: A Revised Land Surface Parameterization (SiB2) for Atmospheric GCMs. Part II: The Generation of Global Fields of Terrestrial Biophysical Parameters from Satellite Data. *Journal of Climate*, **9,** 706-737.

Sheridan, P. J., D. J. Delene, and J. A. Ogren, 2001: Four Years of Continuous Surface Aerosol Measurements from the Department of Energy's Atmospheric Radiation Measurement Program Southern Great Plains Cloud and Radiation Testbed Site. *Journal of Geophysical Research - Atmosphere*, **106,** 20735-20747.

Slingo, A., and H. M. Schrecker, 1982: On the shortwave properties of stratiform water clouds. *Quarterly Journal Review Meteorology Society*, **108**, 407-426.

Takahashi, T., S. C. Sutherland, C. Sweeney, A. Poisson, N. Metzl, B. Tilbrook, N. Bates, R. Wanninkhof, R. A. Feely, C. Sabine, J. Olafsson, and Y. Nojiri, 2002: Global Sea-Air CO_2 Flux Based on Climatological Surface Ocean pCO_2, and Seasonal Biological and Temperature Effects. D*eep-Sea Research Part II,* 4**9,** 1601-1622.

Tans, P. P., I. Y. Fung, and T. Takahashi, 1990: Observational Constraints on the Global Atmospheric CO_2 Budget. S*cience,* 2**47,** 1431-1438.

Tremback, C. J., 1990: Numerical Simulations of a Mesoscale Convective Complex: Model Development and Numerical Results. *Ph.D. Dissertation, Atmospheric Science Paper No. 465, Colorado State University, Dept. of Atmospheric Science, Fort Collins, CO 80523*.

Yamamoto, G., 1962: Direct Absorption of Solar Radiation by Atmospheric Water Vapor Carbon Dioxide and Molecular Oxygen. *Journal of Atmospheric Sciences*, **19,** 182-188.

Wofsy, S.C. and R.C. Harriss (2002*) The North American Carbon Program (NACP)*, Report of the NACP Committee of the U.S. Carbon Cycle Science Program. Washington, DC: US Global Change Research Program. Available on-line http://www.carboncyclescience.gov/nacp/